이학박사학위논문

Electrical transport studies of low-dimensional organic conductors and chalcogenide superconductors under high pressures

고압 하에서의 저 차원 구조를 가진 유기 전도체와 칼코겐 초전도체의 전기 전도도에 관한 연구

2018 년 2 월

서울대학교 대학원

물리천문학부

장 동 현

Electrical transport studies of low-dimensional organic conductors and chalcogenide superconductors under high pressures

고압 하에서의 저 차원 구조를 가진 유기 전도체와 칼코겐 초전도체의 전기 전도도에 관한 연구

지도 교수 김 기 훈

이 논문을 이학박사 학위논문으로 제출함
2018 년 2 월

서울대학교 대학원
물리천문학부
장 동 현

장동현의 이학박사 학위논문을 인준함

위 원 장 국 양 (인)
부위원장 김 기 훈 (인)
위 원 노 태 원 (인)
위 원 유 재 준 (인)
위 원 심 지 훈 (인)

Abstract

Many novel phenomena such as superconductivity, metal-insulator transition, and Fermi-surface reconstruction under high-pressure have been reported. High-pressure generally reduces lattice constant in turn modifies band structure. Due to these general effects, many interesting physical phenomena are expected. Recently, the discovery of 200 K superconductor under 155 GPa shows the possibility of the room-temperature superconductor under high-pressure. On top of that, adjusting U/W ratio in the Mott insulators shows many exotic material properties such as an unconventional universality classes or superconductivity.

We measured electrical transports of various materials under high-pressure. High-pressure was achieved by three different kinds of pressure cells; hybrid piston cylinder cell, diamond anvil cell, and cubic anvil cell. These pressure cells have different pressure range and pressure quality. Hybrid piston cylinder cell can reach up to 3.0 GPa and diamond anvil cell can reach up to higher than 60 GPa. Although both cells use liquid medium, unexpected uniaxial pressure can be applied higher than medium solidification pressure. On the other hands, cubic anvil cell can apply highly hydrostatic pressure up to 10.0 GPa after liquid medium turns into solid.

In this thesis, we focused on low-dimensional materials such as 2*H*-Pd_xTaSe_2, La-doped $CaFeAs_2$, and P-doped $BaFe_2As_2$ with the quasi two-dimensional crystal structures and $Nb_2Pd_1Se_5$, and $[(S,S)\text{-DM-MeDH-TTP}]_2AsF_6$ with the quasi one-dimensional crystal structures.

In two dimensional materials, superconductivity was enhanced in measured superconductor samples and insulating behavior such as charge density

wave, spin density wave, and insulating gap were suppressed by pressure. In addition, some superconductors show quantum critical behaviors under high-pressure.

In 2*H*-Pd_xTaSe_2, incommensurate and commensurate charge density wave were suppressed and superconductivity was enhanced under pressure. We also show that the superconductivity and charge density wave are competing in these materials. This enhancement of superconductivity was also observed in $CaFeAs_2$, $BaFeAs_2$, and $Nb_2Pd_xSe_5$ single crystals.

In the [(*S,S*)-DM-MeDH-TTP]$_2AsF_6$ one-dimensional organic conductor, we observed critical exponents δ, β, and γ of an electrical conductivity which are considered as an order parameter of metal-insulator transition. The quantum criticality in two-dimensional metal-insulator transition was suggested in theoretical calculation in 2011 and discovered experimentally in 2015. We have found the quantum criticality in [(*S,S*)-DM-MeDH-TTP]$_2AsF_6$ with the critical exponent $z\nu = 1$. This obtained value of $z\nu = 1$ is the same as theoretical calculation for Tomonaga-Luttinger liquid model. This implies that the universality class is determined only by global factor such as dimensionality or symmetry, not microscopic factor such as a microscopic interaction.

Keyword : Low-dimensional system, superconductors, organic conductors, high-pressure, the quantum criticality, critical exponent, universality class

Student Number : 2011-30123

Contents

List of figures

1. Introduction

In deep in Earth, all elements experience pressure due to gravity. This pressure melts rocks and changes properties of elements. This activity makes four different layers; crust, mantle, outer core, and inner core with different physical properties. The pressure and temperature of the center of Earth is near 364 GPa and 5000 ºC. The high-pressure changes properties of materials. For example, black color and non-transparent carbon elements turn into shinny and transparent diamonds under high-pressure and high-temperature. Moreover, physical strength of carbon and diamond is very different. Carbon is very soft and it is used as pencils but diamond is very strong and it is used as cutting tools. This dramatic change of properties in the same elements makes physicists consider pressure as a new energy scale parameters.

In physics, many experiments have been conducted in the low temperature and high magnetic field to research their ground states and classical (or quantum) phase transitions of each ground state. These attempts were very successful to achieve new physical phenomena such as superconductivity, a metal-insulator transition, or a quantum criticality. Many theoretical calculations successfully explain the role of temperature and magnetic field as an energy scale.

High-pressure is also another energy scale, which can modify properties of materials such as appearance or enhancement of superconductivity, band structure modification, and suppression of lattice constants. In this thesis, we focused on transport properties of quasi low-dimensional systems under high-pressure and expect novel ground states.

Moreover, we introduce pressure tools such as hybrid piston-cylinder cell,

diamond anvil cell, and cubic anvil cell. These pressure tools have different pressure range and pressure quality. In the pressure measurements, pressure quality should be considered seriously because pressure usually induces unexpected uniaxial pressure and it makes poor reproducibility of measurements. To get rid of this concern, pressure quality such as a hydrostatic pressure is highly recommended.

High-pressure techniques indicated above change physical properties of materials by squeezing lattices. This induces the change of materials properties of quasi low-dimensional materials. We measured electrical transports of three kinds of quasi two-dimensional system and two kinds of quasi one-dimensional materials.

2. Overview

Many theories describing non-interacting electrons have successfully been predicting basic physical phenomena. However, exotic and rich properties of materials cannot be understood only by the theory describing non-interacting electrons. Thus, the correlation between electrons has been considered as important factor to describe richer and more exotic material properties. However, many exotic physical properties have not been exactly understood due to lack of theory. Thus, we will briefly review the theoretical background to understand the interpretation of our results.

2.1 Landau Fermi liquid theory

Drude explained the resistivity by considering only the scattering of electrons in a uniform electric field [1]. Drude described electrons in metals with scattering like point particles without any interactions [2]. In his description, the resistivity is expressed by $\rho = m/ne^2\tau$, where m is the electron mass, n is the density of states, e is the electron charge and τ is the collision time. This theory is in good agreement with resistivity of many metals. Furthermore, many different scattering mechanisms that affects to the resistivity was considered. Main assumption of this theory is that scatterings are independent of each other, and can be summed up according to Matthiesen's rule: $1/\tau = 1/\tau_0 + 1/\tau_e + 1/\tau_{ph} + 1/\tau_{LM}$, where τ_0 is the temperature-independent scattering of impurities, τ_e, τ_{ph}, and τ_{LM} are temperature scatterings of electrons, lattice (or phonon), and local moments, respectively. Then, the resistivity can be described as: $\rho = \rho_0 + \rho_e + \rho_{ph} + \rho_{LM}$. According to this theory, the resistivity decreases under magnetic field, since

disorder can be suppressed by magnetic field.

In Fermi-liquid state, the resistivity shows a quadratic dependence with temperature, $\rho(T) = \rho_0 + AT^2$. In high temperature, electron-phonon scattering is a dominant scattering, while electron-electron scattering is dominant at low temperature. An electron with energy $E_1(K_1)$ above the Fermi surface that resides within k_BT about the Fermi surface scatters off of an electrons below the Fermi surface which has an energy $|E_2(K_2)| < E_1(K_1)$. The scattered electron has a smaller energy than that of the first electron for the final states to be above the Fermi surface and contribute to the conduction. In the final state, the electrons have energies $E_3(K_3)$ and $E_4(K_4)$ [2]. A single scattering event is indicated in figure 2.1.1.

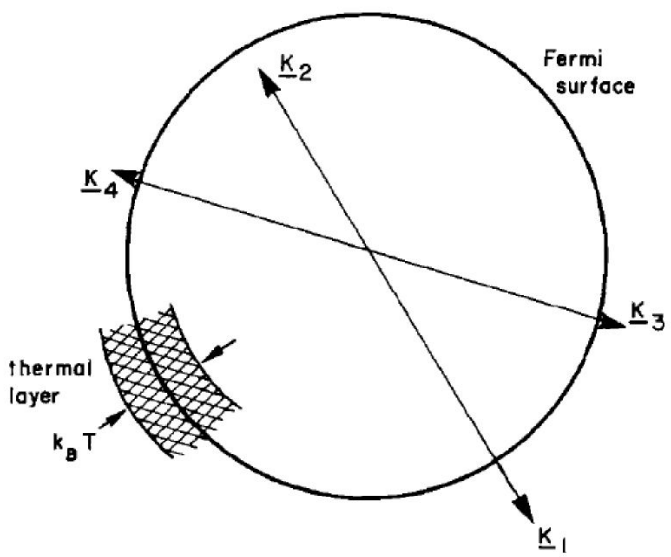

Figure 2.1.1. Diagram showing the initial (K_1 and K_2) and final states (K_3 and K_4) of a single electron-electron collision [2].

The scattering rate can be described as $1/\tau(K_1)=\sum P(K_1, K_2, K_3, K_4)$. Conservation of energy and momentum and the Pauli exclusion principle places restrictions to the final state so that $1/\tau(K_1) \propto \sum P(E(K_2), E(K_3), q)$, where $q = K_2 -$

K_3. In other words, the scattering rate depends on the number of electronic state with energy $E(K_2)$ available for scattering and the number of empty states with energy $E(K_3)$ available for scattering into. Since both are proportional to $k_B T_N(E_F)/E_F$, where $N(E_F)$ is the density of states at the Fermi surface, then finally $1/\tau \propto T^2$ and also, $1/\tau \propto m^2$, where $N(E_F) \propto m$ [3].

In the Fermi liquid theory with non-interacting electrons, three assumptions are established [4].

- ➔ One to one correspondence between the low-lying excitations of electrons in the Fermi-gas and the quasi particles in the Fermi-liquid: The spin and momentum quantum numbers of electrons are good quantum number for quasi particles.
- ➔ The interactions between electrons are turned on adiabatically, so as to prevent any phase transitions and ensure that the new density of states is a smooth change from that of a free electron gas.
- ➔ Electron charges of the quasi particles are $-e$.

2.2 Density wave

The density wave characters such as charge density wave or spin density wave are spatial fluctuations of charge and spin, respectively and it breaks translational symmetry. Cr metal is a good example of a spin density wave [5]. 3d electrons of Cr are not fully occupied so it becomes itinerant conduction electron. This implies that transition metal with unoccupied 3d electrons such as Fe, Co, and Ni has no local magnetic moments, although they show ferromagnetism. It was explained by the Stoner model, which describes a mechanism for itinerant

ferromagnetic ordering.

Overhauser explained spin density wave of Cr and it was related to the itinerant antiferromagnetic ordering due to its Fermi surface nesting between electron and hole [5].

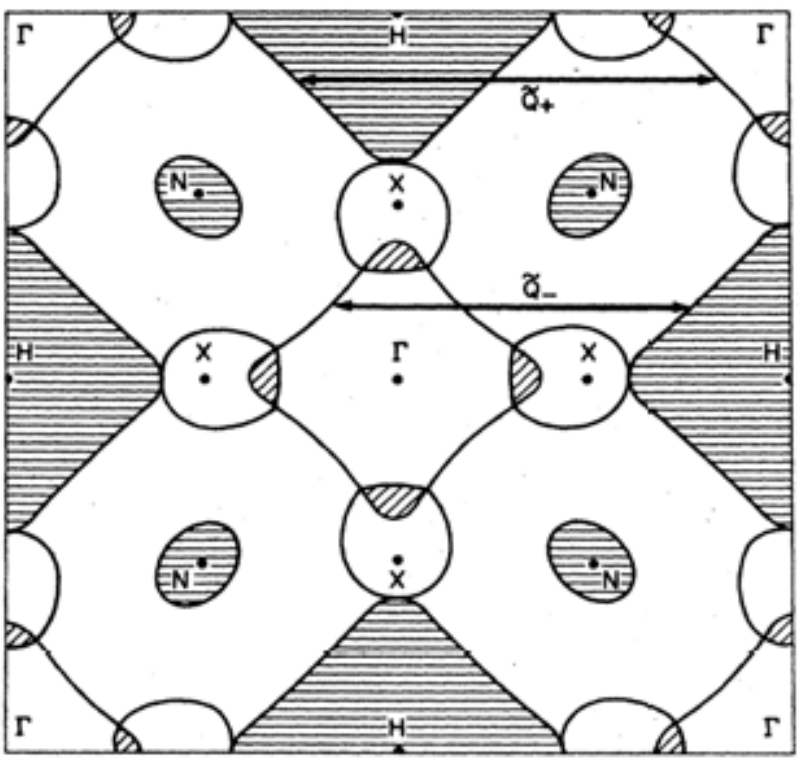

Figure 2.2.1. Fermi surface of Cr along the (100) plane. The wavevectors Q_- and Q_+ indicate the nested electron and hole Fermi surfaces [Fawcett, 1988; Laurent et al., 1981].

Figure 2.2.1 shows the Fermi surface of the (100) plane and the nesting vector Q_- and Q_+. Consider that in a crystalline metal, the atomic ions are screened by the electrons. The Lindhard response function describes how this screening mechanism causes electrons to redistribute in response to an external perturbation [6].

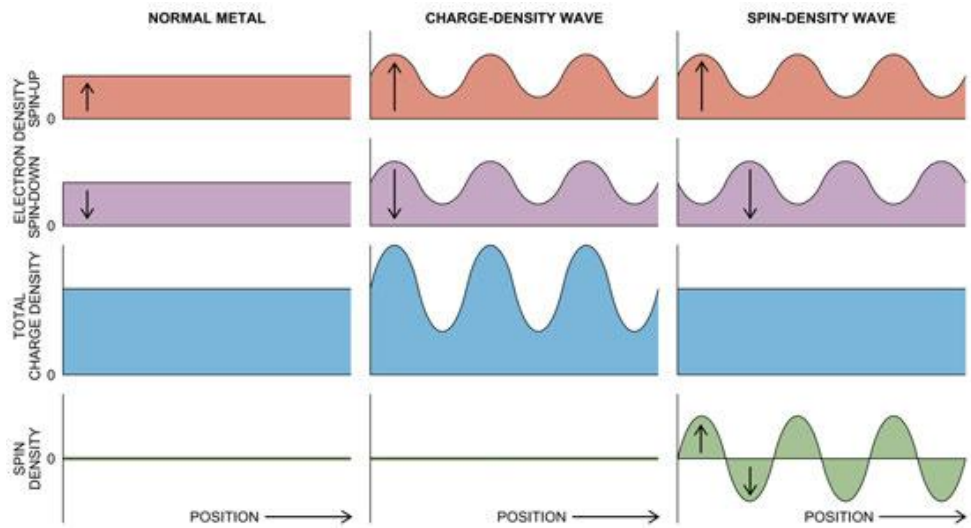

Figure 2.2.2 Comparison of a normal metal, charge density wave (CDW), and spin density wave (SDW) considering the spin up and down electron density, the total charge density and the spin density as it is visualized in real space [Brown and Gruner, 1994].

In figure 2.2.2, the difference between a normal metal, charge density wave (CDW), and spin density wave (SDW) in real space are indicated. For CDWs, the density of electrons is spatially modulated and causes periodic distribution of the lattice. This distribution forms the periodicity of the CDW and opens up a gap in the electron band. The opening up of the gap decrease of the system's energy. However, the distortion of the lattice causes an increase in the system's elastic energy. Even though, system's energy is increased by elastic energy, whole system is stabilization by opening up CDW gap.

In real system, CDW and SDW are often seen in lower dimensional systems such as two-dimensional or one-dimensional systems because Fermi surface nesting is more favorable in low-dimensional systems indicated in figure 2.2.3.

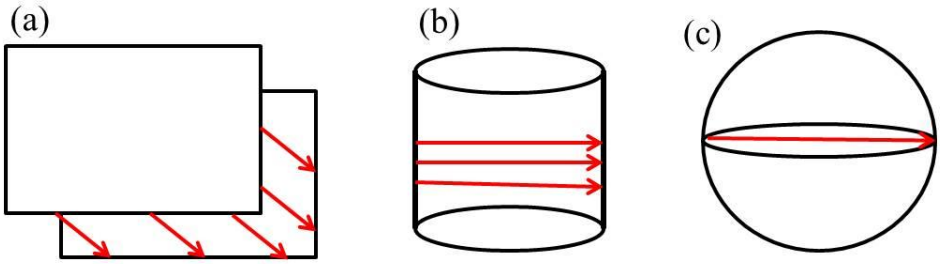

Figure 2.2.3 Schematics of Fermi surface topology in one-dimension (a), two-dimension (b), and three-dimension (c). The red arrows are wave vectors of $2k_F$ going one Fermi surface to another and indicate an occupied and unoccupied state.

When the CDW or SDW gap opens, systems become more insulating because density of states are empty in the Fermi surface. In low-dimensional system, CDW can cause this metal-insulator transition, which is called a Peierls transition due to the Peierls instability.

2.3 Metal-insulator transition

Electrical conductivity, which varies from 10^{-22} $\Omega^{-1}cm^{-1}$ for an insulator to 10^{10} $\Omega^{-1}cm^{-1}$ for pure metal (except superconductor) becomes intriguing due to its theoretical and experimental results. In pure metals, electronic states responsible for charge transport are spatially extended in materials, while it is localized in an insulator. It is generally agreed that the localization of electrons can be caused by disorder proposed by P. Anderson [7], strong electron-lattice coupling proposed by T. V. Ramakrishnan [8], or strong electron-electron correlations proposed by Hubbard [9]. In many case, many mechanisms contribute to properties of materials.

Phenomenologically, the metal is considered state with a finite DC electron conductivity at zero temperature, whereas the insulator has zero electron

conductivity at zero temperature. In the microscopic point of view, this is due to the fact that the metal has the Fermi surface with gapless excitations at zero temperature, whereas the insulator is gapped at Fermi surface. Several criteria have been proposed by many researchers. We will discuss these criteria for the metal-insulator transition (MIT).

2.3.1 Mott criteria

Mott criteria explain the electron localization when materials approach from metal to insulator [10]. The metal is made of a lattice of positively charged ions plus free conduction electrons.

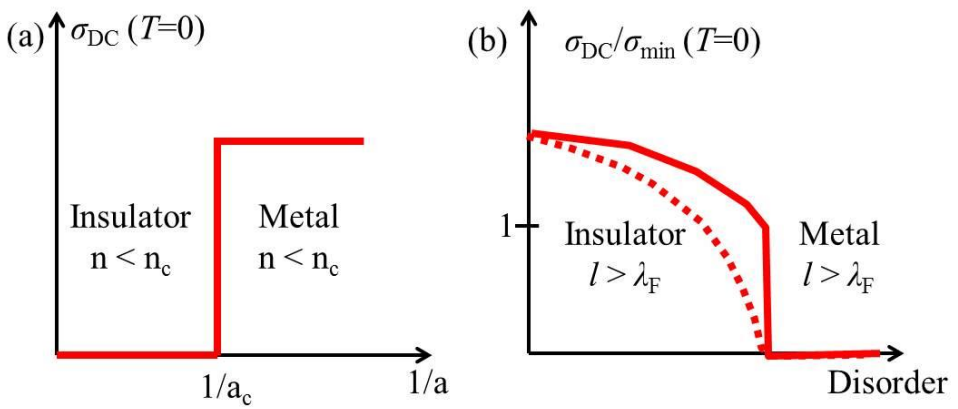

Figure 2.3.1. (a) Mott's first criterion. The dilute system (left part) is the insulator and the dense electron system is the metal (right part). a is the interdonor spacing and the electron density is proportional to $1/a$. (b) the mean free path of electrons (l) is larger than their de Broglie wavelength (λ_F). The Mott transition occurs at $T = 0$, when σ is smaller than σ_{min}. The red line is first-order MIT at $T = 0$, while continuous MIT is indicated by the red dotted line.

In high density of state of conduction electrons, the itinerant electrons

screen the attractive Coulomb potential between electrons and ions. As a result, conduction electrons do not make bound states with ions, and the system becomes metallic. If the density of conduction electrons is gradually decreased by increasing the inter-particle distance, the screening becomes smaller. Finally, at some critical density (n_c) the electron-ion bound states form and the system becomes an insulator with $\sigma_{DC} = 0$ at $T = 0$ indicated in figure 2.3.1 (a). In addition, Mott suggested that the critical inter-donor distance (a_c) makes first-order MIT. In figure 2.3.1 (b), first-order and second-order MIT were indicated.

Mott's first criterion is generally stated in terms of the n_c and the Bohr radius of the donor nucleus a^*: $n_c^{1/3}a^* \leq 0.25$. In this criterion, temperature must be zero because only few millikelvin temperatures can contribute electrical conductivity.

Mott's second criterion argues that there is minimum conductivity σ_{min} which determines the metallic behavior in the material [11]. According to his paper, his idea is based on the breakdown of the Boltzmann theory of electronic transport. When the mean free path of electrons becomes less than the lattice spacing, the material shows insulating behavior. In the Drude model, the electrical conductivity at $T = 0$ is expressed by

$$\sigma(T=0) = \frac{ne^2\tau}{m} \approx \left(\frac{e^2}{h}\right)\frac{2^{2-d}}{2\pi}\frac{l}{a} = \sigma_0\frac{l}{a}$$

The approximations we used are $l = v_F\tau$ and $k_F = (d\pi n)^{1/d}$. The electron density is given by $n = a^{-d}$ where a is the lattice spacing. The minimum value of l is the lattice spacing a and results $\sigma_0 = \sigma_{min}$. When the mean free path of conduction electrons in the lattice is the order of their de Broglie wave length $\lambda_F = 2\pi/k_F$, we can calculate the minimum conductivity, which is called Ioffe-Regel limit [12].

Iofffe-Regel limit for the 3D materials, which have v conduction electrons per unit cell can be calculated considering the density of electrons $n = v/a^3$, where a is the cubic unit cell dimension. Using the Drude model in 3D with the limitation of $l \sim a$, we have

$$\sigma = \frac{ne^2\tau}{m^*} = \frac{ne^2 l}{\hbar k_F} = \frac{ne^2}{\hbar}\frac{l}{(3\pi^2 n)^{1/3}} \quad \overrightarrow{l \sim a} \quad \sigma_{IR} = \frac{e^2}{h}\frac{2\pi v}{(3\pi^2 n)^{1/3}}\frac{1}{a}$$

In the last term, we introduce the quantum conductance $e^2/h = 3.9 \times 10^{-5}$ $\Omega^{-1}m^{-1}$. In addition, IR maximum resistivity can be calculated by $\rho_{IR} = \sigma_{IR}^{-1}$.

Because the mean free path of the electrons is controlled by disorder, extended theory considering localization of electrons is introduced by Anderson [7]. The strong disorder makes the mean free path of the electrons comparable to the inter-atomic distance ($l \sim a$) and it results in $\sigma = \sigma_{min}$.

2.4 Quantum phase transition

The quantum phase transition (QPT) is continuous phase transitions which are observed at absolute zero temperature in the absence of thermal fluctuation [13]. Since thermal energy is not considered in QPT, other tuning parameters such as the magnetic field, disorder, doping, or pressure change its ground states at $T = 0$ K. When we consider a system defined by the Hamiltonian $H(g)$, the evolution of the ground state of $H(g)$ by adjusting g shows non-analytic behavior at the critical value $g = g_c$, where g is dimensionless coupling, representing non-thermal tuning parameters. This point ($T = 0$, $g = g_c$) is called the quantum critical point (QCP). The QPT is different from classical phase transition (CPT), since there is no thermal energy contribution when phase is evolving.

When the system crosses phase boundary of a CPT, the correlation length

and the correlation time (τ) diverge. This means that the order parameter of the system fluctuates coherently over increasing distance and more slowly. When we consider a frequency $\omega \propto 1/\tau$, the frequency becomes zero at the critical point. Thus, $\hbar\omega << k_B T_c$ is satisfied close to the classical critical point (CCP). This means that the critical fluctuation which drives the system to cross the phase boundary are soft mode ($\omega << 1$) in a finite temperature regime where all the quantum mechanical properties are smeared out and they can be treated by classical statistical mechanics. However, this is no longer valid in the QPT at $T = 0$. Because no thermal energy exists at $T = 0$, QPT is driven by purely quantum critical fluctuation whose origin lie in Heisenberg's uncertainty principle [14].

Two kinds of QCP were generally proposed. The first one has no ordered state at finite temperature indicated in figure 2.4.1 (a). This system can have the QCP at $T = 0$ and $g = g_c$, while the quantum ordered phase disappear above the absolute zero. The second case we can observe dotted line of CCP at finite temperatures, which determines QCP at $T = 0$ and $g = g_c$. In the shaded area around the CPT dotted line, the classical statistical mechanics governs the critical behavior within the shaded area (figure 2.4.1 (b)).

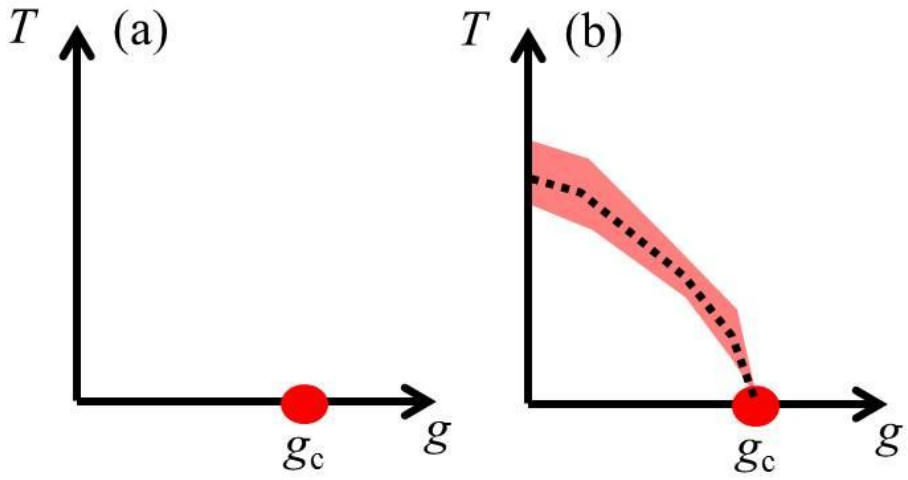

Figure 2.4.1. Two possible QCP. (a) no ordered state at finite temperature. (b) Dotted line indicates that classical ordered state and $\hbar\omega << k_B T_c$ only valid in the shaded area.

2.4.1. Classical critical behavior

The classical critical point (CCP) is the separation point between the ordered phase and the disordered phase at the finite temperature. The disordered phase can be characterized by the lager fluctuations of the order parameter. However, the ordered phase can be characterized by two parameters; first, the existence of the order parameter, and secondly, the divergence of correlation length of ξ and the correlation time τ at the transition. Close to the critical point, the only relevant length and time scales of the system are ξ and τ follow relations: $\xi \propto |T - T_c|^{-\nu}$, and $\tau \propto \xi^z \rightarrow \tau \propto |T - T_c|^{-z\nu}$, where ν is the critical exponent of correlation length and z is the dynamic critical exponent. Both ξ and τ diverge at the critical point ($T = T_c$). At the critical point, the physics of the system is completely determined by the long range fluctuations of the order parameter. Critical exponents show the universal behavior, which means that critical

exponents are independent of the microscopic details of the Hamiltonian, while global parameter such as dimensionality or symmetry determines their universality classes. This implies that the same universality class has the same set of critical exponents [15].

$\omega \propto 1/\tau$ indicates that the energy of the critical fluctuations vanishes with the power law: $\hbar\omega \propto \xi^{z} \propto |T - T_c|^{z\nu}$. For any finite temperature phase transition, we can always find a neighborhood of the critical point where the energy of the critical fluctuations ($\hbar\omega$) is less than the thermal energy at the critical temperature ($k_B T_c$). This corresponds to shaded area of figure 2.4.1 (b).

2.4.2. Quantum critical behavior

The quantum critical point is the point of a non-analyticity in the ground state of the system defined by $H(g)$. Generally, this happens when $H(g) = H_0 + gH_1$, where H_0 and H_1 commute and H_1 is a conserved quantity. At the $g = g_c$, a level crossing occurs such that at g_c an excited state becomes the ground state and g_c is a point of non-analyticity of the ground state energy. This singularity is related to the level-crossing or the avoided level-crossing indicated in figure 2.4.2.

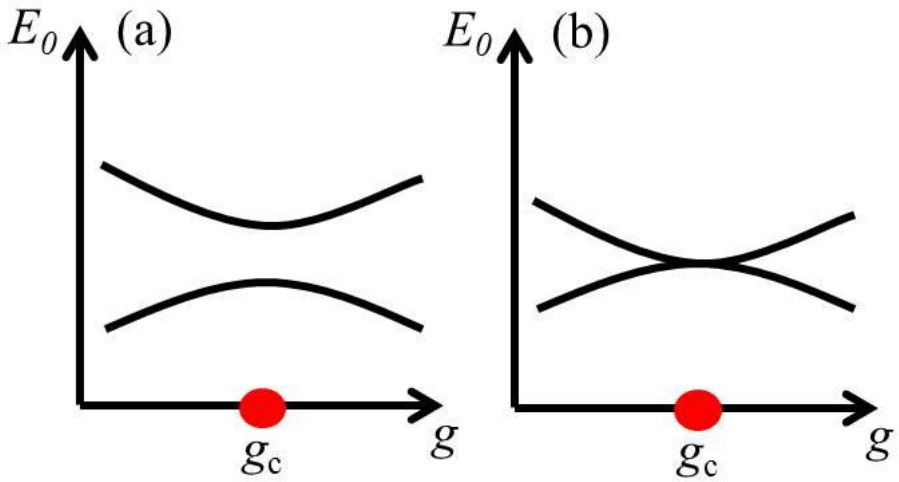

Figure 2.4.2 (a) The ground state energy E_0 of $H(g)$ is depicted as a function of tuning parameter g and two possible level-crossing. (a) Avoided level-crossing. (b) Actual level-crossing.

The quantum critical fluctuation energy Δ represents the difference between the ground state energy and the first excited energy, when energy spectrum of the system has an energy gap. In a gapless spectrum, Δ is defined by the energy scale at which there is a qualitative change in the nature of the frequency spectrum [13]. It is obvious that Δ vanishes at QCP: $\Delta \propto |g - g_c|^{z\nu}$. Δ is associated with a correlation time $\tau \propto 1/\Delta$ which diverges at the boundary of QPT $\tau \propto |g - g_c|^{-z\nu}$ and finally there is always a diverging correlation length which is related to the correlation time through the dynamical exponent similar to the classical case: $\tau \propto \xi^z \rightarrow \xi \propto |g - g_c|^{-\nu}$. Quantum critical systems with the same dimensionality and the same symmetries of the order parameter have identical critical exponents in the scaling limit (large ξ and τ).

When we consider the quantum problem, the extra imaginary dimension z

is introduced. This extra dimension is equally weighted as the spatial dimension. Thus, d dimension quantum problem maps into the $d + 1$ dimensional classical problem.

In figure 2.4.3, generic phase diagrams of the quantum critical system are depicted. The QCP separates the ordered ground state from the disordered one. In figure 2.4.3 (a), there is no ordered state at finite temperature. Three different regions are separated by crossover line. For $g < g_c$, the system can ordered only at $T = 0$, while disordered state was observed at finite temperature. In this case, only thermal fluctuation is responsible for the disorder. For $g > g_c$, the system shows disordered state at all temperature range due to the quantum fluctuation. The third region is the quantum critical region. It appears near the QCP and phase separation line is symmetric due to the thermal and the quantum fluctuations are comparable. The crossover line are obtained by $T \propto \Delta \propto |g - g_c|^{z\nu}$. In this regime, many systems show strange behaviors such as an unconventional power laws or a non-Fermi liquid behavior [16]. In figure 2.4.3 (b), finite temperature CPT is observed and it is terminated at a QCP at $T = 0$. In the red shaded area around dotted line, $\omega << T$ was kept and obeys classical statistical mechanics [16]. The physics in the quantum critical region is controlled by the thermal fluctuation of the quantum critical ground state whose effects can be probed experimentally by tuning g at sufficiently low temperatures and looking for the strange behaviors mentioned above [16].

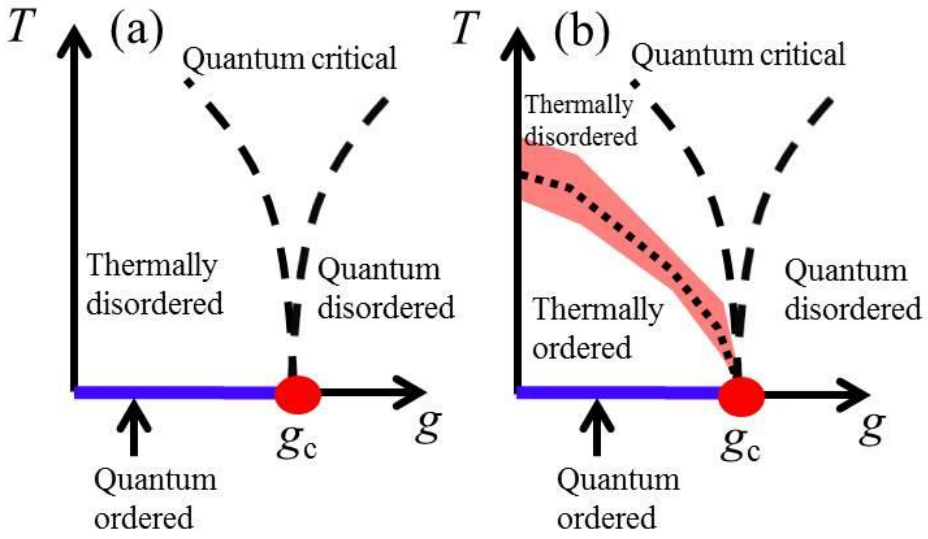

Figure 2.4.3. Generic phase diagram of the quantum critical system.

Bibliography

[1] Drude, Paul. Annalen der Physik. **306** 566 (1900)

[2] M Kaveh and N Wiser. Journal of Physics F: Metal Physics **12** 5 (1984)

[3] Stella Kim. Ph.D. thesis (2013)

[4] W. Harrison. Solid State Theory (1970)

[5] Overhauser, A. W. Phys. Rev. **128** 1437 (1962).

[6] G, Gruner. Density waves in solids, (2000)

[7] P. Anderson, Phys. Rev. **109** 1492 (1958).

[8] T. V. Ramakrishnan, Solid. St. Chem. **111** 4 (1994)

[9] J. Hubbard, Proc. Roy. Soc. London. Ser. A. **281** 401 (1963)

[10] N. F. Mott, Can. J. Phys. **34** 1356 (1956)

[11] N.F. Mott, Philos. Mag. **26** 1015 (1972)

[12] A.F. Ioffe, A. R. Regel. Prog. Semicond. **4** 237 (1960)

[13] S. Sachdev, quantum phase transitions, Cambridge University press (1999)

[14] S. L. Sondhi *et al*. Rev. Mod. Phys. **69** 315 (1997)

[15] N. Goldenfeld, Lectures on phase transition and renormalization group, Addison-Wesley (1992)

[16] Fazel Fallah Tafti. Ph.D. Thesis (2011)

3. Pressure apparatus

High-pressure techniques are quite difficult to achieve because samples are pressed by anvils, and thus have possibility to break of the samples. Small amount of inhomogeneous of applying pressure can make deformation of samples and induces unexpected change of material property. In the pressure experiments, sample mounting and pressurizing technique are the most critical part in order to obtain reliable data. Pressure techniques have been developing since high-pressure techniques emerge. In following sections, various pressure techniques such as hybrid piston cylinder cell, diamond anvil cell, and cubic anvil cell will be reviewed.

3.1 Hybrid piston cylinder cell

Hybrid piston cylinder cell composed of two parts; Ni-Cr-Al inner cell and BeCu outer cell. Inner Ni-Cr-Al material has good mechanical strength but easy to break, while outer BeCu is softer and hard to break. This combination makes the pressure cell more durable in higher-pressure. Previously, only one material of BeCu was used and it has the maximum pressure of near 2 GPa due to the deformation of the pressure cell. However, hybrid piston cylinder cell can reach up to 4 GPa with small deformation. It is very useful to study several materials especially heavy-fermion materials whose quantum critical point is near 2 – 3 GPa [1].

In figure 3.1.1, we can find inner structure of hybrid piston cylinder cell. Electrical leads (red lines) connect between samples and electronics. Two samples are mounted simultaneously in the Teflon cup to calibrate pressure inside of

pressure cell. We used Pb metal as a pressure calibrator. Pb is type-I superconductor with superconducting transition temperature T_C of ~7.2 K. As pressure increases T_C decreases linearly with the slope of dT_C/dP = -0.361/GPa [2]. However, we can measure the pressure only near T_C of Pb metal. In this cell, pressure is decreased about 0.2 GPa with decrease of temperature from 300 K to 2 K [3] because pressure transmitting medium shrinks as temperature decreases. We can use two different kinds of pressure transmitting mediums of solid medium and liquid medium to apply uniaxial and hydrostatic pressure, respectively. When we want to apply uniaxial pressure, we use stycast as a solid medium. On the other hand, we use Daphne 7373 oil to apply hydrostatic pressure before solidifying of the liquid medium in the room temperature. The solidification pressure of Daphne 7373 oil is 2.2 GPa in the room temperature [3].

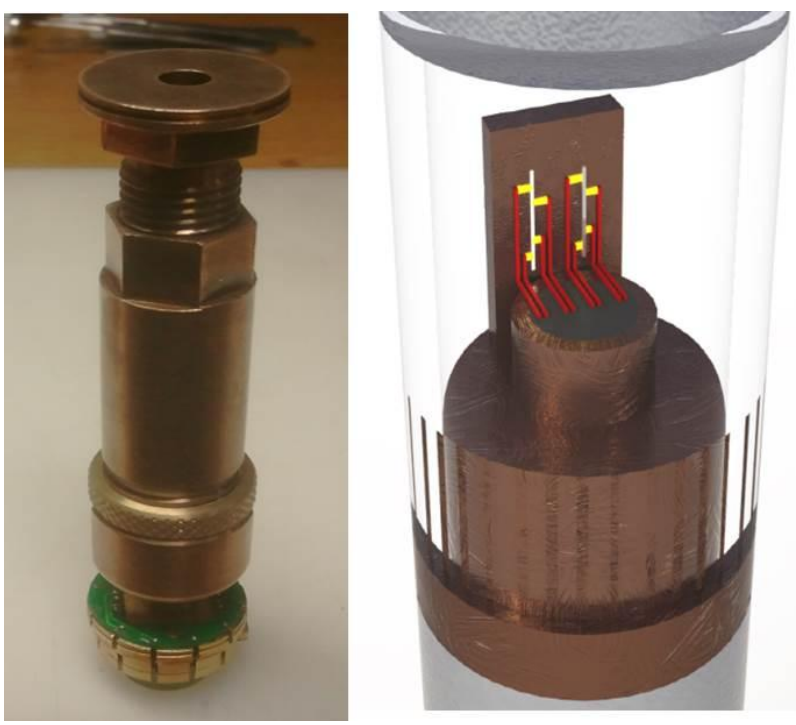

Figure 3.1.1 Hybrid piston cylinder cell and its inner structure. Sample and pressure calibrator Pb metal are loaded in the sample space, simultaneously.

Using hybrid piston cylinder cell, bigger than 2 mm sample can be mounted and several samples more than three samples can be measured at the same time. Using cryostat such as PPMS^{TM}, This cell can reach low temperature down to 2 K and apply magnetic field up to 9 T. Advantage of this cell is the convenience compare to other cells due to its bigger sample space and multiple samples measurement in the single measurement sequence. On the other hand, disadvantage of this cell is the maximum pressure range. Usually, this cell can reach to 3 – 4 GPa as a maximum pressure. At higher than this pressure, cell starts to deform and oil leaking begins. Thus, if we want to study higher pressure physical phenomena, we should use different type of the pressure cell.

3.2 Bridgman anvil cell

In previous section, we reported about disadvantages of hybrid anvil cell. This is mainly due to the maximum pressure range. To overcome maximum pressure issue, we can use Bridgman anvil cell. Bridgman cell is basically the same as piston cylinder cell but smaller sample space with diameter of ~ 2 mm and thickness of 0.2 mm. sample space is capsulated by Teflon ring and pyrophilite gasket indicated in figure 3.2.1.

Figure 3.2.1 Bridgman anvil cell and its inner sample space. Sample and pressure calibrator Pb are loaded in the same sample space. Pressure transmitting medium is captured by Teflon ring and Pyrophyllite gasket.

Using Bridgman anvil cell we can reach to the maximum pressure up to 8 GPa with liquid pressure medium. Pressure inside of sample space is calibrated by T_C of Pb metal.

3.3 Diamond anvil cell

Above two kinds of pressure cells have the limitation of pressure due to deformation or breakdown of anvils. To overcome this problem, many research groups have developed diamond anvil cell (DAC). DAC equipped diamonds which is the strongest material as an anvil. Two diamond anvils should be perfectly aligned, unless diamonds are likely to be broken. BeCu or steel gasket is load at the center of DAC as indicated in figure 3.3.1. After that, we pressurize the metal gasket to pre-indent a hole. Sample is loaded inside of this hole with electrical contacts before pressurizing. In DAC, we usually use NaCl or c-BN as a solid

medium, or silicon oil or Daphne oil as a liquid medium. DAC pressure technique is very useful, when it comes to the maximum pressure range. The world's highest pressure obtained by diamond anvil cell is higher than 300 GPa which value is comparable to pressure of the center of Earth. In addition, the merit of the diamond anvil cell is transparent in the visible light range. Thus, Raman spectroscopy or photo luminescence measurement is possible due to its transparency in the visible light region.

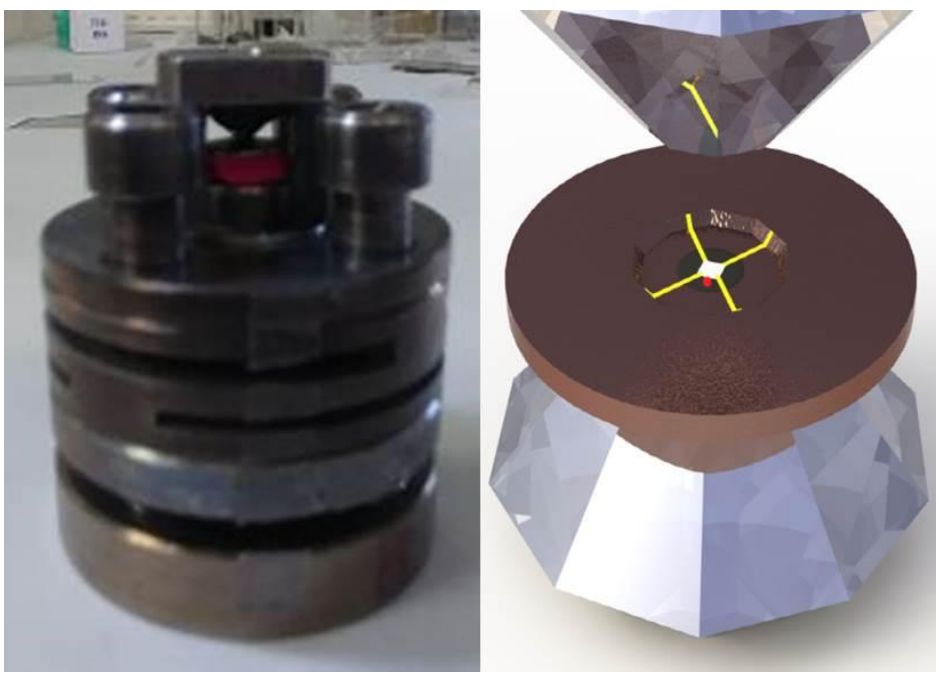

Figure 3.3.1 Diamond anvil cell and its inner structure. Two opposite diamonds press sample and ruby.

Pressure calibration of DAC is calculated by ruby photo luminescence measurement at room temperature. Ruby has two peaks near 694 nm and it evolves to high wave length as pressure increases. Pressure is calibrated by P(GPa) = $A/B[\{1+\Delta\lambda/\lambda_0\}^B-1$ where, A = 19.04 MPa, B = 7.665, λ_0 = 694.22 nm and $\Delta\lambda$ is a shift of wave length [4].

3.4 Cubic anvil cell

Hybrid piston cylinder cell, Bridgman anvil cell, and diamond anvil cell press the sample along one-direction, usually *c*-axis. In this case, hydrostatic pressure can be applied only in the liquid medium. However, all liquid medium are solidified at high-pressure regime in turn unexpected uniaxial pressure must be involved. To remove this problem, liquid medium with higher solidification pressure is necessary. Typical liquid pressure medium we used is Daphne 7373 oil whose solidification pressure is near 2.2 GPa at room temperature. If we need different pressure transmitting oil with higher solidification pressure such as Daphne 7474 or Daphne 7575, we can realize hydrostatic pressure higher than 2.2 GPa. Another way is to increase temperature higher than room temperature just after pressurizing to increase solidification pressure. However, techniques mentioned above still have limitation because these liquid medium solidifies lower than 5 GPa.

To solve this pressure quality problem, cubic anvil cell technique was introduced. Cubic anvil cell has six anvils and they press in the six directions with exactly the same force. This procedure can remove uncontrollable uniaxial pressure, even after solidification of liquid medium.

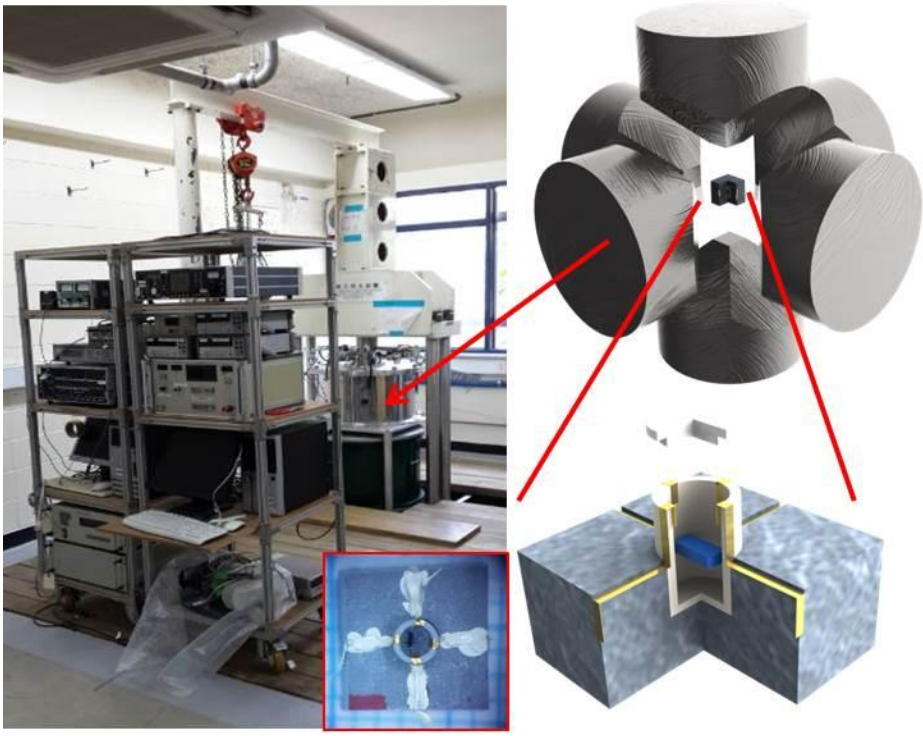

Figure 3.4.1 Cubic anvil cell apparatus and orientation of six anvils. The sample is loaded in the Teflon cup with Daphne 7373 oil pressure medium. Pyrophyllite cube gasket covers outside of Teflon cap.

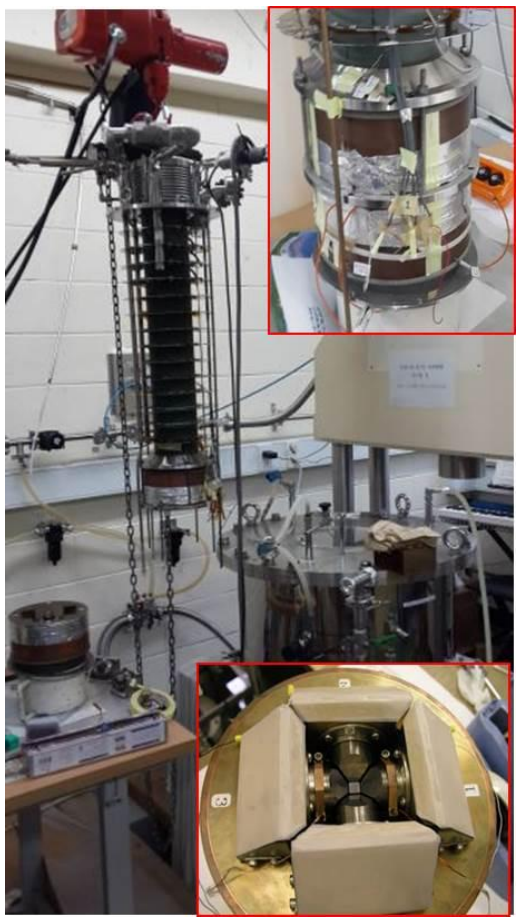

Figure 3.4.2. Main pillar of cubic anvil cell. Four anvils play an important role as electrical contacts. We press the sample space through the outside press unit.

Cubic anvil cell has two different kinds of gasket, one is a pyrophilite cube, and another is Teflon cup and cap. In cubic anvil cell, dimension of Teflon cup and pyrophilite gasket is very important. At the first time, we used feflon cup with 4 mm length, 2.5 mm inner diameter, and 3 mm outer diameter. However, we have failed to pressurize due to oil leakage problem. Thus, we did the computer simulation using COMSOL Multiphysics® modeling software to solve this problem. In this simulation, we used the same dimensions and the same materials to actual gasket. We found severe deformation at the corner of Teflon cup and wall of

pyrophilite gasket in our initial gasket design (Figure 3.4.3.). We simulated many different dimensions and found an appropriate dimension of feflon cup (Figure 3.4.4.). New and stable dimensions of Teflon cup are 3 mm length, 1.5 mm inner diameter, and 2 mm outer diameter.

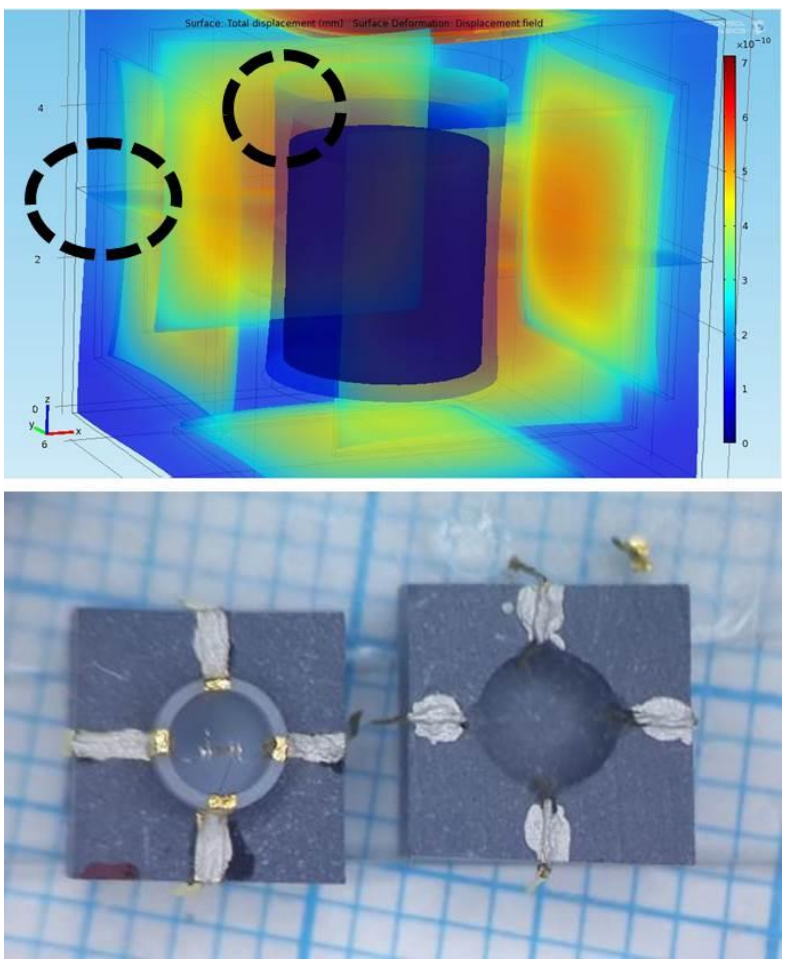

Figure 3.4.3. COMSOL Multiphysics simulation and pyrophilite gasket design with dimension of 3 mm outer diameter and 4 mm length. In the computer simulation, severe deformation was observed on the wall of the gasket.

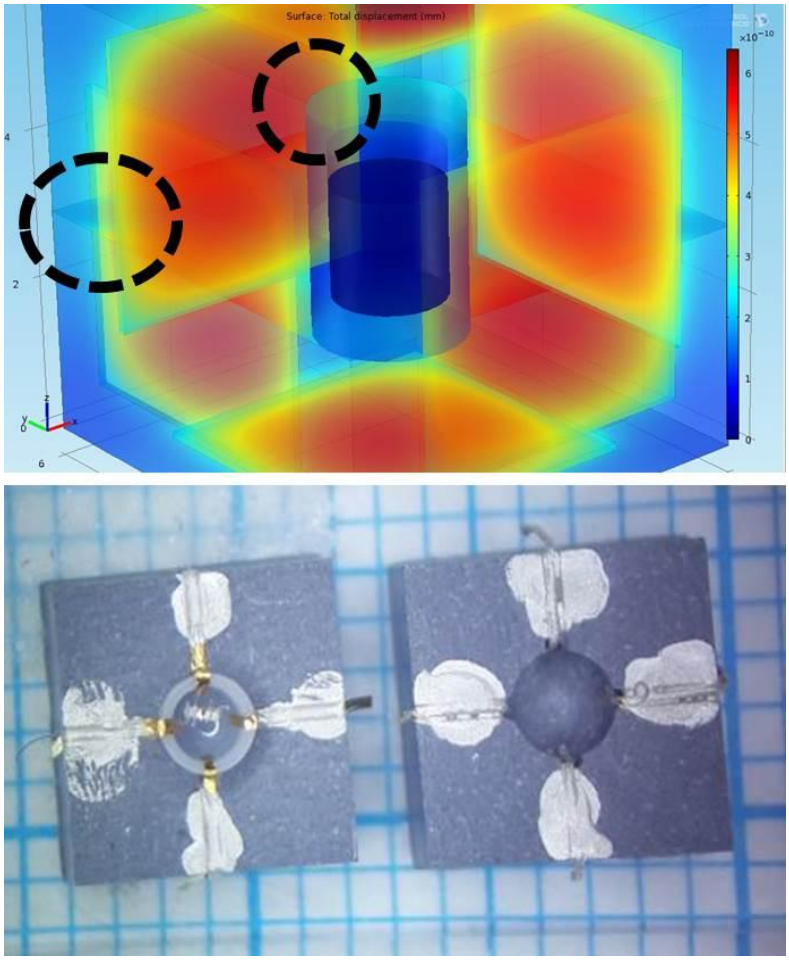

Figure 3.4.4. COMSOL Multiphysics simulation and pyrophilite gasket design with dimension of 2 mm outer diameter and 3 mm length. In the simulation, the deformation at the wall is negligible.

Gold wire and gold foil are used as electrical contacts. When sample loading is completed, pyrophilite cube was mounted inside of six different anvils and pressurize. Cubic anvil cell (CAC) is not piston-type pressure cell such as hybrid piston cylinder cell, Bridgman cell, or diamond anvil cell. Thus, we should cool down all parts of cubic anvil cell and liquid helium consumption is very huge.

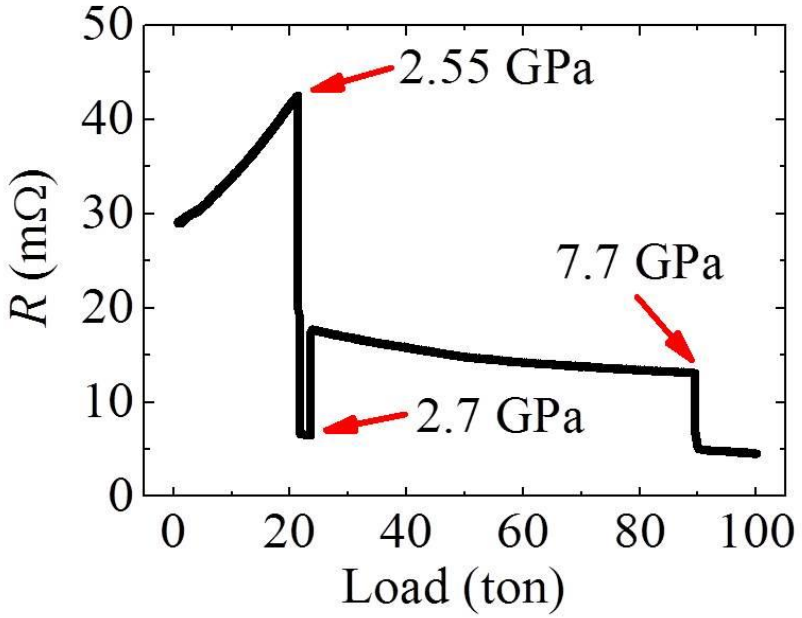

Figure 3.4.5. Three first-order transitions of Bi metal were observed at 2.55, 2.7, and 7.7 GPa in room temperature up to 100 tons.

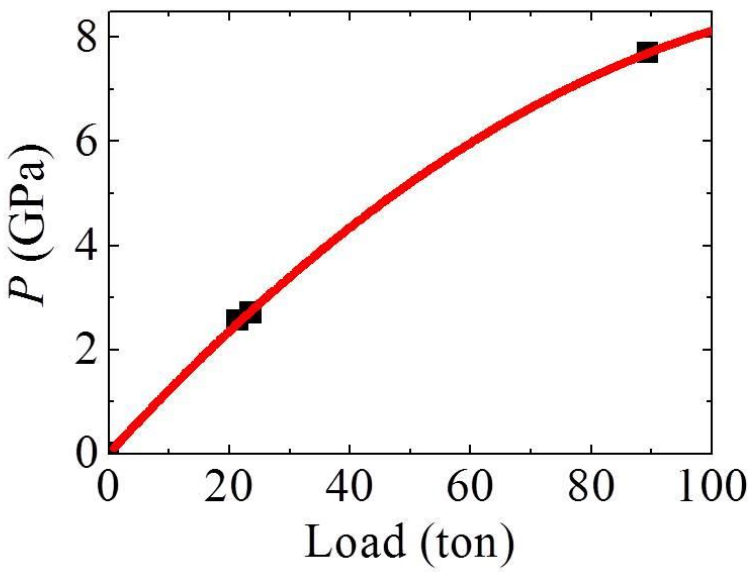

Figure 3.4.6. Three Bi metal transitions calibration curve. We can adjust pressure inside of six anvils by changing pressure from by outside pressure unit.

Pressure is calibrated by three kinds of 1st order transitions of Bi-metal. Bi-metal has characteristic 1st order structure transitions at specific pressure. In figure 3.4.5, we found three transition pressures at 2.55, 2.7, and 7.7 GPa. Pressure in the sample space can be calibrated using this points and controlled the load of the sample space. In this calibration, we can apply up to 8.5 GPa due to lack of calibration points. If we want to reach to higher than 10 GPa, we use Sn-metal, which has higher transition pressure in the room temperature.

Bibliography

[1] Tuson Park *et al*. *Nature* **440** 65 (2006)

[2] T. F. Smith and C. W. Chu, Phys. Rev. **159** 353 (1967)

[3] Keiichi YOKOGAWA *et al*. Japanese Journal of Applied Physics **46** 3636 (2007)

[4] H. K. Mao. *et al*. Journal of geophysical research **91** 4673 (1986)

4. Quasi two-dimensional materials

4.1 Introduction

In this chapter, we will report transport properties of quasi two-dimensional superconductors under high-pressure. Three different superconductors 1) 2*H*-Pd_xTaSe_2, 2) $Ca_{0.9}La_{0.1}FeAs_2$, and 3) $BaFe_2(As_{1-x}P_x)_2$ show general phenomena such as an enhancement of T_C and a suppression of density wave behaviors.

The quasi two-dimensional materials have strong correlation along *ab* plane, whereas small correlation along *c*-axis. Generally, lattice suppression along *c*-axis is larger than *a* or *b*-axis, since contraction of Weak van der Waals bonding layer is larger than that of ionic bonding layer. This unequal compressibility induces several interesting behaviors.

4.2 2*H*-Pd_xTaSe_2

The layered transition metal dichalcogenides (TMDs) with a chemical formula MX_2 where M is a transition metal atom (M = Ti, Zr, Hf, V, Nb, Ta, Mo, W and Re) and X is a chalcogen atom (X = S, Se, and Te) have been extensively studied due to their novel electronic properties resulted from their low-dimensionality [1-3]. Each layer consists of a hexagonal transition metal layer sandwiched by two chalcogen layers and layers are coupled by weak van der Waals force [4]. MX_2 materials exhibit charge-density wave (CDW), Mott metal insulator transition, or superconductivity [1-3]. In these materials, superconductivity emerges in the vicinity of the CDW quantum phase transition induced by

intercalation of various elements into the van der Waals gaps [5-10], and by the application of pressure or gate voltage to the pristine compound [11-13]. Previous reported electronic phase diagram as a function of doping, gate voltage or pressure suggests possible role of the CDW quantum critical point on the emergence of superconductivity.

The 2*H* structure of tantalum diselenide ($TaSe_2$) is well-known CDW system, in which an usual metallic state at high temperatures enters into an incommensurate charge density wave (ICDW) phase near T_{ICDW} ~ 122 K, followed by a commensurate charge density wave (CCDW) phase near T_{CCDW} ~ 90 K [14-16]. In figure 4.2.1, 2*H*-Pd*x*$TaSe_2$ (x = 0.0) exhibits superconductivity in the CDW phase near T_C ~ 0.14 K and it enhanced up to 3.3 K with Pd intercalation of 9 % between van der Waals layers [4].

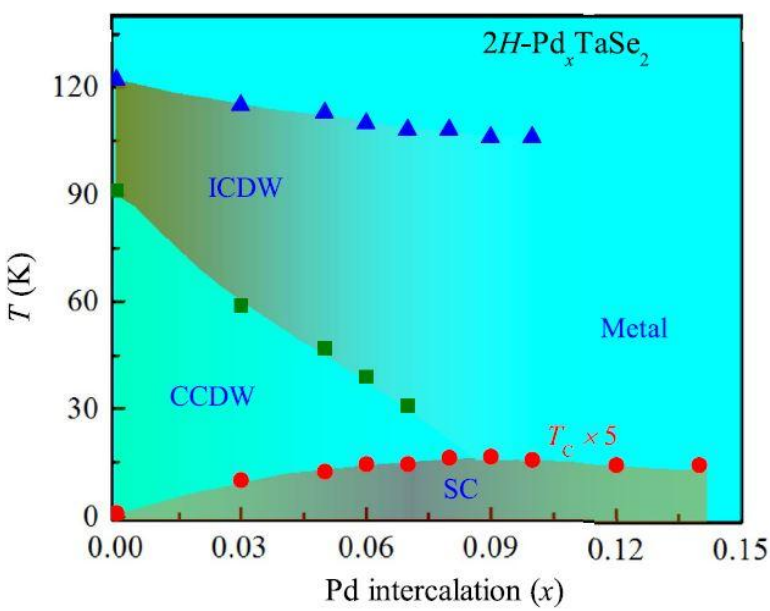

Figure 4.2.1 *x*-*T* phase diagram of poly-crystalline Pd$_x$$TaSe_2$. The CCDW is fully suppressed near 8 % intercalation rate and T_C reach up to 3.3 K at the optimal intercalations of 9 % [4].

In 2*H*-Pd_xTaSe_2 system, Pd goes into $TaSe_2$ material in two different ways; doping or intercalation. Previous study of lattice constant of poly-crystalline 2*H*-$TaSe_2$ shows that lattice constants of *a* and *c* increases as Pd contents increase. If Pd ions doped into Ta sites, lattice constant of *a* must be reduced due to different atomic sizes between Pd and Ta. However, lattice constant of *a* and *c* both increase with Pd contents indicating Pd is intercalated rather than doping into van der Waals layers [4].

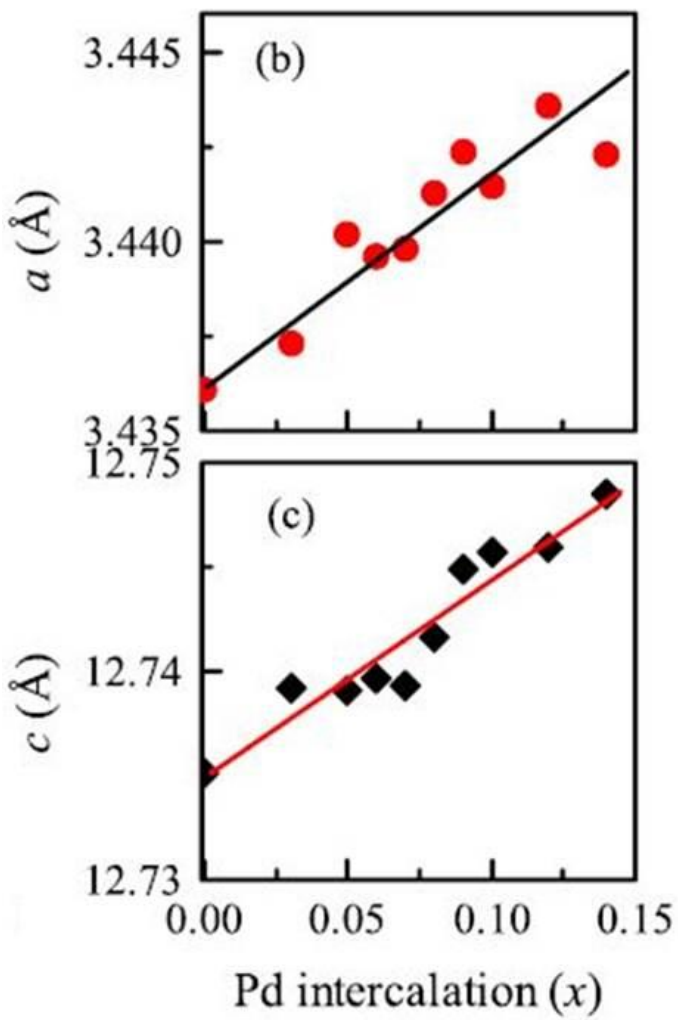

Figure 4.2.2 Evolution of *a* and *c* lattice constants as a function of Pd intercalation. Both *a* and *c* lattice constants are increased by Pd intercalation [4].

Moreover, superconductivity in this material is sensitive to c/a ratio, since it can modify electronic band structure. The relation between c/a ratio and T_C will be discussed in next section. We measured transport property of 2*H*-Pd_xTaSe_2 under high-pressure to find the evolution of CDW and superconductivity.

4.3 High-pressure effect of Pd_xTaSe_2

We have investigated in-plane resistivity of the 2*H*-Pd_xTaSe_2 single crystals with nominal intercalation rate of x = 0.02, 0.03, 0.05, and 0.06 under hydrostatic pressure up to 8.5 GPa using hybrid piston anvil cell and cubic anvil cell. In addition, higher pressure measurement up to 37.7 GPa using diamond anvil cell was investigated in x = 0.06 sample.

Experimental

Single crystals of 2*H*-Pd_xTaSe_2 with a nominal concentration of x = 0.03 and 0.05 by a chemical vapor transport method using $SeCl_4$ as a transport agent as reported previously [4]. The grown single crystals of a few millimeters in their lateral dimensions were cut into a rectangular shape. Conventional four prove method was used using silver phase (Dupont 4929N^{TM}). Hybrid piston cylinder cell and PPMS^{TM} (Quantum design) were used to measure resistivity down to 2 K in the low-pressure regime and cubic anvil cell covers high-pressure regime up to 8.5 GPa. We used diamond anvil cell to measure electrical resistivity and Hall effect up to 37.7 GPa. In hybrid piston cylinder cell and cubic anvil cell pressure measurements, Daphne 7373 oil was used as a pressure medium. However, silicon oil was used for diamond anvil cell. The solidification pressure of Daphne 7373 oil is near 2.2 GPa in the room temperature [17].

Results and discussion

Figure 4.3.1(a) shows the temperature-dependence of the in-plane resistivity $\rho_{ab}(T)$ of 2*H*-Pd_xTaSe_2 single crystals with nominal intercalation of x = 0.03 and 0.05. Three phase transitions can be observed in the $\rho_{ab}(T)$ data of the 2*H*-$Pd_{0.03}TaSe_2$. Resistivity kink near 120 K corresponds with charge density wave transition. In $d\rho_{ab}(T)/dT$ curve, we can observed three different anomalies; 1) ICDW transition, 2) CCDW transition, and 3) Fermi-liquid transition, indicated by arrows (figure 4.3.1(b)). The determined T_{ICDW} at 117K, T_{CCDW} at 91 K, and T_{FL} at 28 K shows the similar values to previous reported values obtained from poly-crystalline samples [4]. On the other hand, x = 0.05 single crystal, ICDW and CCDW transitions are absent and only shows superconductivity transition. T_C obtained from 50 % of the normal state resistivity is 3.3 K (figure 4.3.1(c)) and this value is larger than T_C of x = 0.03 sample, whose T_C is 2.14 K. In poly-crystalline sample, CDWs disappear at the intercalation concentration higher than x = 0.08. This result suggests that an actual chemical intercalation rate is much higher than 0.05. The comparison between T_C of poly-crystalline samples and single crystal samples indicates that actual intercalation rate of 0.05 sample is 0.08.

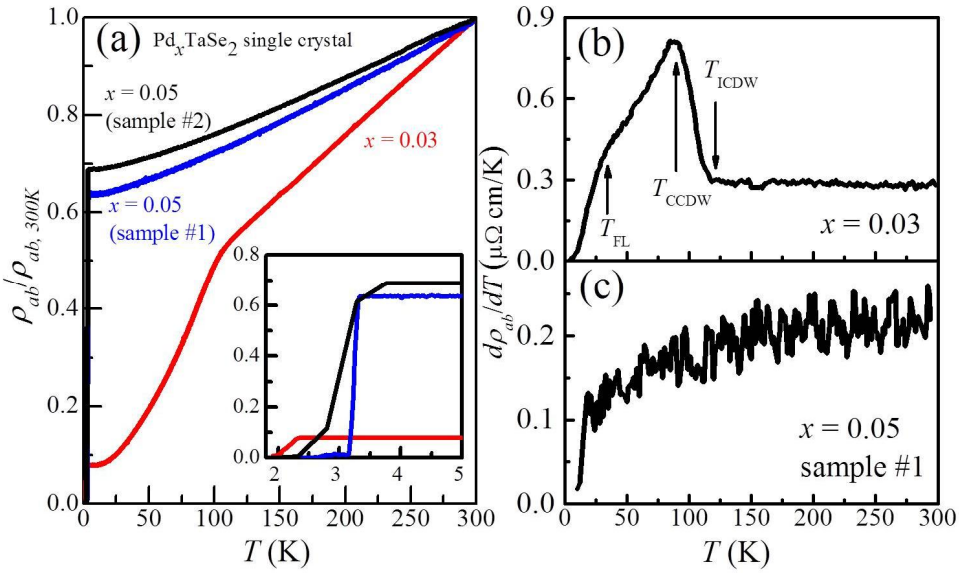

Figure 4.3.1. (a) Electrical resistivity of x = 0.03 and x = 0.05 intercalation single crystal samples. CDWs are observed at x = 0.03 crystal, while x = 0.05 CDWs are disappeared. Both samples show superconductivity near 2 K. (b) T_{FL}, T_{CCDW}, and T_{ICDW} can be obtained from derivatives of resistivity in x = 0.03 crystal. (c) CDW orders are not observed at x = 0.05 crystal [25].

Figure 4.3.2 (a) and (b) show the temperature dependence of the resistivity of 2*H*-Pd_xTaSe_2 samples up to 1.82 GPa for nominal intercalation rate of x = 0.03 and x = 0.05 samples. For x = 0.03, ICDW and CCDW transition temperature decreases with pressure up to 1.82 GPa. Both samples show linear increase of T_C under pressure.

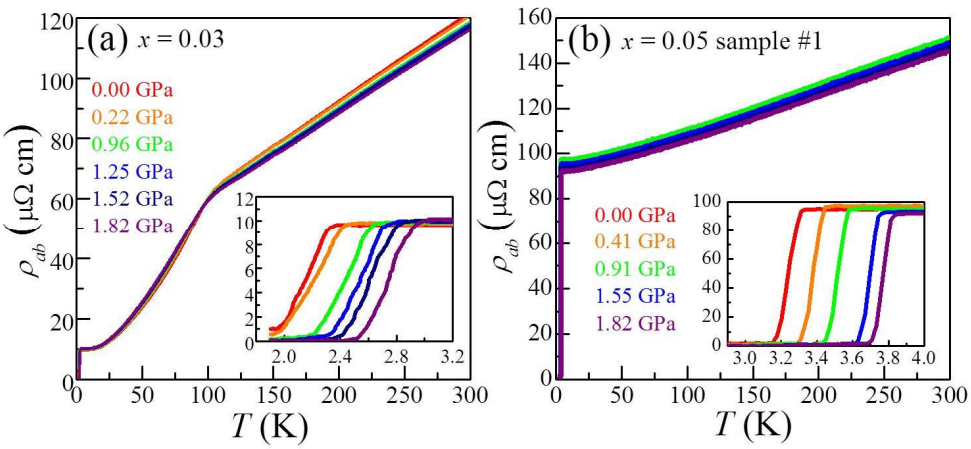

Figure 4.3.2 (a) and (b) Electrical resistivity of $x = 0.03$ and $x = 0.05$ intercalation samples under high-pressure using hybrid piston cylinder cell. CDW orders are suppressed with pressure in the $x = 0.03$ sample. Both samples show linearly increase of T_C up to maximum pressure of hybrid piston cylinder cell [25].

To investigate the evolution of the T_C at higher pressure, we performed transport measurements of 2*H*-$Pd_{0.05}TaSe_2$ single crystal collected from the same batch using cubic anvil cell. Measured crystal shows broad superconducting transition and two-step behavior, probably due to the inhomogeneous intercalation of the Pd ions. However, irrespective of the sample quality, the evolution of the superconducting phase at higher pressures can be obtained from figure 4.3.3. Parallel shift of the T_C towards higher temperature implies good hydrostatic quality of applied pressure. The maximum T_C of $x = 0.05$ sample is 5.01 K which corresponds to the highest value among 2*H*-Pd_xTaSe_2 crystals and it is 36 times larger value compared to pristine 2*H*-$TaSe_2$ crystal.

The overall *p*-*T* phase diagrams for x =0.03 and $x = 0.05$ are indicated in figure 4.3.4(a) and 4.3.4(b), respectively. For $x = 0.03$ sample, T_{ICDW} changes from

117 K at 0 GPa to 113 K at 1.8 GPa and T_{CCDW} changes from 91 K at 0 GPa to 77 K at 1.8 GPa. The linear increase of T_C with pressure was observed in both crystals and CDW orders compete the superconductivity. Interestingly, no saturation of T_C was observed up to 8.0 GPa, suggesting T_C can be enhanced under higher pressure.

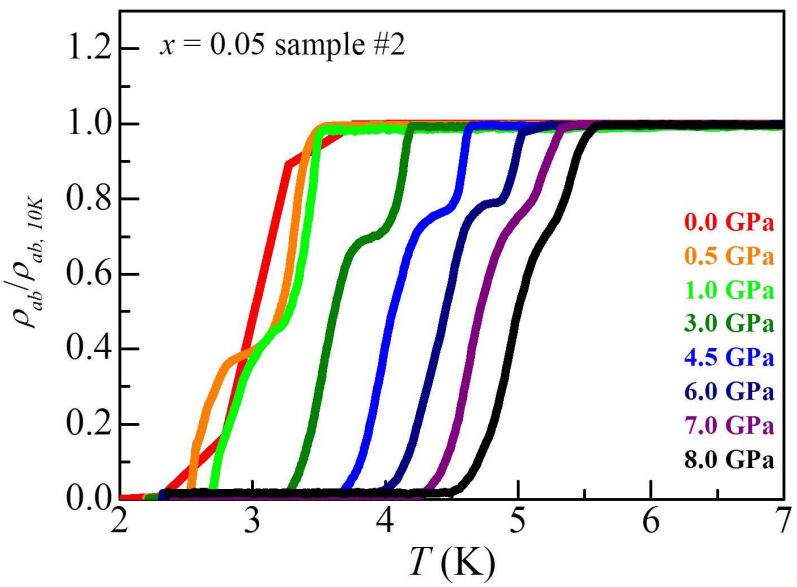

Figure 4.3.3. Higher pressure resistivity measurement of 5 % crystal measured by cubic anvil cell shows no saturation of T_C up to 8.0 GPa [25].

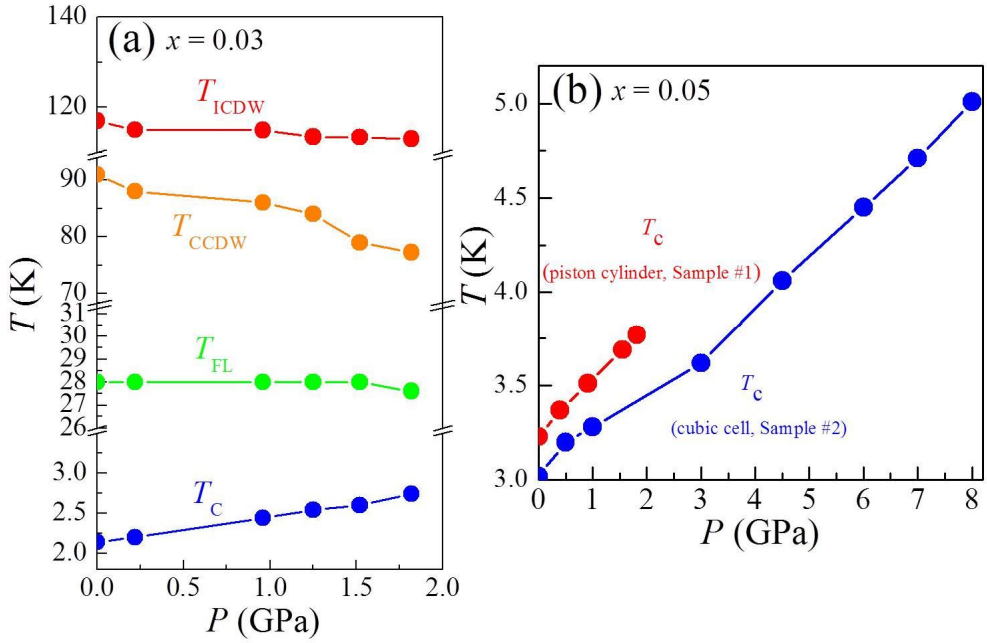

Figure 4.3.4. Overall phase diagrams of $x = 0.03$ and $x = 0.05$ single crystals under high-pressure. (a) In $x = 0.03$ sample, ICDW and CCDW decrease with pressure, while T_C increases linearly. (b) In $x = 0.05$ sample, T_C increases linearly up to 8 GPa with no saturation, while CDWs orders are not observed [25].

To study other intercalation rate samples, high pressure effect of Pd_xTaSe_2 (x = 0.02, 0.06) single crystals for different batch samples have been measured using cubic anvil cell. Intercalation rates are determined by comparison of T_C to poly-crystalline samples. In different batch samples, different transport agents are used during single crystal growth. Previously used $SeCl_4$ transport agent was replaced to $PdCl_2$ for new batch sample growth. T_C of newly grown single crystals shows comparable value to poly-crystalline samples as shown in Figure 4.3.5 and 4.3.7 for $x = 0.02$ and 0.06.

We have measured two different intercalation rate samples; 0.02 and 0.06. Electrical resistivity of Pd_xTaSe_2 shows that T_C increased almost linearly with rate

of 0.365 K/GPa and 0.344 K/GPa for 0.02 and 0.06 intercalation contents, respectively (figure 4.3.5 and 4.3.7).

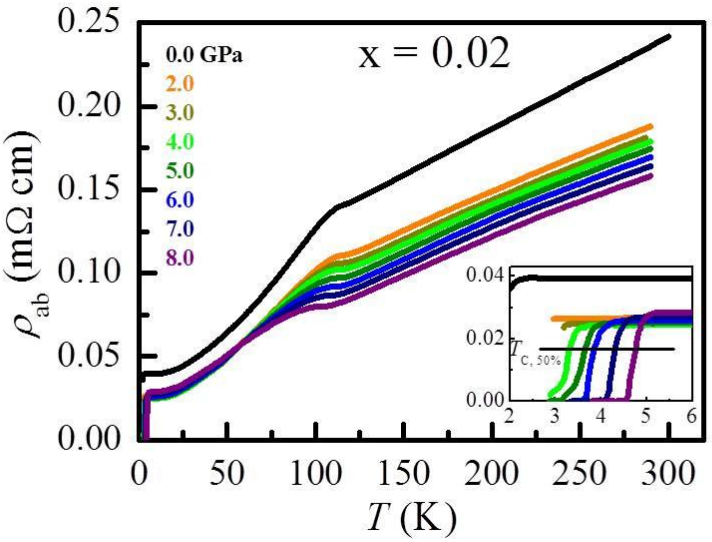

Figure 4.3.5. Resistivity of $x = 0.02$ intercalation sample grown by $PdCl_2$ flux shows the suppression of CDWs and the enhancement of T_C up to 8.0 GPa.

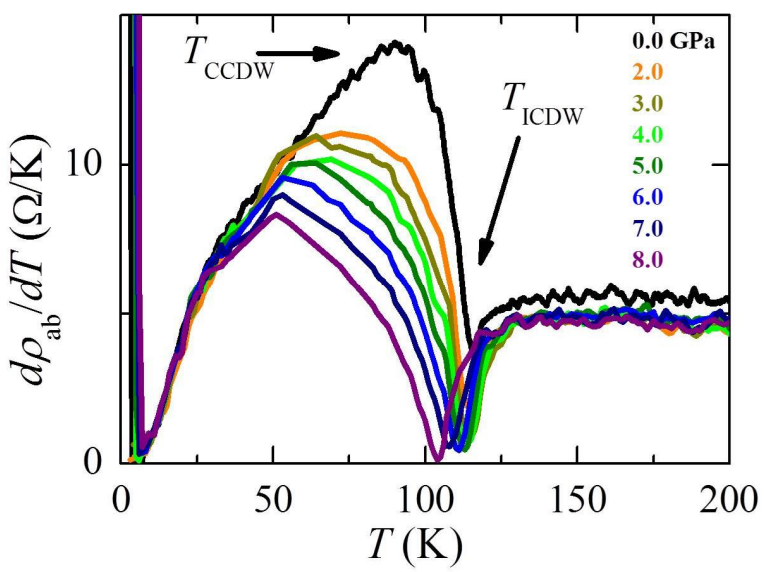

Figure 4.3.6. Temperature derivative of the resistivity of $x = 0.02$ intercalation single crystal. T_{ICDW} is defined by the minimum point and T_{CCDW} is defined by the maximum point.

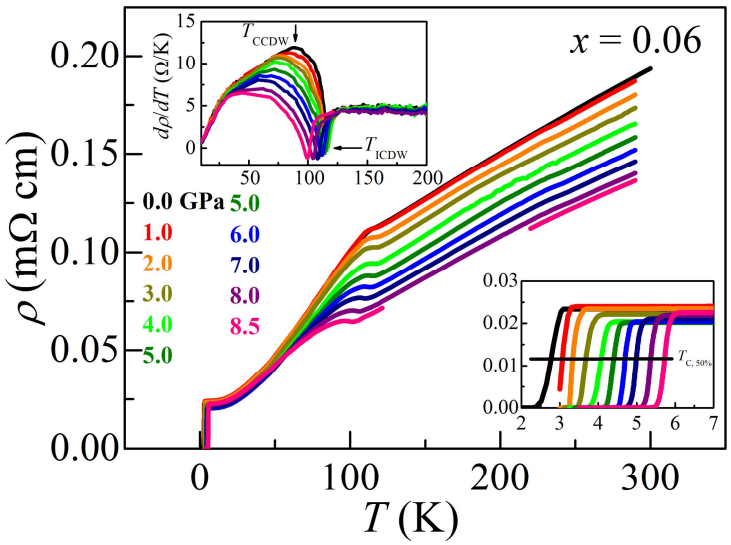

Figure 4.3.7. Resistivity of 6 % intercalation sample grown by $PdCl_2$ flux shows the suppression of CDWs and the enhancement of T_C up to 8.5 GPa.

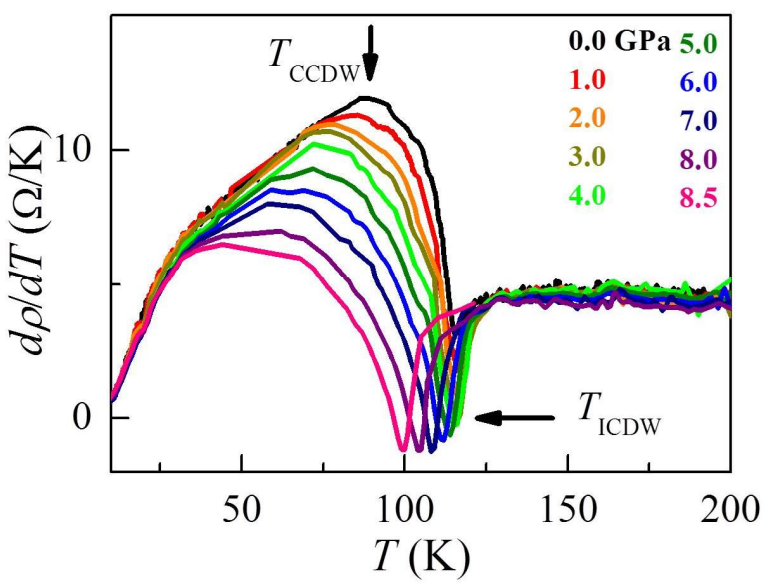

Figure 4.3.8. Temperature derivative of the resistivity of x = 0.06 intercalation single crystal. T_{ICDW} is defined by the minimum point and T_{CCDW} is defined by the maximum point.

In figure 4.3.6 and 4.3.8, derivatives of resistivities are indicated. ICDW and CCDW can be obtained from the minimum point and the broad maximum point as defined previously.

Overall phase diagrams of newly grown single crystals were indicated in figure 4.3.9 and figure 4.3.10. As we mentioned previously, decrease of ICDW and CCDW transition temperature and the enhancement of T_C with pressure in both sample of x = 0.02 and x = 0.06. Pressure coefficient defined by dT_C/dP shows different values in the different intercalation rate. Faster increase of T_C observed in the lower interaction rate. Following this results, CDW orders seems to compete with superconductivity but higher pressure experiments is necessary to confirm that which CDW orders compete with superconductivity.

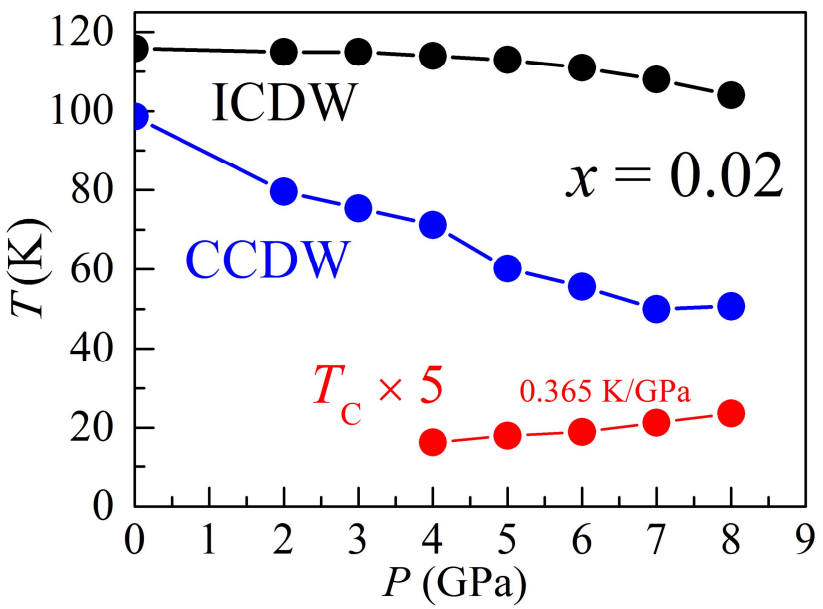

Figure 4.3.9. p-T phase diagram of x = 0.02 intercalation Pd_xTaSe_2 single crystal. Both ICDW and CCDW temperatures decrease with pressure. T_C is enhanced under pressure with a rate of 0.365 T_C/GPa.

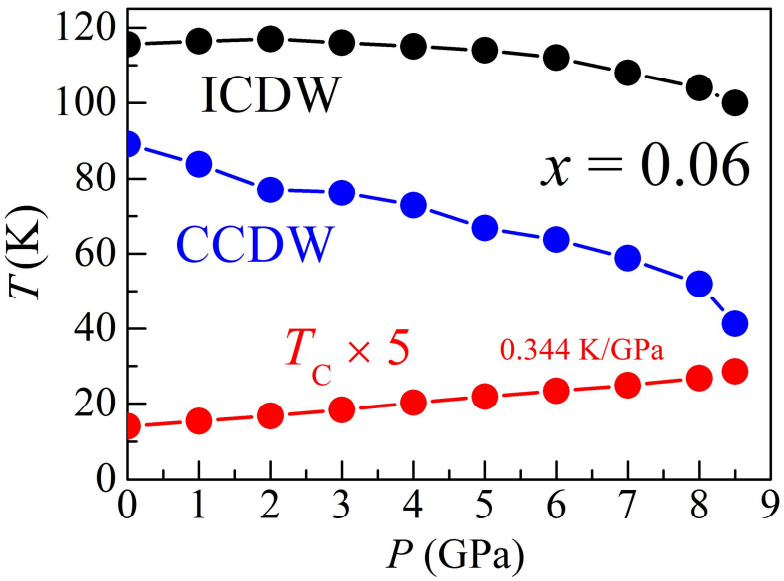

Figure 4.3.10. *p*-*T* phase diagram of $x = 0.06$ intercalation Pd_xTaSe_2 single crystal. Both ICDW and CCDW temperatures decrease with pressure. T_C is enhanced under pressure with a rate of 0.344 T_C/GPa.

To expand the phase diagram of $Pd_{0.06}TaSe_2$ single crystal to higher pressure, diamond anvil cell (DAC) with 300 μm culet size was used. We measured electrical conductivity of $Pd_{0.06}TaSe_2$ single crystal with Prof. Chen's group in HPSTAR (Center for high pressure science and technology advanced research, China).

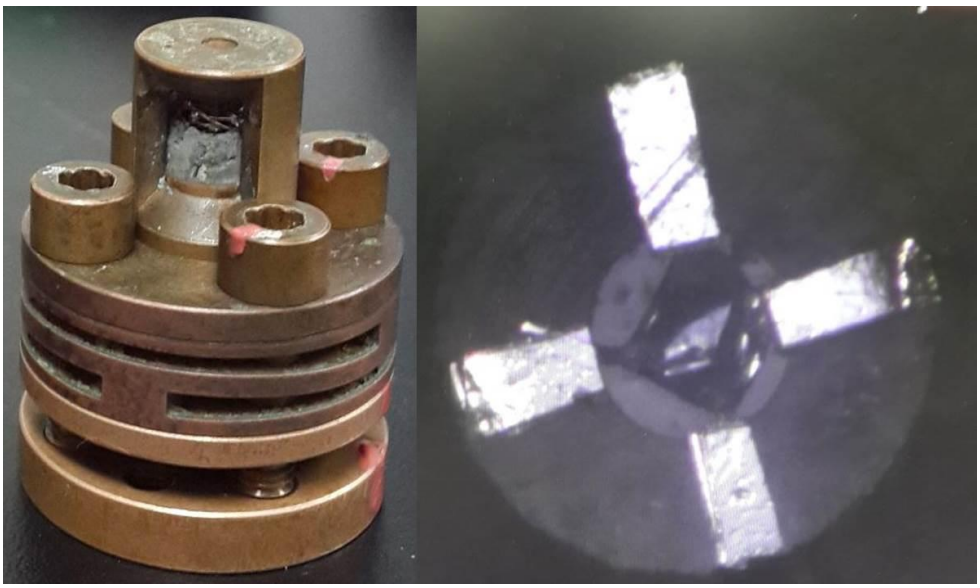

Figure 4.3.11. Diamond anvil cell in HPSTAR. Overall picture of diamond anvil cell is stated in the left. Right picture shows the view of mounted sample in the sample space. The culet size of diamond anvil is 300 μm. The size of the hole is approximately 120 μm and sample size is 70 μm.

DAC in HPSTAR is made from BeCu metal. We used 5 μm Pt foil and room temperature silver epoxy to make electrical contacts. The most noticeable point is the type of pressure transmitting medium. Typically, solid mediums are used for the electrical conductivity measurement in DAC experiments due to the convenience of sample loading. In this case, however, uncontrollable uniaxial pressure is considerably huge and the strain effect became significant. Thus, the reproducibility of each measurement cannot be guaranteed. To solve this problem, we used silicon oil as a pressure medium. After solidification of the liquid silicon oil, it becomes soft solid. Because of this, we wait 2 hours after pressurization to stabilize pressure of the solidified silicon oil. We used four wires with Van der Pauw electrical configuration so two kinds of electrical resistivities denfined in

‘measurement 1’ and ‘measurement 2’ can be obtained. Pressure is calculated by ($P_{\text{before measurement}}$ + $P_{\text{after measeurment}}$)/2 calibrated by ruby PL peaks, since pressure inside of the sample space is increased after cooling-warming cycles. It might come from pressure annealing or reorientation of pressure medium.

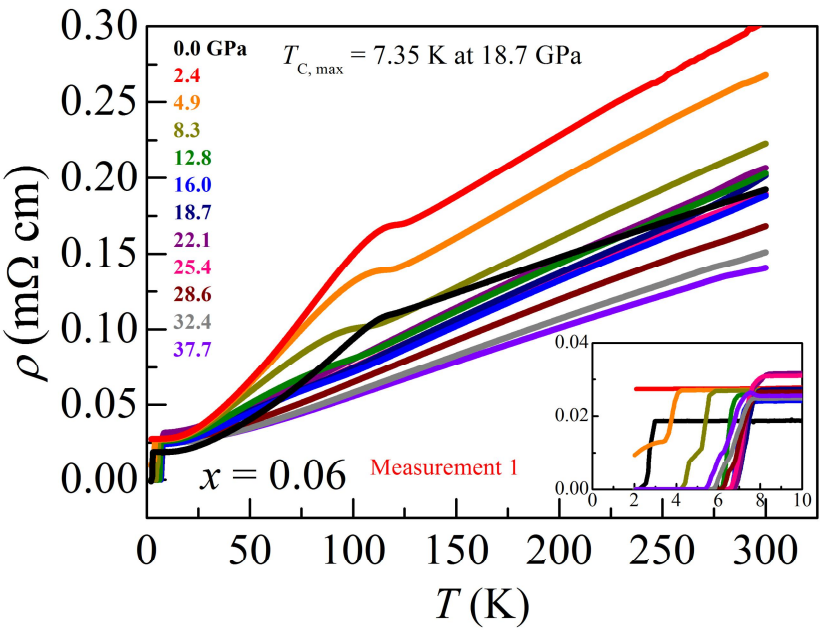

Figure 4.3.12. Electrical resistivity of $Pd_{0.06}TaSe_2$ single crystal under high pressure up to 37.7 GPa using DAC (measurement 1).

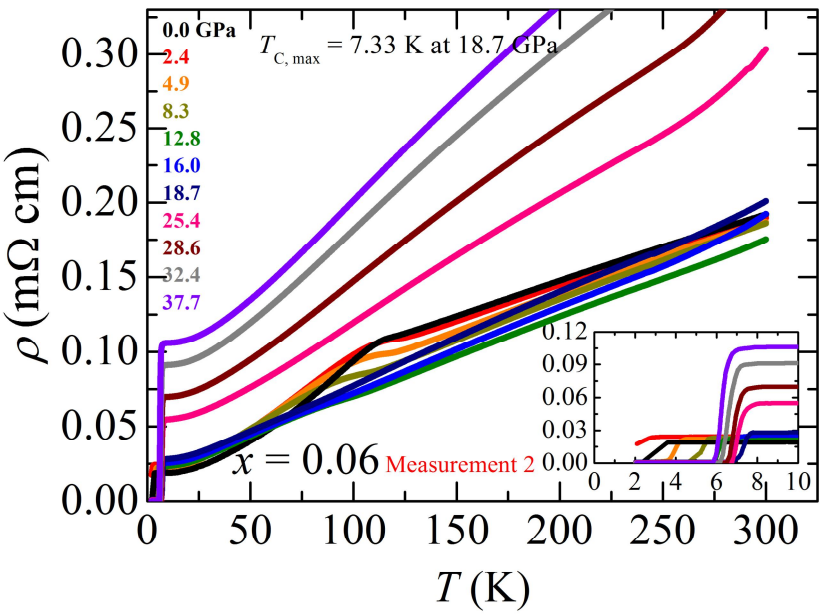

Figure 4.3.13. Electrical resistivity of $Pd_{0.06}TaSe_2$ single crystal under high pressure up to 37.7 GPa using DAC (measurement 2).

In DAC measurement, T_C increased to 7.35 K at the optimal pressure of 18.7 GPa indicated in figure 4.3.12 and 4.3.13. Higher than the optimal pressure, T_C starts to decrease to the maximum pressure we can obtain. To investigate further information, we calculated temperature derivative of $\rho(P, T)$.

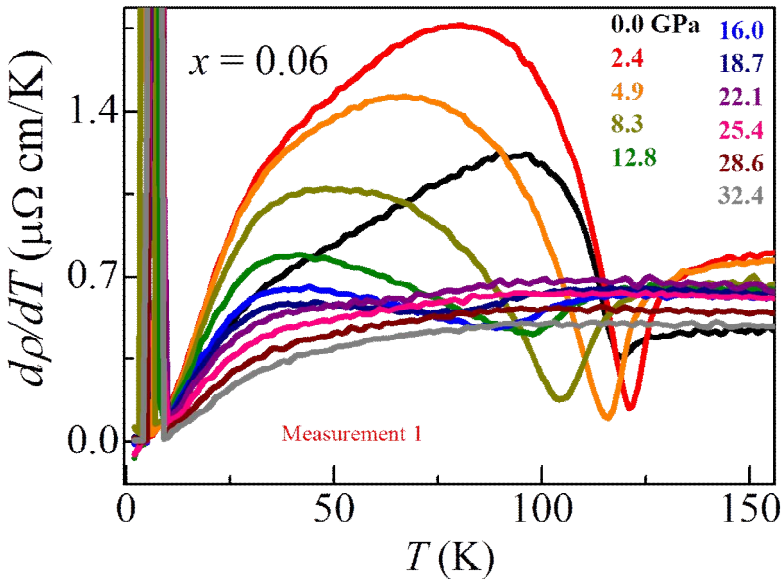

Figure 4.3.14. The derivative of the resistivity of $Pd_{0.06}TaSe_2$ single crystal of 'Measurement 1' under high pressure using DAC.

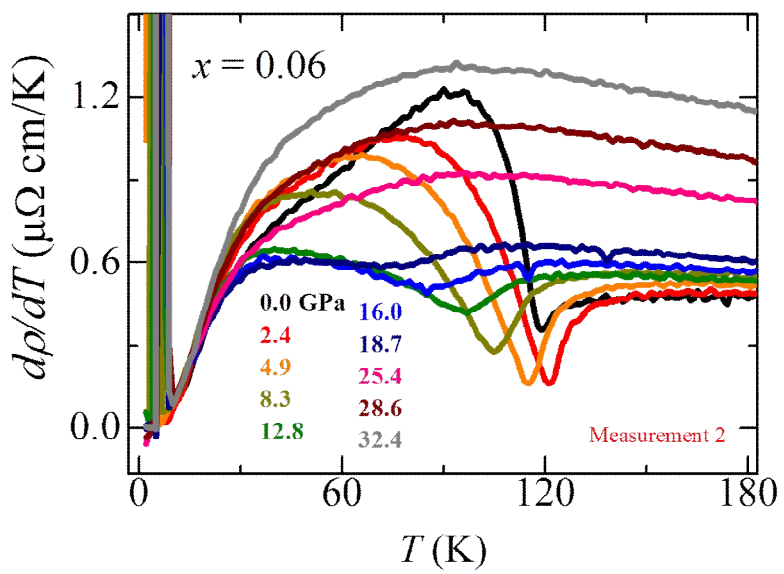

Figure 4.3.15. The derivative of the resistivity of $Pd_{0.06}TaSe_2$ single crystal of 'Measurement 2' under high pressure using DAC.

In figure 4.3.14 and 4.3.15, we observed deeps in the derivative of resistivities which corresponds to ICDW transitions as explained previously. In addition, broad maximums of the derivative correspond to CCDW. However, the broadness of the maximum is getting broader and difficult to recognize at higher pressure.

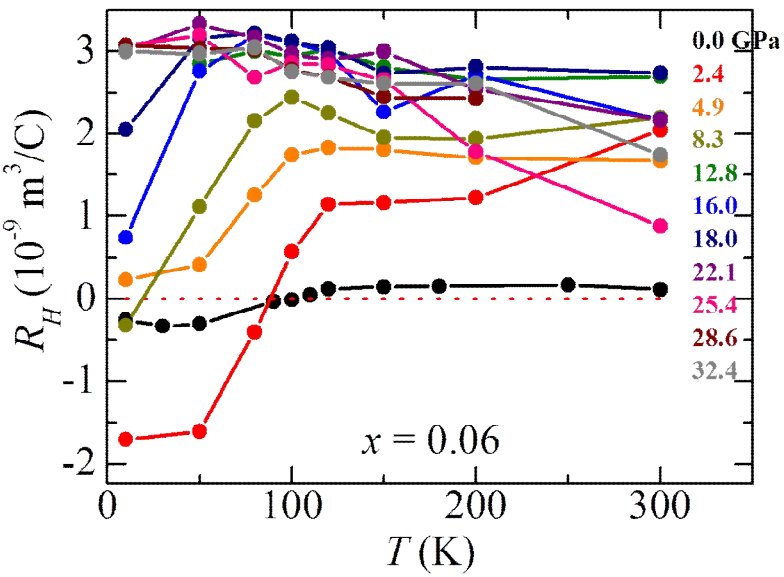

Figure 4.3.16. Hall coefficient of $Pd_{0.06}TaSe_2$ single crystal. In higher temperature, dominant carrier type is hole. However, the sign of the carriers is changed from plus to minus at low temperature and low pressure regime.

To confirm the carrier type of these materials, we measured Hall effect under higher pressure in the selected temperature. Sign change of the Hall coefficient observed at the CCDW transition temperature. Following this definition, the CCDW disappear at 4.9 GPa. Hall coefficients at fixed temperature were chosen to observe the evolution of the Hall coefficient in ground states.

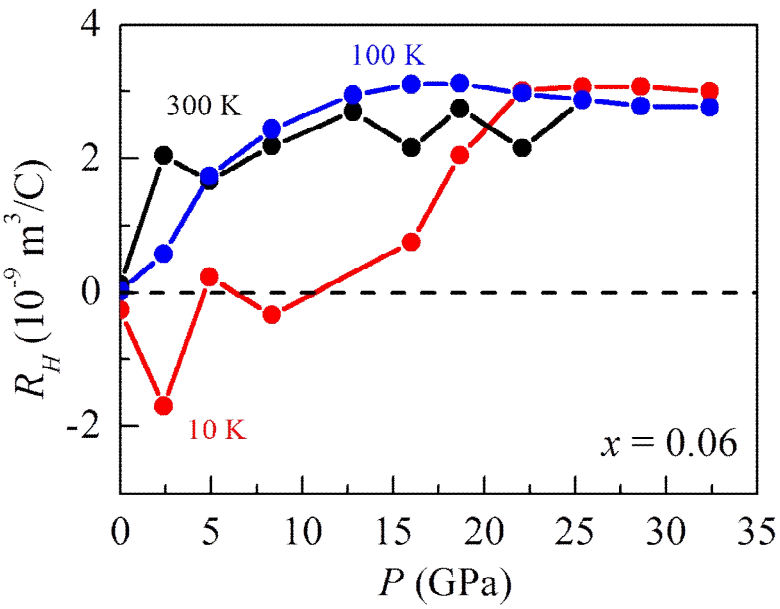

Figure 4.3.17. Hall coefficient of $Pd_{0.06}TaSe_2$ single crystal at selected temperature. At 10 K, the slope change of the Hall coefficient was observed near the optimal pressure.

In figure 4.3.17, we choose the Hall coefficient at selected temperature. At 10 K, the slope changed of the Hall coefficient was observed and it might indicate the Fermi-surface reconstruction. Therefore, we can expect the quantum critical point at this pressure. Further experiment such as high pressure Raman measurement is required to strengthen the existence of the quantum critical point.

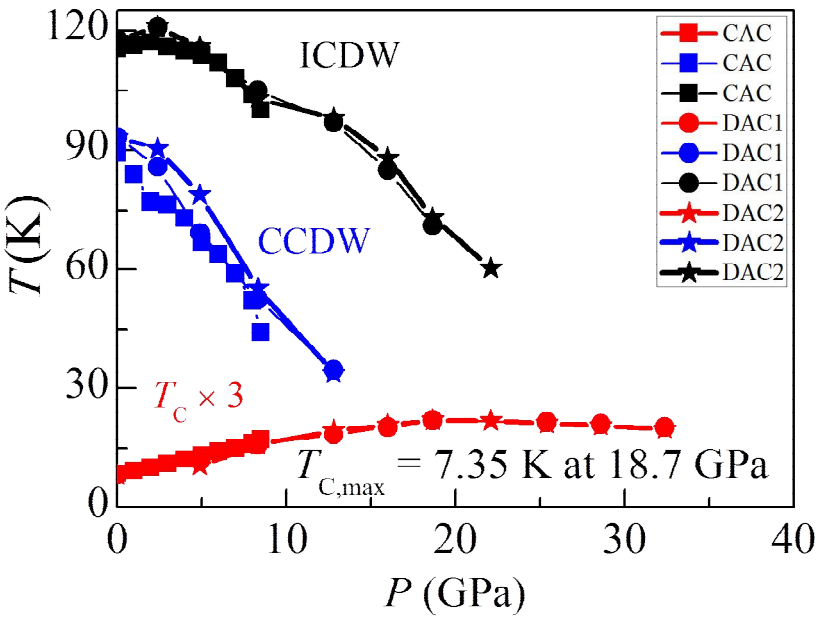

Figure 4.3.18. Overall phase diagram of $Pd_{0.06}TaSe_2$ single crystal measured from CAC and DAC.

Overall *p*-*T* phase diagram including CAC and DAC data indicated in figure 4.3.18. T_C shows the maximum value of 7.35 K at 18.7 GPa. Higher than the optimal pressure, T_C starts to decreased but not be fully suppressed. This suggests that another quantum critical point might exist at higher pressure. In transport data, we cannot decide the existence of the quantum critical point. The low temperature and high pressure Raman experiment is possible tool to uncover the existence of the quantum critical point.

To explain the suppression of CDWs and the enhancement of T_C, we introduce two possible scenarios. The first scenario is that the intercalation of Pd can increase inter-layer coupling between $TaSe_2$ layers. If the inter-layer coupling increases, Fermi surface should be modified. Cylinder-like 2D Fermi surface is warped by *c*-axis interactions and it weakens Fermi surface nesting. This

weakening of the Fermi surface nesting vector results in the suppression of the CDW phase and the enhancement of superconductivity phase which competes with CDW. Another scenario is the decrease of *c*/*a* ratio. *c*/*a* ratio is the crucial factor to determine CDW and superconductivity temperatures in MX_2 [18]. In figure 4.3.19, decrease of *c*/*a* ratio suppresses CDW and enhances T_C. Decrease of *c*/*a* ratio can be obtained from hydrostatic or uniaxial pressure. Decrease of *c*-axis is larger than *a* or *b*-axis because van der Waals bonding between layers is weaker than intra-layer ionic bonding. Thus, decrease of *c*/*a* ratio can be realized by hydrostatic or uniaxial pressure.

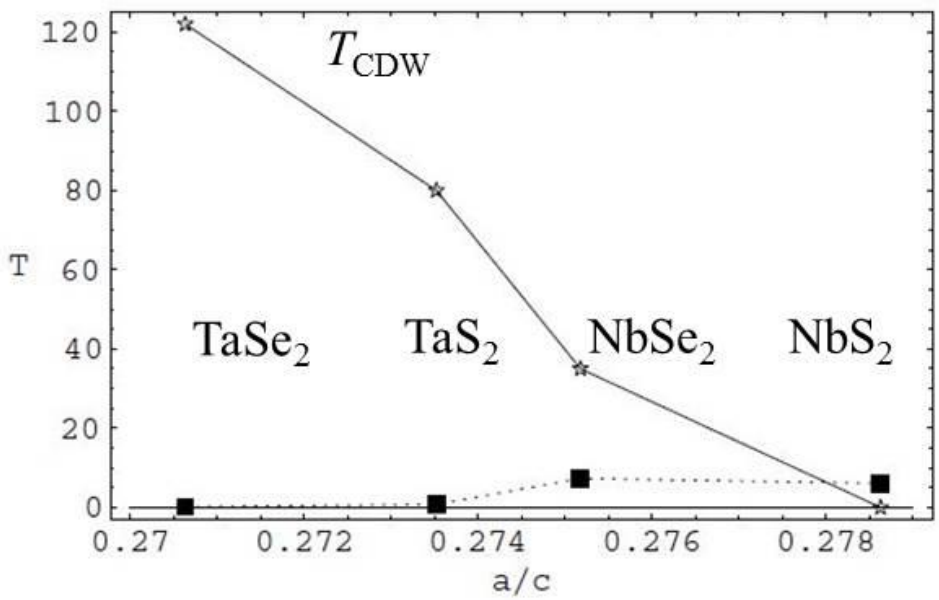

Figure 4.3.19. T_{CDW} and T_C are sensitive to *c*/*a* ratio of MX_2 materials. Large *c*/*a* ratio materials shows high T_{CDW} and low T_C or vice versa [18].

Interestingly, T_C enhancement was observed by adjusting of Pd intercalation concentration. The relationship between decrease of *c*/*a* ratio and T_C in the polycrystalline crystals was observed, even though both *a* and *c* axes

increase with Pd intercalation indicated in figure 4.3.20.

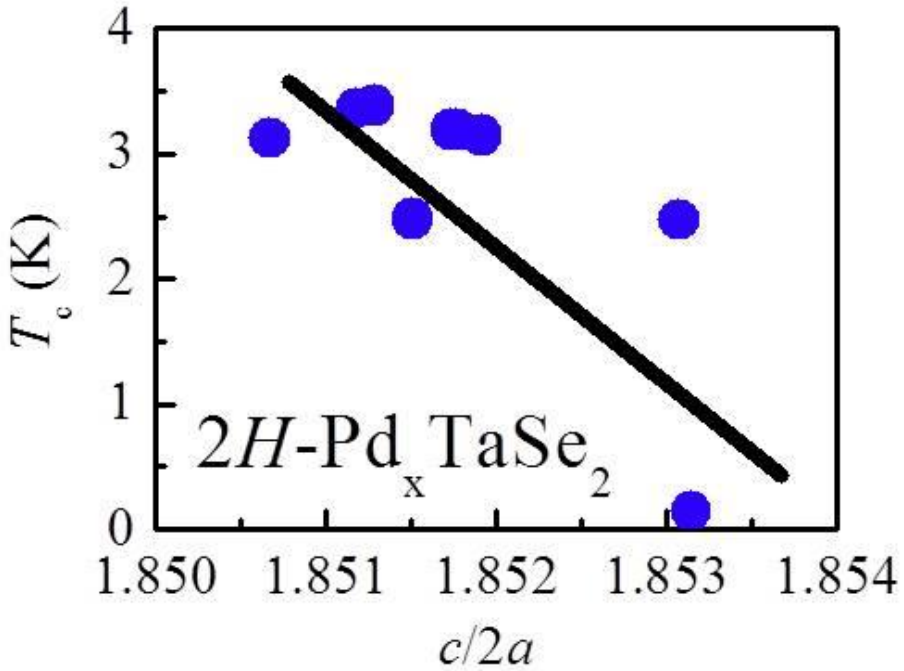

Figure 4.3.20. c/a ratio vs T_C in Pd_xTaSe_2 poly-crystalline samples. Small c/a ratio shows higher T_C.

Conclusion

We have investigated the pressure- and the chemical tuning-dependence of 2*H*-Pd_xTaSe_2 (x = 0.03 and x = 0.05) grown by $SeCl_4$ flux and 2*H*-Pd_xTaSe_2 (x = 0.02 and x = 0.06) grown by $PdCl_2$ flux. The suppression of the CDWs and the enhancement of T_C with linear slope were obtained in x = 0.02, 0.03, and 0.06 samples. For x = 0.05 crystal, we achieved a maximum T_C as high as 5.01 K without any saturation up to 8.0 GPa using cubic anvil cell. Furthermore, the maximum T_C was achieved to 5.72 K at 8.5 GPa in the x = 0.06 single crystal using cubic anvil cell and 7.35 K at 18.7 GPa using diamond anvil cell in the same

crystal. To reveal the existence of the quantum critical point, another high pressure measurement such as Raman spectroscopy is required.

4.4 $Ca_{0.9}La_{0.1}FeAs_2$

Discovery of the iron-based superconductor $LaFeAsO_{1-x}F_x$ with T_C of 26 K [19] play a very important role for searching new superconductors because it is believed that ferromagnetic ions suppress the superconductivity. Iron-based superconductors consists common Fe_2As_2 layers that are alternately stacked with various spacer layers.

Recently, new type of iron-based superconductor $Ca_{1-x}La_xFeAs_2$ was discovered [20]. The substitution of a small amount of La into Ca site stabilizes crystal structure, while pristine $CaFeAs_2$ (Ca112) is unstable. Ca112 consists of arsenic zigzag bond layers between Fe_2As_2 layers. Crystal structure of Ca112 is the first example of iron-based superconductor with the monoclinic space group $P2_1$ [20]. In $Ca_{0.9}La_{0.1}FeAs_2$ crystal, bulk superconductivity at 34 K was found in magnetization measurement and this value is quite large compare to other iron-based superconductors [20]. Moreover first-principle calculation indicates that the Fermi-surface has cylindrical-like shape, which is similar to those of 1111 compounds such as LaFeAsO and SrFeAsF [20].

4.5 High-pressure effect of $Ca_{0.9}La_{0.1}FeAs_2$

Newly found iron-based superconductor $Ca_{0.9}La_{0.1}FeAs_2$ shows quite large T_C compared to other iron-based superconductors. The maximum temperature of iron-based superconductor is near 55 K in $SmFeAs_{0.8}F_{0.2}$ crystal and it may be

related to iron-plane interlayer distance [21]. $Ca_{0.9}La_{0.1}FeAs_2$ has longer iron-plane interlayer distance than an optimal interlayer distance. Thus, if we can reduce interlayer distance by high-pressure, T_C might be enhanced higher than 50 K.

Experimental

Single crystal of $Ca_{0.9}La_{0.1}FeAs_2$ was grown by conventional self-flux method. We have grown $FeAs_2$ precursor and mix it with specific ratio of Ca : La : $FeAs_2$ = 0.9 : 0.1 : 1. Mixture was poured into Nb tube and heated to 1160˚C. after temperature is stabilized, we cooled Nb tube down to 950 K with a rate of 1˚C/h. Single phase and single crystal were confirmed by X-ray diffraction. Silver paste was use to contact between 25 μm Au wire and grown single crystals.

Hybrid piston cylinder cell and cubic anvil cell were used to apply high-pressure and conventional four probe technique was used to measure electrical property.

Results and discussion

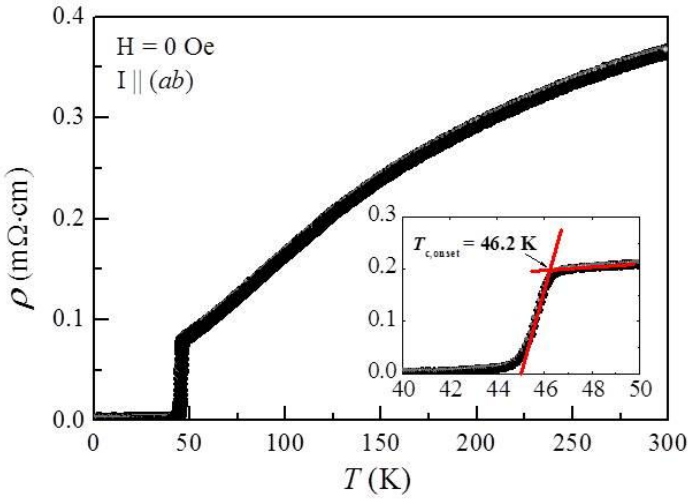

Figure 4.5.1. In-plane resistivity of $Ca_{0.9}La_{0.1}FeAs_2$ single crystal. $T_{C,onset}$ is determined to 46.2 K.

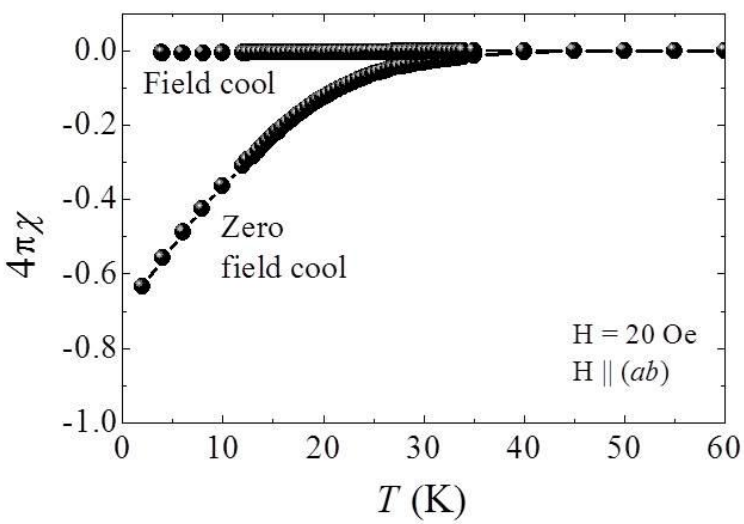

Figure 4.5.2. T_C obtained by magnetization is observed near 40 K and bulk superconductivity is also found.

The resistivity of $Ca_{0.9}La_{0.1}FeAs_2$ single crystal under 0.0 GPa pressure shows the $T_{C,onset}$ is near 46.2 K indicated in figure 4.5.1. The observed T_C is quite high compare to other iron-based superconductors. In magnetization data, bulk superconductivity was observed near 40 K indicated in figure 4.5.2.

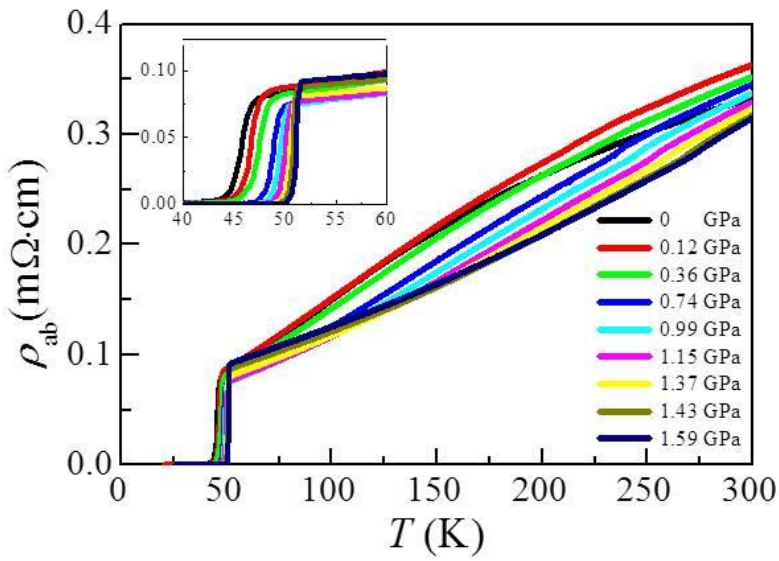

Figure 4.5.3. high pressure transport data up to 1.59 GPa measured by hybrid piston cylinder cell.

In figure 4.5.3, high-pressure transport properties of $Ca_{0.9}La_{0.1}FeAs_2$ single crystal using hybrid piston cylinder cell show monotonous enhancement of T_C and temperature exponent looks increasing with pressure.

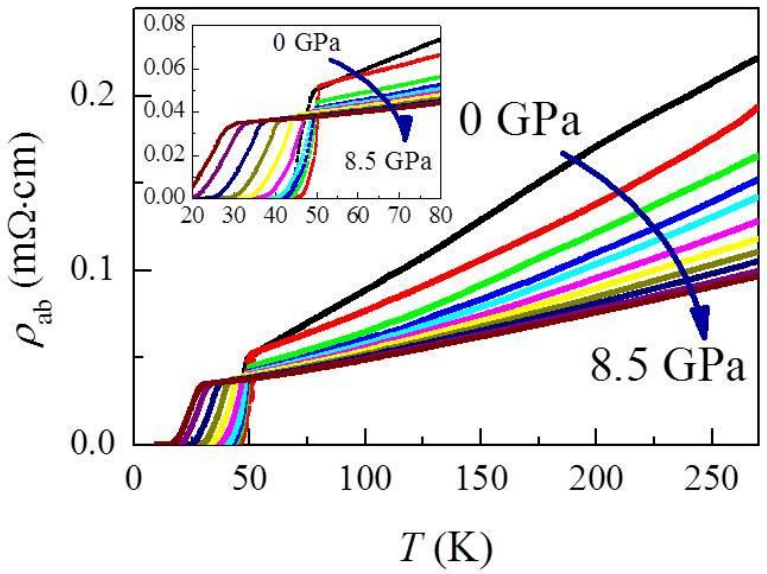

Figure 4.5.4. The resistivity of $Ca_{0.9}La_{0.1}FeAs_2$ single crystal up to 8.5 GPa using cubic anvil cell. Normal state resistivity shows decrease of temperature exponent.

High-pressure effect of $Ca_{0.9}La_{0.1}FeAs_2$ single crystal up to 8.5 GPa was measured using cubic anvil cell indicated in figure 4.5.4. The room temperature resistivity decreases with pressure and the maximum T_C of 51 K was observed near optimal pressure of 1.5 GPa. Higher than optimal pressure, T_C starts to decrease and shows superconducting dome.

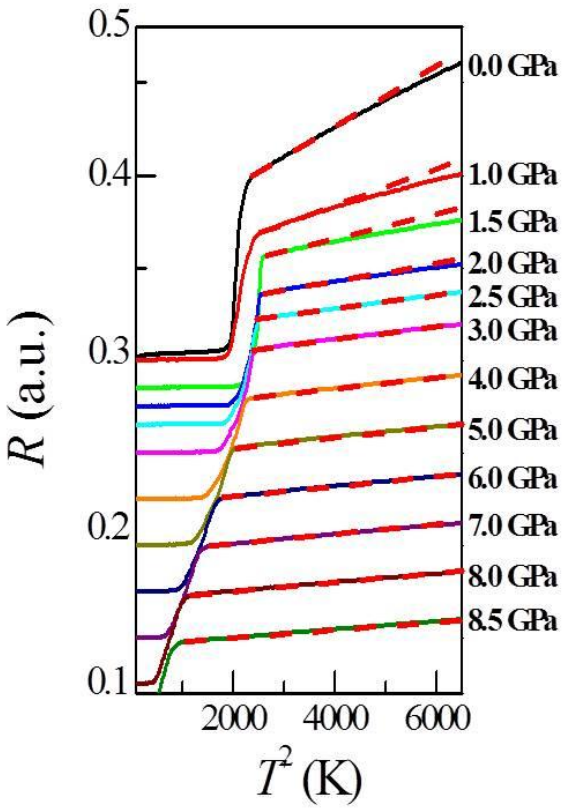

Figure 4.5.5. T^2 vs resistivity of $Ca_{0.9}La_{0.1}FeAs_2$ at various temperatures. T^2 behavior is distinctive at higher pressure.

In figure 4.5.5, T^2 behavior is more pronounced at higher pressure. It shows a possibility that the quantum critical point may exist at the optimal pressure. Magnetic field is necessary to reveal the effective mass or carrier types of $Ca_{0.9}La_{0.1}FeAs_2$. The effective mass usually diverges at the optimal pressure which shows the quantum critical point at the zero temperature.

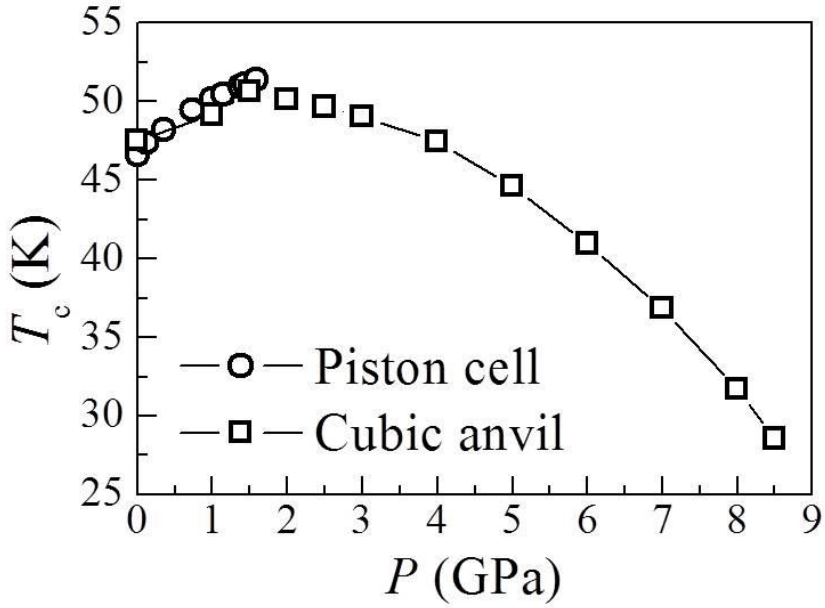

Figure 4.5.6. Superconducting phase diagram of $Ca_{0.9}La_{0.1}FeAs_2$ using hybrid piston cylinder cell and cubic anvil cell. The maximum T_C of 51 K was observed near 1.5 GPa.

Overall *p*-*T* phase diagram of $Ca_{0.9}La_{0.1}FeAs_2$ indicates in figure 4.5.6. Maximum T_C was observed 51.4 K at 1.59 GPa using hybrid piston cylinder cell and this value is quite large value among iron-based superconductors. Hall effect or Raman measurement is required to observed the existence of the QCP.

Conclusion

New discovered iron-based superconductor $Ca_{0.9}La_{0.1}FeAs_2$ single crystal shows high T_C among other iron-based superconductors. T_C is observed at 46.2 K at zero pressure and it is enhanced to 51.4 K at the optimal pressure. This T_C enhancement may be related to interlayer distance between iron-planes or angle of $FeAs_4$ tetrahedron. The evolution of temperature exponent gives us a possibility of the quantum critical point at the optimal pressure in this material.

4.6 $BaFe_2(As_{1-x}P_x)_2$ (x = 0.32, 0.51)

The most famous iron-based superconductors are Ba122 superconductor series. These materials have been studied more than 10 years since it is discovered. Pristine Ba122 crystal shows structure transition at 134.5 K and antiferromagnetic (AFM) order at 133.75 K [22]. In high pressure, structure transition temperature and AFM ordering temperature are suppressed and eventually superconductivity appeared [23]. The observed maximum T_C is 29 K at near 4 GPa [23].

In 2010, non-Fermi liquid behavior was observed in the P-doped Ba122 single crystals. By doping P into As site, the structure transition and spin density wave (SDW) suppressed and superconductivity is observed. At the optimal doping concentration ($x \sim 0.33$), T-linearity was observed up to quite high temperature. This T-linearity is indirect evidence of the non-Fermi liquid and the quantum critical point may exist in zero temperature at this doping concentration [24].

4.7 High-pressure effect of $BaFe_2(As_{1-x}P_x)_2$ (x = 0.32, 0.51)

In iron-based superconductor, the spin density wave or the structure transition is suppressed by pressure. P-doped Ba122 also shows the suppression of both structure transition and spin density wave, whereas T_C increases with pressure and P-doing concentration. Therefore, we measured pressure-dependence of resistivity to observe the evolutions of structure transition, spin density wave, and superconductivity.

Experimental

P-doped Ba122 single crystals were grown by Bridgman method to prevent evaporation of P. Stoichiometrically mixed powder of Ba, Fe, As, and P are put into Al_2O_3 crucible. After that, Al_2O_3 crucible is put inside of bigger size of W crucible and it is capsuled by arc welder. During $BaFe_2(As_{1-x}P_x)_2$ single crystal growth, W crucible was heated from room temperature to 1400 ºC with 50 ºC/h and temperature at the center of the Bridgman furnace was kept a constant temperature for 12 hours. After all uniformly mixed powder turns into liquid form, W crucible started to go down with rate of 1.5 mm/h. Total growth time is 100 h. Small part of solid single crystals starts to crystalize from the bottom of the crucible due to lower temperature compare to middle part of crucible. Using Bridgman growth method, we can grow big crystal with high homogeneity. All samples are cut into rectangular shape. Conventional four probe method was used and electrical contacts are made using silver paste. Electrical conductivity at 0 GPa was measured using PPMS. CAC was utilized to observe pressure effect up to 8.5 GPa.

Results and discussion

Grown single crystals of $BaFe_2(As_{1-x}P_x)_2$ show shinny surfaces and easily be exfoliated by conventional tapes. Typical sizes of the crystals are 2 mm × 2 mm. The resistivity at 0 GPa shows in figure 4.7.1. In $x \sim 0.32$ sample, the anomaly was observed near 60 K, while the resistivity of $x \sim 0.51$ sample is monotonically decreased as temperature decreases. Compared to previous reported data [24], T_Cs are matched to $x = 0.32$ and $x = 0.51$, even though nominal doping concentrations are 0.35 and 0.5, respectively.

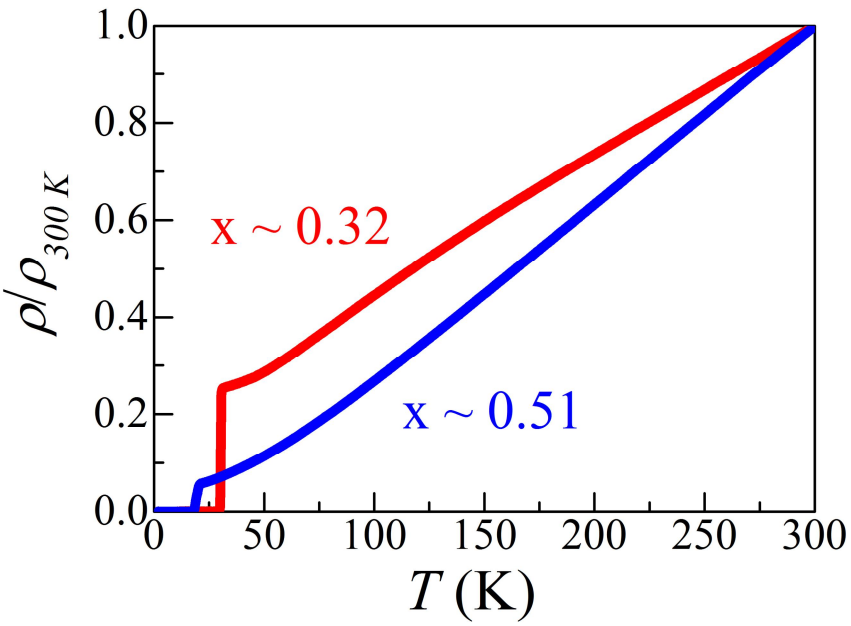

Figure 4.7.1. The resistivity of $BaFe_2(As_{1-x}P_x)_2$ ($x \sim 0.32$ and 0.51). $x \sim 0.32$ sample shows anomaly of the resistivity, while $x \sim 0.51$ sample does not show any anomaly of the resistivity. Both samples show superconductivity transitions.

By applying high pressure, we expected the continuous suppression of anomalies and the enhancement of the T_C. However, we observed unexpected anomaly at high pressure. The resistivity increased with pressure and kink of the resistivity was observed at 1.0 GPa indicated in figure 4.7.2. We defined the minimum point of the resistivity as T_0 which is related to structural transition and the resistivity kink point derived by derivative as T_{SDW} which is related to SDW transition temperature as described in previous reported data [24]. Higher pressure than 4.5 GPa, these T_0 and T_{SDW} started to decrease up to the maximum pressure we can reach.

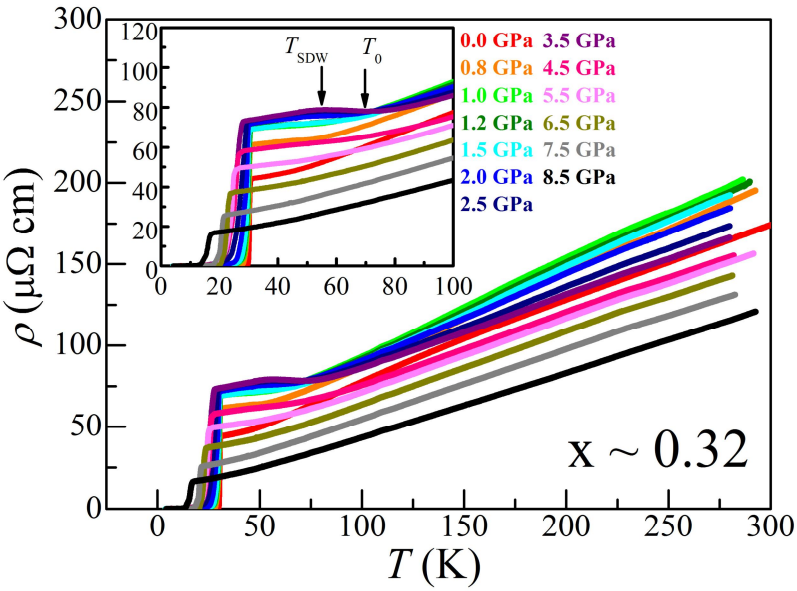

Figure 4.7.2. The resistivity of $BaFe_2(As_{1-x}P_x)_2$ ($x \sim 0.32$) single crystal under high pressure. Unexpected anomaly was observed near 1.0 GPa. That anomaly disappeared at higher pressure.

In figure 4.7.3, the resistivity versus pressure plot was indicated. The resistivity anomaly was observed near 4.0 GPa, which may be related to T_0 or T_{SDW}.

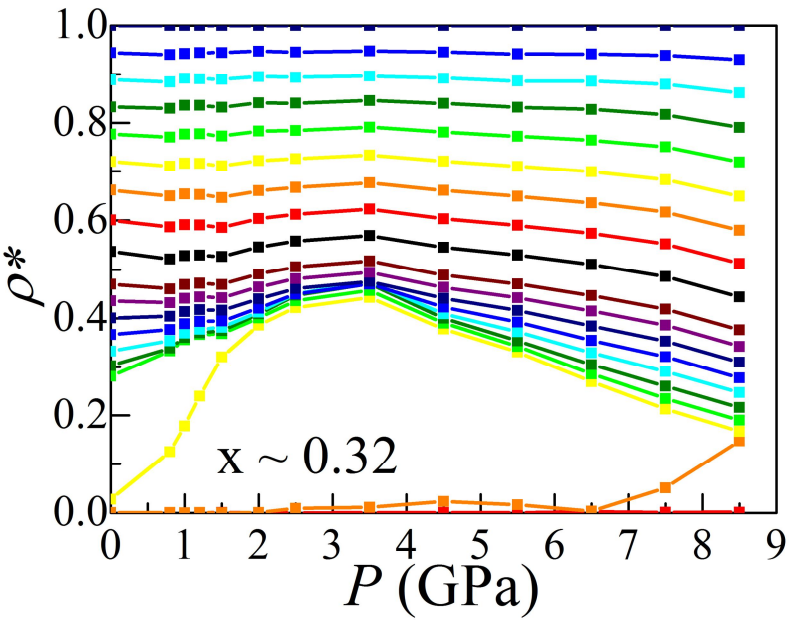

Figure 4.7.3. The resistivity vs pressure plot. Near 4.0 GPa, we can observed the resistivity hump and it may be related to T_0 or T_{SDW}.

In figure 4.7.4 to 4.7.6, ρ_0, A, and ε values of $BaFe_2(As_{1-x}P_x)_2$ ($x \sim 0.32$) are stated. The electrical transport data under pressure shows that the resistivity anomaly was observed in all pressure ranges and it has peak near 3.5 GPa. At this pressure, extracted ρ_0, A, and ε values fitted from $\rho(T) = \rho_0 + AT^{\varepsilon}$ shows anomalies. ρ_0 and ε show peak behavior near 4.0 GPa. However, sudden suppression was observed in A value near 2.5 GPa.

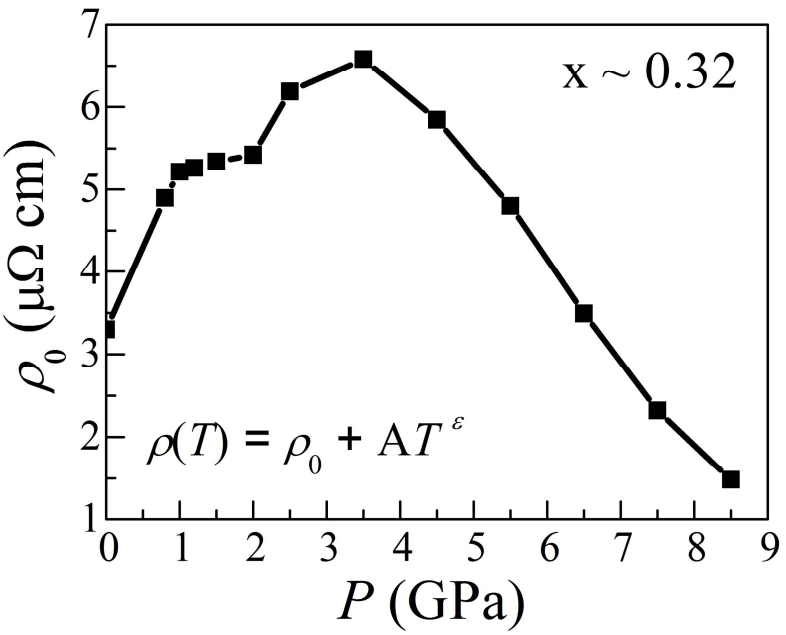

Figure 4.7.4. ρ_0 of $BaFe_2(As_{1-x}P_x)_2$ ($x \sim 0.32$). It shows the maximum value at 3.5 GPa.

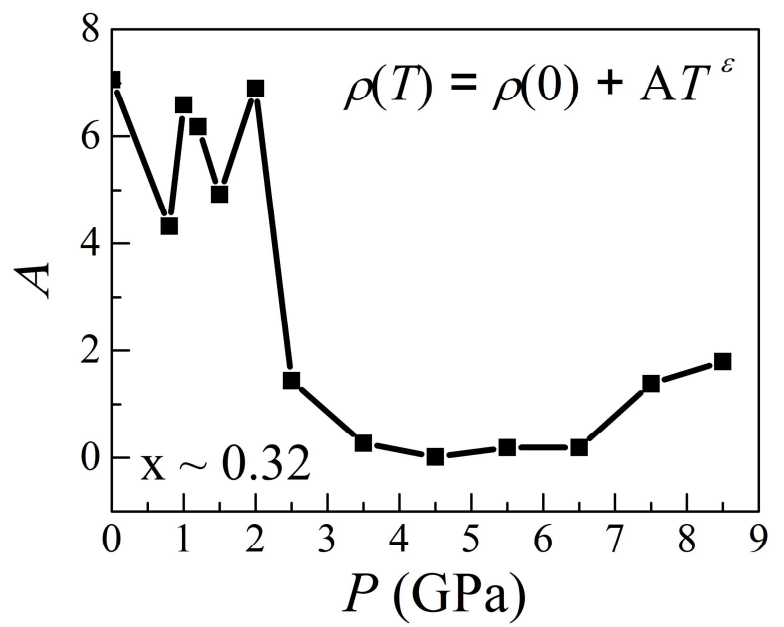

Figure 4.7.5. A value of $BaFe_2(As_{1-x}P_x)_2$ ($x \sim 0.32$). Constant A value was observed at lower pressure, while it suppressed rapidly higher than 2.5 GPa.

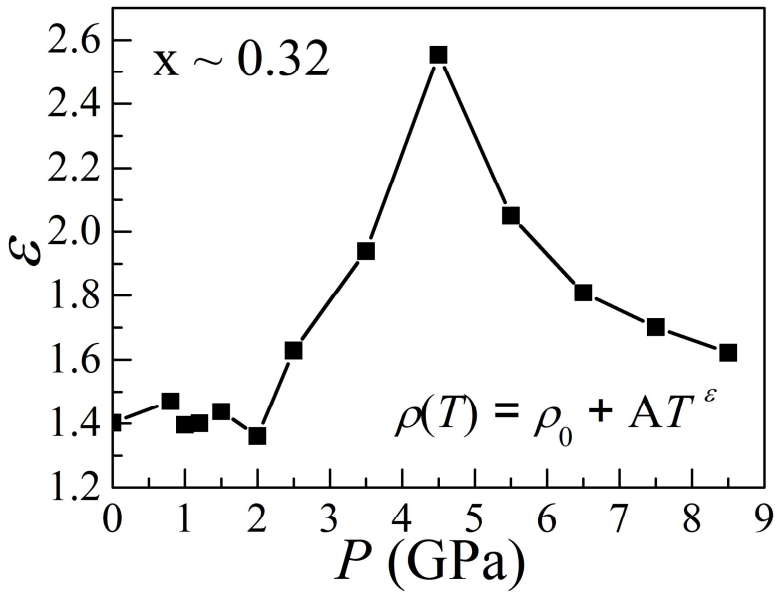

Figure 4.7.6. ε of $BaFe_2(As_{1-x}P_x)_2$ ($x \sim 0.32$). ε shows a peak at 4.5 GPa.

Overall phase diagram of $BaFe_2(As_{1-x}P_x)_2$ ($x \sim 0.32$) single crystal was indicated in figure 4.7.7. As mentioned previously, T_{zero} is suppressed when T_{SDW} and T_0 begin to increase. This implies that T_0 and T_{SDW} may compete with the superconductivity. However, further experiments are required to reveal the origin of the evolution of T_0 and T_{SDW} and the suppression of T_C.

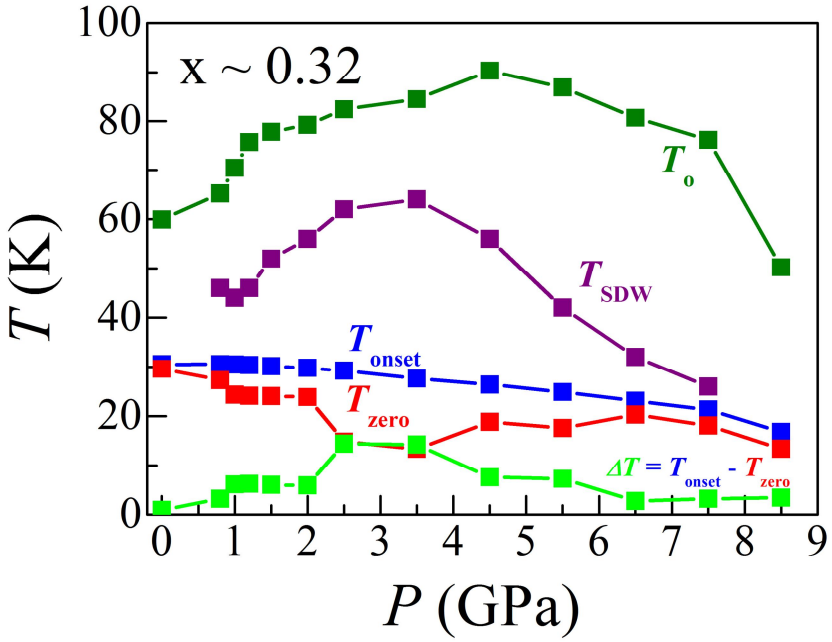

Figure 4.7.7. Phase diagram of $BaFe_2(As_{1-x}P_x)_2$ ($x \sim 0.32$) single crystal. At the maximum point of T_{SDW} and T_0, the suppression of T_{zero} was observed.

In $x \sim 0.51$ single crystal, no anomaly was observed at 0.0 GPa indicated in figure 4.7.8. However, the resistivity anomaly was observed near 4.5 GPa, which is higher pressure compared to $x \sim 0.32$ single crystal. The absolute value of the resistivity is also small compared to that of $x \sim 0.32$ sample.

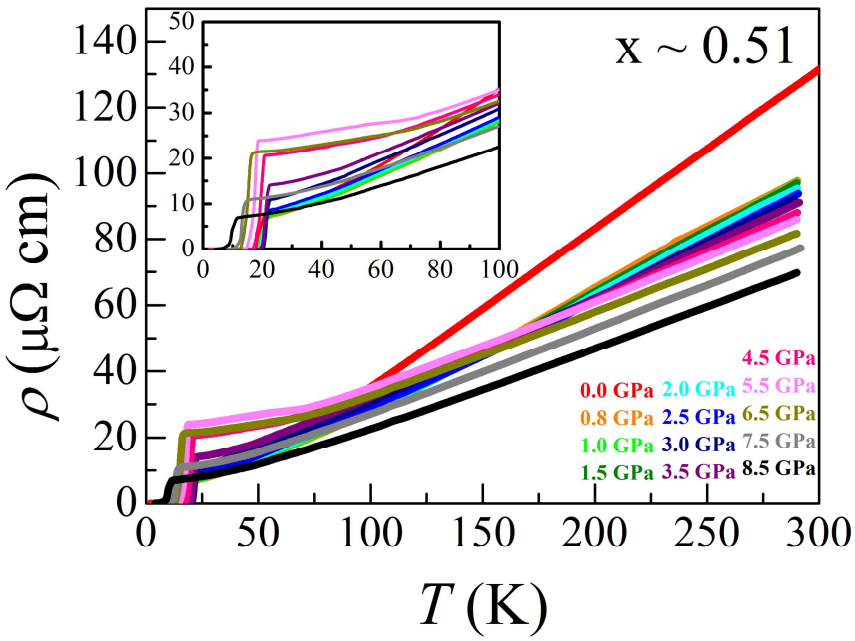

Figure 4.7.8. The resistivity of $BaFe_2(As_{1-x}P_x)_2$ ($x \sim 0.51$) single crystal under high pressure. Unexpected anomaly was observed near 5.0 GPa. The anomaly disappeared at higher pressure

In figure 4.7.9, the resistivity versus pressure plot of $BaFe_2(As_{1-x}P_x)_2$ ($x \sim 0.51$) was indicated. The resistivity anomaly was observed near 5.5 GPa, which may be related to T_0.

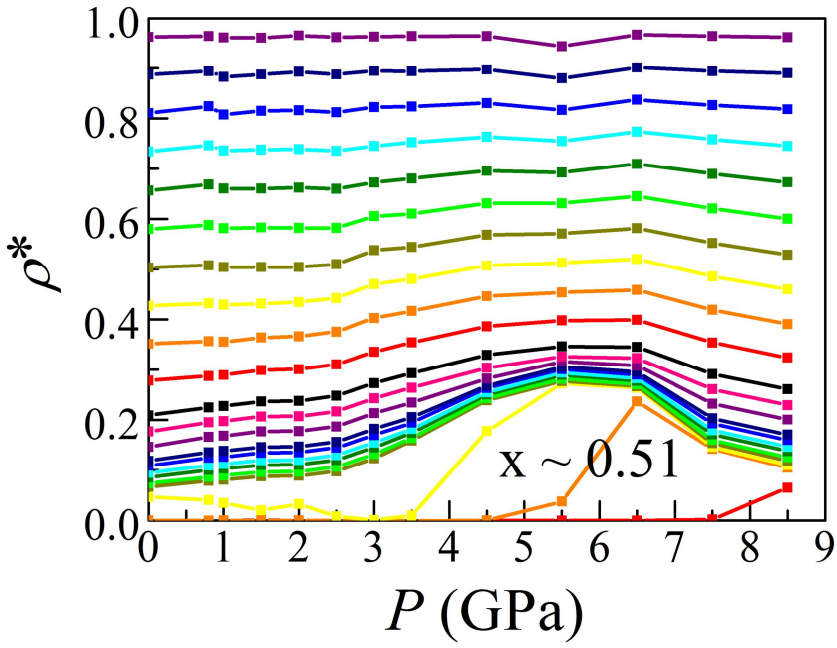

Figure 4.7.9. The resistivity versus pressure plot. Near 5.5 GPa, we can observed resistivity hump and it may be related to T_0.

In figure 4.7.10 to 4.7.12, ρ_0, A, and ε values of $BaFe_2(As_{1-x}P_x)_2$ ($x \sim 0.51$) are stated. The electrical transport data under pressure shows that the resistivity anomaly was observed in all pressure ranges and it has peak near 5.5 GPa. At this pressure, extracted ρ_0, A, and ε values show anomalies. ρ_0 and ε show peak behavior near 5.0 GPa. However, moderate decrease of A value was observed from 3.0 GPa.

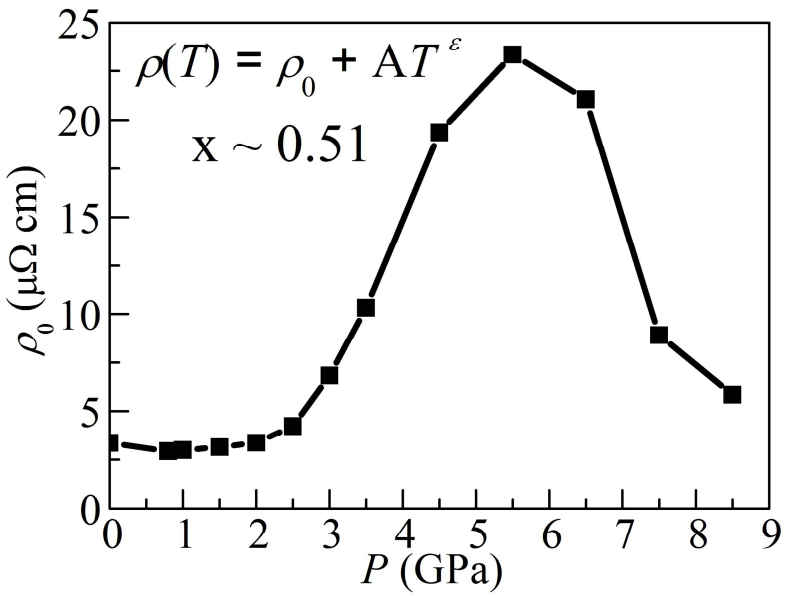

Figure 4.7.10. ρ_0 of $BaFe_2(As_{1-x}P_x)_2$ ($x \sim 0.51$). It shows the maximum value at 5.5 GPa.

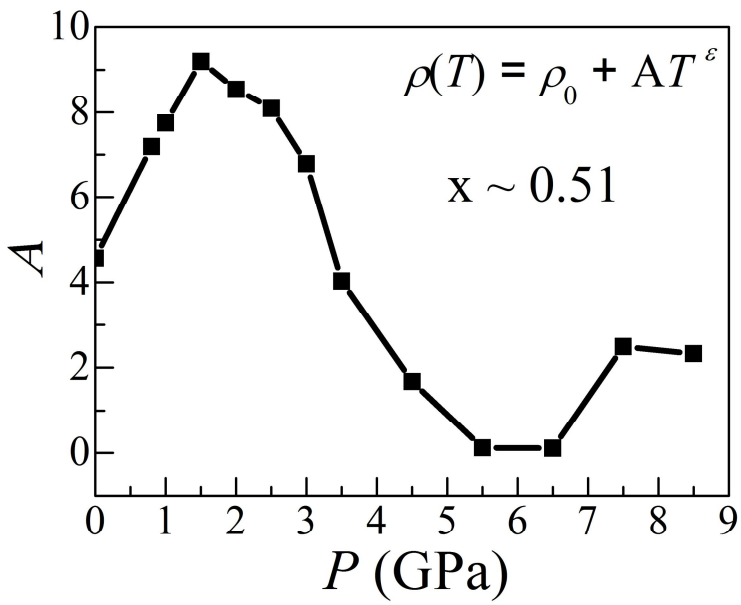

Figure 4.7.11. A value of $BaFe_2(As_{1-x}P_x)_2$ ($x \sim 0.51$). Small increase of A value was observed at lower pressure, while it suppressed rapidly higher than 3.0 GPa.

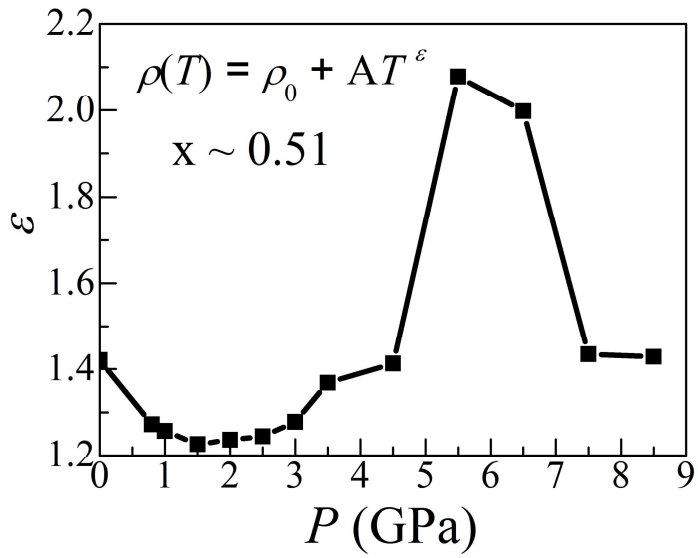

Figure 4.7.12. ε of $BaFe_2(As_{1-x}P_x)_2$ ($x \sim 0.51$). ε shows a peak at 5.5 GPa.

Phase diagram of $x \sim 0.51$ single crystal is quite different from that of $x \sim 0.32$ single crystal. However, the suppression of T_{zero} was observed when T_0 appeared. In this phase diagram, T_0 seems to compete to superconductivity.

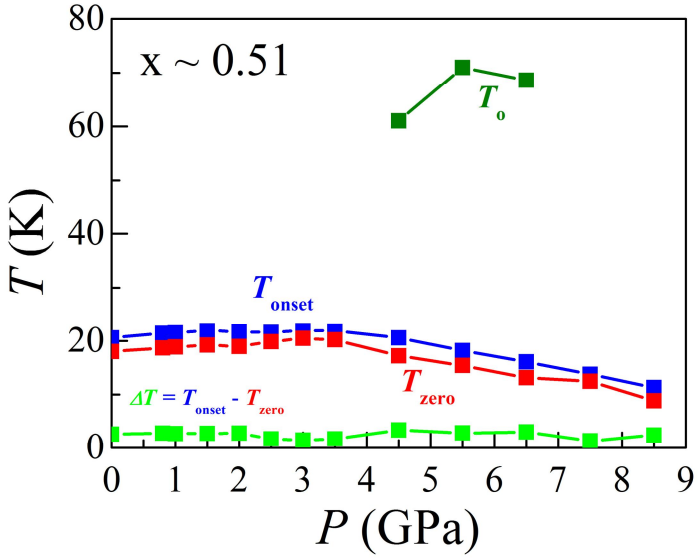

Figure 4.7.13. Phase diagram of $BaFe_2(As_{1-x}P_x)_2$ ($x \sim 0.51$) single crystal. At the maximum point of T_0, the small suppression of T_{zero} was observed.

Conclusion

We have reported high pressure effects of $BaFe_2(As_{1-x}P_x)_2$ ($x \sim 0.32$ and $x \sim 0.51$) single crystals. In both single crystals, unexpected resistivity anomalies were observed under high pressure. The resistivity anomalies seem to compete to superconductivity. To uncover the origin of these behaviors, we need further experiments such as high-pressure XRD or neutron scattering measurements.

Bibliography

[1] Wilson, J. A. *et al*. Advances in Physics **24** 117 (1975).

[2] Wilson, J. A. *et al*. Advances in Physics **18** 193 (1969).

[3] Rossnagel, K. J. Phys.: Condens. Matter **23** 213001 (2011).

[4] D. Bhoi. *et al*. Scientific Reports **6** 24068 (2016)

[5] Morosan, E. *et al*. Nat. Phys. **2** 544 (2006).

[6] Wagner, K. E. *et al.* **78** 104520 (2008).

[7] Morosan, E. *et al*. Phys. Rev. B **81** 094524 (2010).

[8] Fang, L. *et al.* Phys. Rev. B **72** 014534 (2005).

[9] Gamble, F. R. *et al*. Science **168** 568 (1970).

[10] Gamble, F. R. *et al*. Science **174** 493 (1971).

[11] Kusmartseva, A. Phys. Rev.Lett. **103** 236401 (2009).

[12] Sipos, B. *et al.* Nat. materials **7** 960 (2008).

[13] Yu, Y. *et al.* Nat. Nanotech. **10** 270 (2015).

[14] Moncton, D. E. *et al*. Phys. Rev. Lett. **34** 734 (1975).

[15] Moncton, D. E. *et al*. Phys. Rev. B **16** 801 (1977).

[16] Fleming, R. M. *et al*. Phys. Rev. Lett. **45** 576 (1980)

[17] K. Yokogawa. *et al*. Jpn. J. Appl. Phys. **46** 3636 (2007)

[18] A. H. Castro Neto. Phys. Rev. Lett. **86** 4382 (2001)

[19] Y. Kamihara *et al*. J. Am. Chem. Soc. **130** 3296 (2008)

[20] N. Katayama *et al*. JPSJ. **82** 123702 (2013)

[21] H. Ogino *et. al*. Appl. Phys. Lett. **97** 072506 (2010)

[22] M. G. Kim *et al*. Phys Rev B **83** 134522 (2011)

[23] Patricia L Alireza *et al*. J. Phys.: Condens. Matter **21** 012208 (2009)

[24] S. Kasahara *et al*. Phys. Rev. B **81** 184519 (2010)

[25] Dong Hyun Jang *et al*. summited. (2017)

5. Quasi one-dimensional materials

5.1 Introduction

Previous researches are focused on electrical properties of the quasi two-dimensional superconductor materials. When the dimensionality of materials is decreased down to 1D, 1D character is emerged in transport properties due to its strong directionality of conducting chains. Quasi-1D materials accompany to density wave caused by Peierls instability and sensitive to disorder of the crystals. In this section, we will report high-pressure transport properties of quasi-1D materials focused on organic conductor [(*S,S*)-DM-MeDH-TTP]$_2$AsF$_6$ and chalcogenide superconductor $Nb_2Pd_xSe_5$.

5.2 [(*S,S*)-DM-MeDH-TTP]$_2$AsF$_6$ organic conductor

The correlations between electrons in materials change their ground states of materials from the insulating state with the strong on-site Coulomb repulsion *U* to the metallic state with the large bandwidth *W*. In the strongly correlated system, the single parameter *U*/*W* ratio controls properties of ground states by changing physical pressure or chemical substitutions in turn metal-insulator transition (MIT) can be observed [5, 6]. In this framework, two kinds of critical phenomena can be expected; the classical criticality in the vicinity of the critical end point and the quantum criticality at the finite temperature. The critical exponents set determined their universality classes. The universality classes are determined by global parameters such as dimensionality or symmetry, not by microscopic interactions or ground states.

In 2003, critical exponents β, γ, δ were found in the 3D Mott MIT system [5]. Each critical exponent can be calculated by $\sigma - \sigma_c \sim (T_c - T)^{\beta}$, $(d\sigma_{met}/dP) \sim (T - T_c)^{-\gamma}$, and $\sigma_{457K} - \sigma_c \sim (P_c - P)^{1/\delta}$ because the order parameter of MIT is the electrical conductivity. These critical exponents must satisfy critical relation $\gamma = \beta(\delta - 1)$ which is called Widom's identity. In 3D system of Cr-doped V_2O_3 crystal, Mott MIT was observed under pressure induced by helium gas. When insulator state turns into metal, the electrical conductivity defined by $\sigma(T,P) = 1/\rho(T,P)$ increases discontinuously and shows the finite electrical conductivity. Near the critical end point, critical exponents were measured to be $\beta = 0.34$, $\gamma = 1$, and $\delta = 5$, whereas $\beta = 0.5$, $\gamma = 1$, and $\delta = 3$ were measured far away from the critical end point. These critical exponents satisfy the critical relation near or far away from the critical end point. These critical exponents set belong to 3D Ising and mean-field universality classes, respectively.

In quasi-2D organic conductor κ-(BEDT-TTF)$_2$Cu[N(CN)$_2$]Cl, critical exponents should be different from that of 3D system, since the universality class is determined by its crystal dimensionality [6]. Mott MIT is considered as the Ising universality class. In Mott MIT system, metal state can be considered as a spin up state and insulating state can be considered as a spin down state. Thus, Mott MIT system can be explained by Ising model. However, obtained critical exponents of the quasi-2D organic conductor show unconventional values of $\beta = 1$, $\gamma = 1$, and $\delta = 2$ [6]. Theoretically calculated critical exponents of 2D Ising universality class are $\beta = 0.125$, $\gamma = 1.75$, and $\delta = 15$. The origin of this discrepancy between theoretically calculated 2D Ising critical exponents and experimentally discovered 2D organic critical exponents is unclear. Theory research group proposed that these unconventional critical exponents can be related to marginal quantum criticality [9].

Previously, critical exponents of 3D and 2D Mott MIT have been revealed near the critical end point. If we can reduce the dimension of the crystal, what happen to their critical exponents? This question drives us to study the critical exponents of quasi-1D system. We start from the quasi-1D organic conductor of $[(S,S)\text{-DM-MeDH-TTP}]_2AsF_6$ which is grown by Prof. Nishikawa's group in Ibaraki university. $[(S,S)\text{-DM-MeDH-TTP}]_2AsF_6$ single crystals were grown by the conventional electrochemical method. Typical size of the crystals are 1 mm × 1 mm. Theoretical calculation by tight binding calculation method from Prof. Nishikawa's group shows that the grown organic single crystal has quasi-1D character and 3/4 filled Fermi surface. The same group suggests that grown crystals are dimerized and eventually charge ordered state forms. This crystal shows insulating behaviors in all temperature range from 2 K to 300 K under ambient pressure. Thus, if we can find the critical end point near the metal-insulator crossover, we can define critical exponents β, γ, and δ in quasi-1D system.

In Mott MIT system, Coulomb repulsion U and bandwidth W are important parameters to characterize metal and insulating state. In the MIT configuration, the competition between U and W can be expected by tuning the clean physical parameters such as hydrostatic pressure and possibly the quantum criticality can be observed at finite temperature due to large energy scale competitions.

In the conventional MIT system, the coexistence region hinders the observation of the zero-temperature quantum critical point, since its first-order nature eliminated at the critical end point T_c screens the quantum critical point [5, 6, 12, 13]. Recently, the dynamic mean field theory (DMFT) calculation suggested that the finite temperature quantum criticality can be realized in the intermediate

temperature range of $T_c < T << U, W$ due to large competing energy scale [7]. Generally, energy orders of U and W are several thousand Kelvin or even higher. [23]. Experiments studied on three different kinds of quasi-2D organic conductors κ-$(ET)_2Cu_2(CN)_3$, κ-$(ET)_2Cu[N(CN)_2]Cl$ and $EtMe_3Sb[Pd(dmit)_2]_2$ have also revealed the finite temperature quantum criticality can exist almost two times higher than T_c [8]. In the quasi-2D organic conductors, the quantum critical scaling was observed with the critical exponent of $z\nu = 0.6 \pm 0.1$, where z is the dynamical critical exponent, and ν is the correlation length critical exponent [8]. This value shows quite similar value of $z\nu \sim 0.6$ calculated from DMFT calculation [7]. On the other hand, different critical exponent $z\nu = 1.6$ was reported in a two-dimensional Si-MOSFET [10, 11] and this similar critical exponent of $z\nu = 2$ ($z = 4$, $\nu = 1/2$) was proposed in the theoretical study for the marginal quantum Mott transition [14]. Moreover, different critical exponents were confirmed experimentally in the 2D ultracold Bose gases in optical lattices with $z\nu = 1$ ($z = 2$, $\nu = 1/2$) [17] and corresponds to the theoretical prediction [18]. The origin of these discrepancies between experiments in two-dimensional systems is still unclear and further researches on the quantum criticality are required.

In the one-dimensional strongly correlated system, the Tomonaga-Luttinger liquid (TLL) can be described regardless of the quantum statistics of the constituent particles and it leads to the free-fermion universality class of the quantum criticality near a phase transition [15]. Generally, the quantum fluctuation is enhanced when the dimensionality of the material is reduced and it generates the phase transition from quantum disordered to the TLL state with competition of low energy scales in the 1D material [16]. Recently, the quantum criticality in the 1D Bose gas was reported with critical exponent of $z\nu = 1$ ($z = 2$, $\nu = 1/2$ for the

quantum critical phase and z = 1, ν = 1 for the TLL phase) [15]. In classical gas, the quantum critical region and the TLL phase were separated by $T^* \sim | \mu - \mu_c |^{z\nu}$ with zν = 1 in the 1D Bose gas [15]. The relationship between the global parameters of materials and universality classes are unknown, since only a few researches have been reported to the quantum criticality in low-dimensional systems. Here, we also report the quantum criticality in the quasi-1D organic conductor using cubic anvil cell.

5.3 High-pressure effect of [(*S*,*S*)-DM-MeDH-TTP]$_2$AsF$_6$ organic conductor

First, we report the classical critical exponents β, γ, and δ and the finite temperature quantum criticality in the quasi-1D organic conductor using scaling hypothesis above the quantum phase transition temperature to find the relationship between one-dimensional Bose gas and strongly correlated electron system. Furthermore, we compare the reported critical exponents of the quasi-2D organic conductors to that of our quasi-1D organic conductor results.

To observe various classical critical exponents of β, γ, δ, and dynamic exponent zν, physical tuning parameters such as magnetic field or hydrostatic pressure is required. Critical exponents of Ising spin system can be obtained by applying magnetic field. However, in the MIT system, electrical properties are sensitive to pressure. Here, pressure effect of the quasi-1D organic conductor will be reported to find critical exponents and the quantum criticality.

Experimental

Single crystals of [(*S,S*)-DM-MeDH-TTP]$_2$AsF$_6$ were grown by conventional electrochemical oxidation method reported elsewhere [24]. The typical sizes of single crystals are ~1 mm × ~1 mm. The electrical conductivity $\sigma(P, T)$ was measured using the standard d.c. four-probe method at the fixed pressure. We made electrical contacts to crystal surfaces with 10 μm Au wires and carbon paste as electrodes. Organic conductors are very fragile so we annealed Au wires using electric current to make it soften. In Figure 5.3.1, the organic conductor was loaded in the CAC. Direction of the electrical current is *b*-axis which is the current chain direction of the organic conductor. Pressure transmitting medium Daphne 7373 oil was used to apply hydrostatic pressure. We measured the $\sigma(P, T)$ at the fixed pressure to observed the MIT and replot the $\sigma(P, T)$ vs pressure at selected temperatures. In previous reports related to the quantum and classical criticalities in the Mott transition systems, gas helium press was used and only small experimental window can be achieved by gas helium press with the maximum pressures of 0.35 GPa and the minimum temperature of 35 K [5,6] due to solidification of He gas. To overcome this limitation, we used CAC to measure pressure-dependence of the $\sigma(P, T)$ as a function of temperature in the constant and hydrostatic pressure. To research the critical behavior of the quasi-1D organic conductor, high hydrostaticity of the pressure is required. The CAC covers the pressure range up to 10 GPa and temperature range down to 2 K. [(*S,S*)-DM-MeDH-TTP]$_2$AsF$_6$ single crystal is expected charge ordered system based on theoretical calculation, not the Mott insulator [24]. Therefore, we consider this material in the general MIT framework, not the Mott MIT.

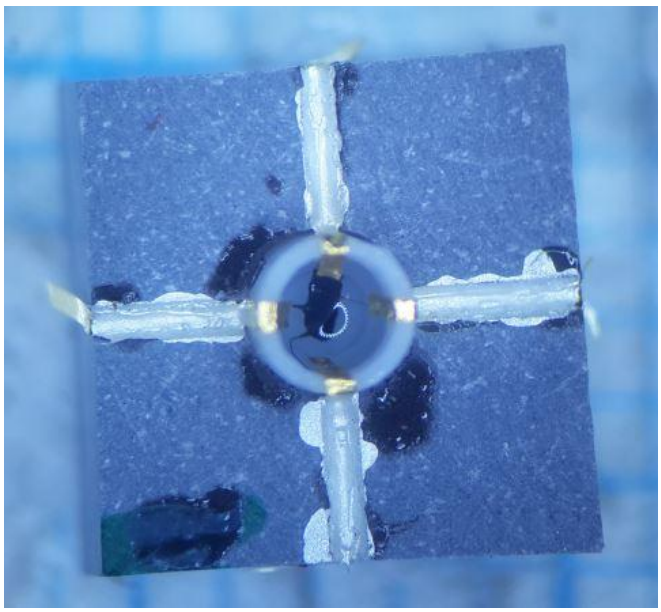

Figure 5.3.1. Organic conductor load in the Teflon cup and pyrophilite gasket.

Results and discussion

The resistivities versus temperature at various pressures show insulating behavior at 0 GPa indicated in figure 5.3.2. As pressure increase, resistivities were decreased and upturn behaviors were weakened, eventually metallic state was appeared. In figure 5.3.3, replotted the electrical conductivity versus pressure data were indicated at selected temperatures. At fixed temperature, metal-insulator crossover behavior was observed. However, we could not find first-order MIT, which means that there is the strong fluctuation in crystals. Zero electrical conductivity insulator state changes to the finite conductivity metallic state.

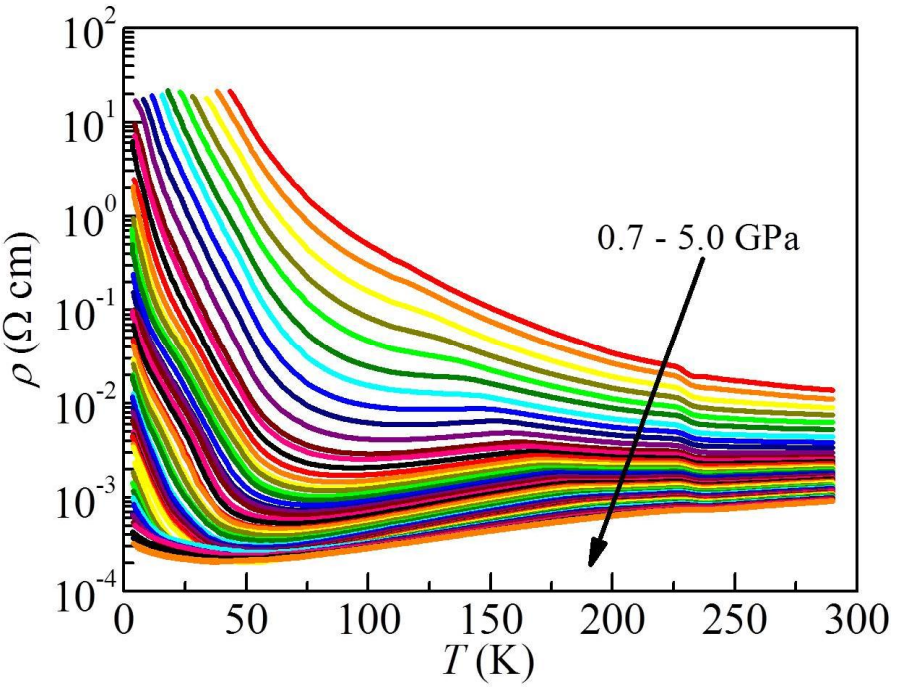

Figure 5.3.2. The resistivities versus temperature plot at selected pressure. During cooling down temperature, pressure is kept constant.

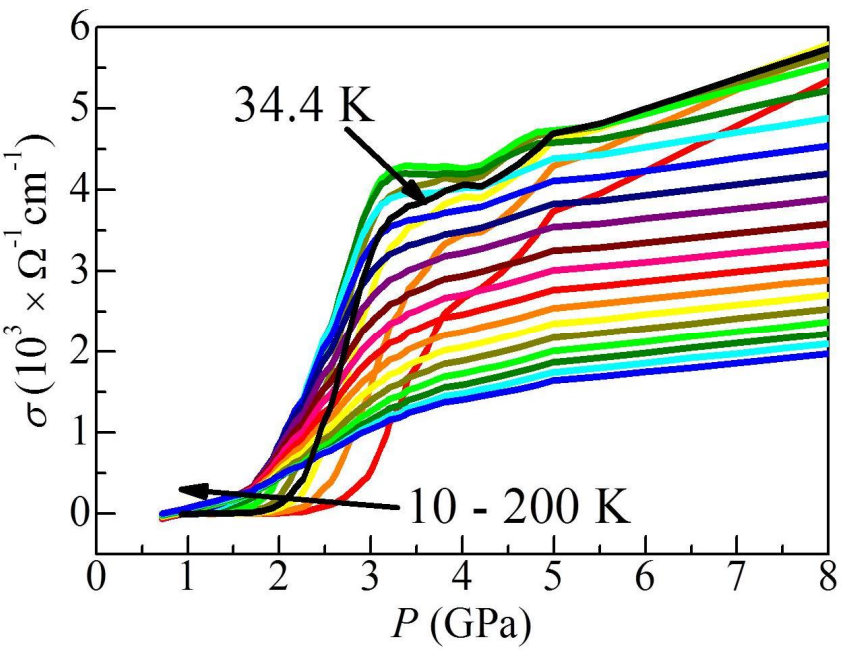

Figure 5.3.3. Conductivity (σ) vs P plot at selected temperature obtained from figure 4.3.2.

No existence of the first-order transition indicates that the critical end point cannot be found in this system. At the critical end point, the value of the conjugate field derivative of the order parameter diverges. In this experiment, this value is defined by the pressure derivative of the electrical conductivity. In the first-order transition, value of $d\sigma/dP$ diverges at the point where the first-order transition disappears and crossover from insulator to metal emerges. In figure 5.3.4, $d\sigma/dP$ at various temperatures is indicated. In the organic conductor, however, the divergence of $d\sigma/dP$ was not observed. Thus, we defined the maximum $d\sigma/dP$ point as T^* rather than T_C, since we could not find the any first-order MIT signature.

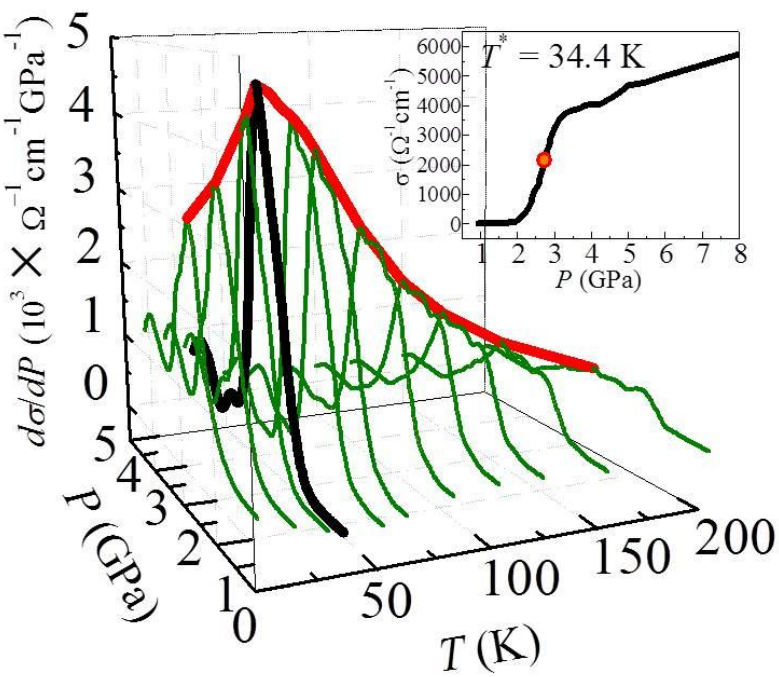

Figure 5.3.4. $d\sigma/dP$ at selected temperatures. The divergence of $d\sigma/dP$ was not found at all temperature. $d\sigma/dP$ shows the maximum value at 34.4 K. The crossover pressure was defined at the inflection point of σ vs P as indicated in inset.

In the MIT, we can define the order parameter and its crossover behavior. According to the theoretical calculation of strongly correlated electron systems, the order parameter of MIT is a scalar nature and it can be measured by the electrical conductivity [1 - 4]. Above the T_C, the first-order transition of the electrical conductivity as a function of pressure smeared out and crossover emerges [5,6]. Inset of figure 5.3.4 shows the $\sigma(P,T)$ and its inflection point corresponds to crossover of the order parameter at 34.4 K which has the maximum value of $d\sigma/dP$. We define this point as a crossover pressure $P_C \sim 2.74$ GPa and zero temperature electrical conductivity begin to increase near P_C as indicated in figure 5.3.5. The conductivity below 20 K is approximately proportional to T and zero-temperature conductivity $\sigma_{0K}(P,T)$ is obtained by the linear extrapolation. $\sigma_{0K}(P,T)$ shows a continuous onset near 2.8 GPa and increase of $\sigma_{0K}(P,T)$ is quite proportional to the applied pressure above 2.8 GPa. Thus, pressure induces the continuous MIT around 2.8 GPa and the similar behaviors were observed in the geometrical frustrated system in $Gd_2Mo_2O_7$ and $Eu_2Ir_2O_7$ [20, 21].

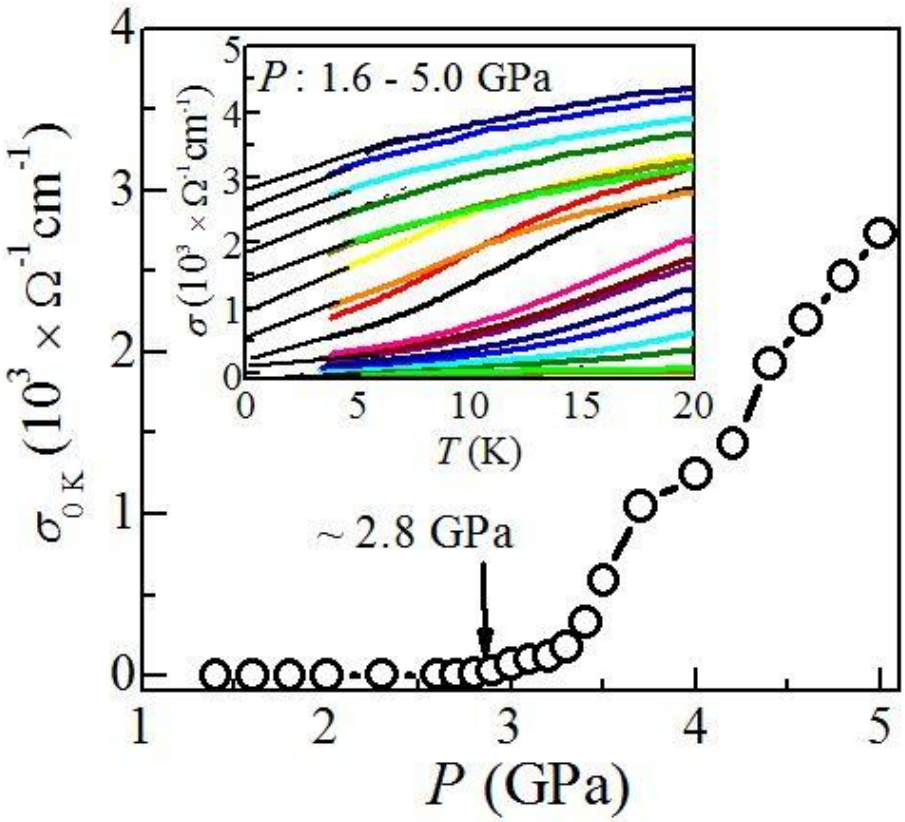

Figure 5.3.5. Zero temperature conductivity at various pressures. Zero temperature conductivity starts to increase near 2.8 GPa which indicate that the metal insulator crossover can be appeared at this pressure.

Absence of the first-order MIT of our quasi-1D organic conductor is probably due to strong low-dimensionality frustration or disorder such as an impurity. Furthermore, the resistivity upturn (figure 5.3.2.) in the low temperature regime can also be related to the low-dimensional frustration similar to geometrical frustrations reported in ref [20, 21] or it can be due to impurities of crystal.

Temperature versus pressure phase diagram is indicated in figure 5.3.6. It shows interesting feature that the phase diagrams obtained form ρ vs T and σ vs P are different. Red line obtained from σ vs P divides zero σ insulating state and

finite σ metallic state. We defined $P_C \sim 2.74$ GPa which separates insulator and metal. Thus, left side of red line is considered as an insulator, while right side of red line is the metallic region. Crossover line is straight higher than T^*, while red line tilts to higher pressure side in lower temperature. The origin of tilts of red line is unclear. When it comes to blue line phase diagram obtained from ρ vs T, it shows the complex phase diagram. In the lower pressure, the resistivity shows the insulating behavior. However, pressure higher than 1.4 GPa, metallic region appeared in the medium temperature range. However, this metallic region was difficult to be explained because phase diagram obtained from σ vs P indicates that the left part is the insulator. These discrepancies between two differently obtained phase diagrams are interesting in research point of view.

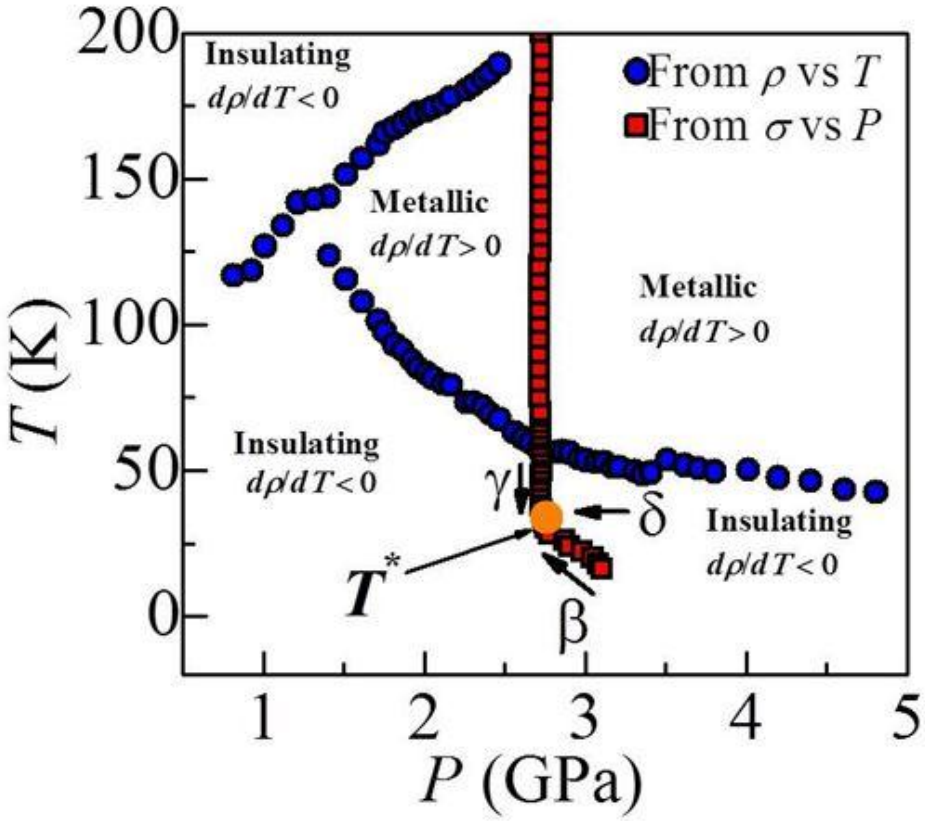

Figure 5.3.6. Temperature pressure phase diagram of $[(S,S)\text{-DM-MeDH-TTP}]_2AsF_6$ quasi-1D organic conductors. Metallic regime and insulating regime are defined by $d\rho/dT$. Critical exponents β, δ, and γ were obtained along the arrow directions.

In above phase diagram, we can define T^* as a maximum point of $d\sigma/dP$, since we could not find the critical end point T_C. Thus, we cannot derive β, δ, and γ from T_C directly. Although we cannot define T_C, we can try to obtain critical exponents δ, β and γ near T^* following arrows indicating in figure 4.3.6.

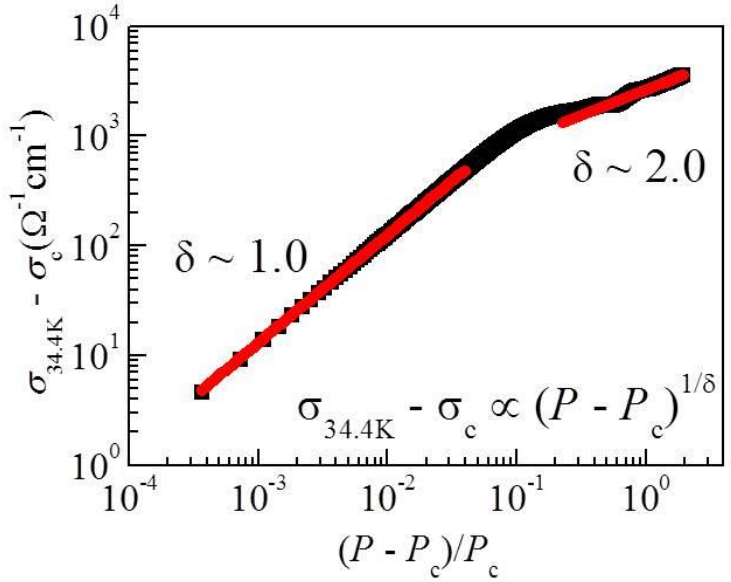

Figure 5.3.7. The critical exponent δ of $[(S,S)\text{-DM-MeDH-TTP}]_2AsF_6$ quasi-1D organic conductor.

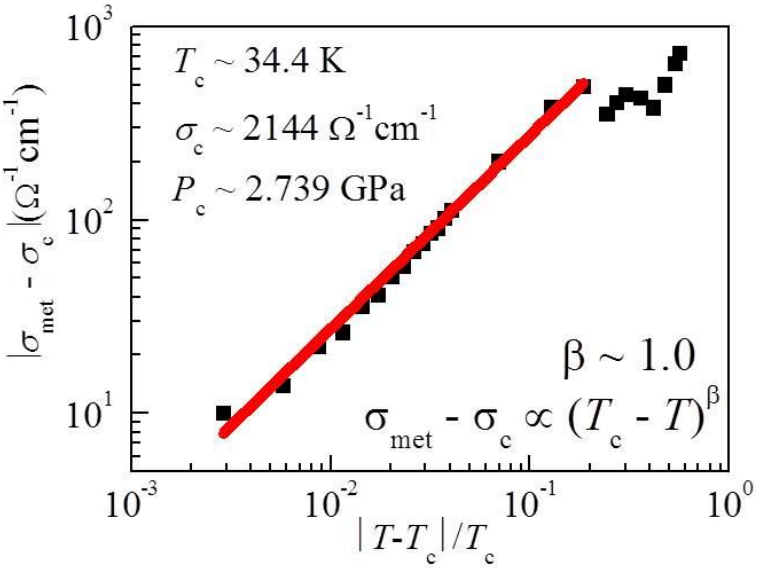

Figure 5.3.8. The critical exponent β of $[(S,S)\text{-DM-MeDH-TTP}]_2AsF_6$ quasi-1D organic conductor.

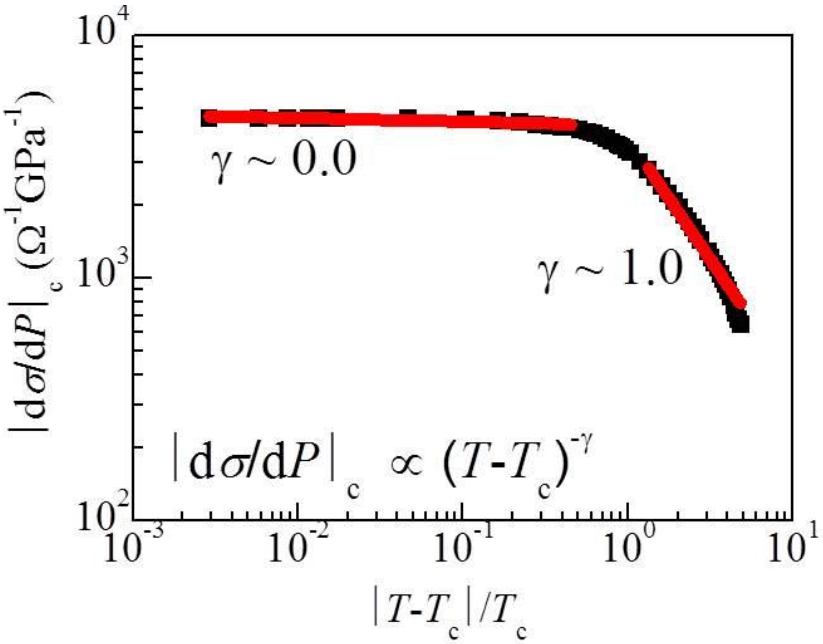

Figure 5.3.9. The critical exponent γ of [(*S,S*)-DM-MeDH-TTP]$_2$AsF$_6$ quasi-1D organic conductor.

Three critical exponents show that $\delta = 1$, $\beta = 1$ and $\gamma = 0$ close to T^* as indicated from figure 5.3.7 to figure 5.3.9. Since there are no reported references of critical exponents of 1D Ising model, we cannot determine that whether these values are unconventional or not. Far away T^*, obtained critical exponents $\delta = 2$, $\beta = 1$ and $\gamma = 1$ are the same as critical exponents of the quasi-2D organic conductor. It can be assumed that the universality class crossover from the quasi-1D to the quasi-2D appeared far away from T^* in the quasi-1D organic conductor. Although these critical exponents look unconventional, both critical exponents satisfy Widom's identity. However, this crossover is not the real crossover from the quasi-2D to the quasi-1D due to no existence of the critical end point. Thus, further experiments are required to uncover these discrepancies.

In the quantum critical point of view, the quantum criticality can be

expected in the MIT. This approach is quite different from the classical critical exponents indicated previously. In the crossover region, the quantum criticality is expected due to the fluctuation of energy scales [7]. Moreover, more than one crossover lines can be defined as proposed by the dynamic mean-field theory [19]. In previous reports on the quantum criticality in the quasi-2D organic conductors, the inflection points of log[$\rho(P, T)$] were adopted to define crossover or instability pressure. Although we use the inflection point of the electrical conductivity as an crossover point in this report, we will compare quantum critical exponents calculated from the inflection point of log[$\rho(P, T)$] to the inflection point of $\sigma(P, T)$.

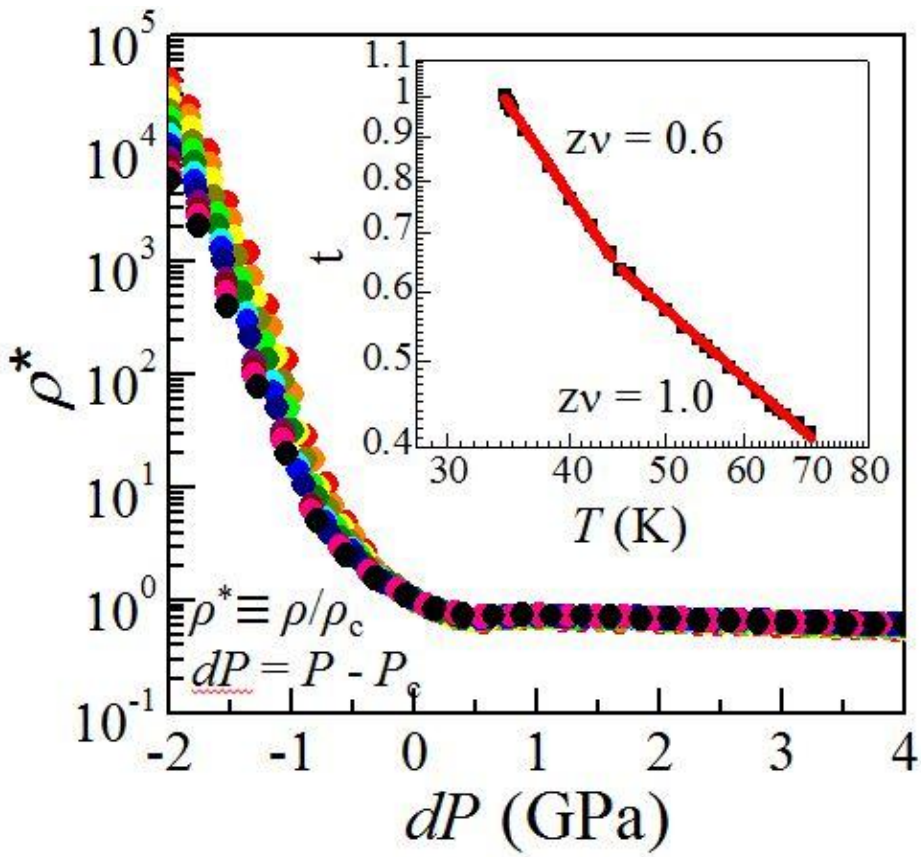

Figure 5.3.10. Normalized resistivity versus pressure. The t value as a function of temperature indicated in the inset. $z\nu$ can be calculated from t(T).

When we approach to the quantum critical point at zero temperature, the correlation length exponent ν and the dynamic exponent z diverge due to its second-order nature across the different phases. At finite temperature, another timescale must be considered $L_T \propto T^{-1}$ due to the thermal fluctuation. Consequently, one single parameter $\tau/L_T \propto T/|g - g_c|^{z\nu}$ governs the singular parts of physical quantities [8].

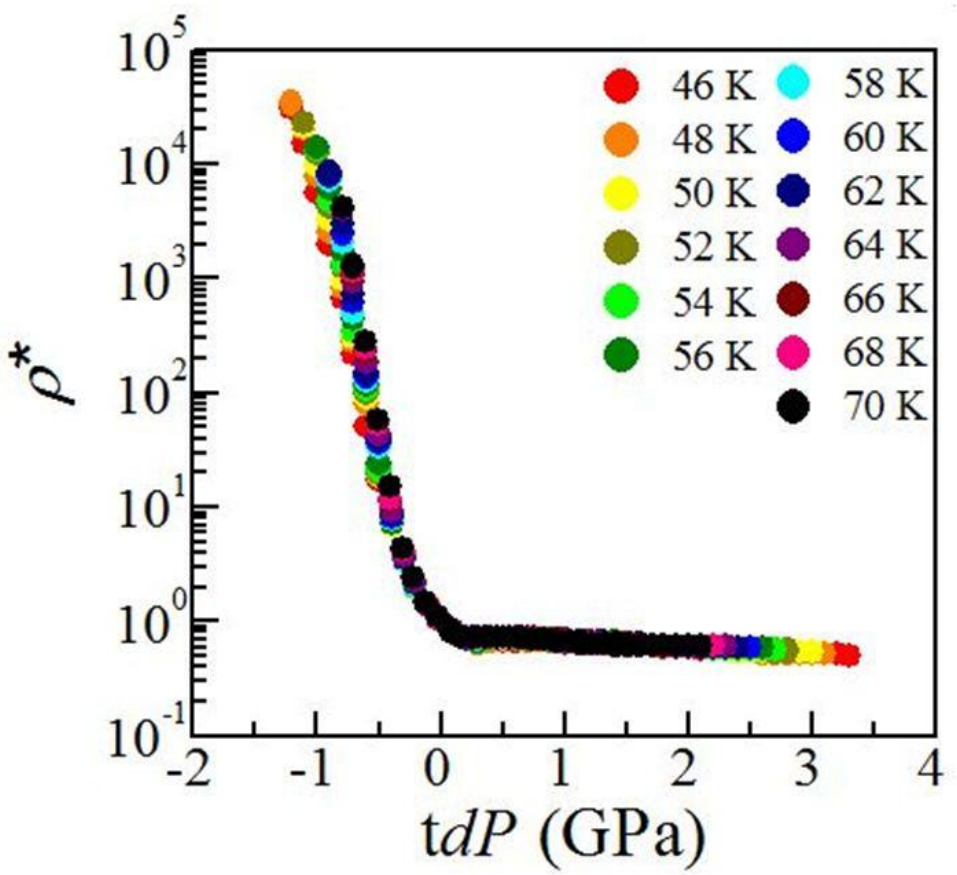

Figure 5.3.11. Scaling of resistivity at various temperatures.

In the present study, we adopt $\delta P = P - P_c(T)$ as a controlling parameter. We define normalized $\rho^*(P, T) \equiv \rho/\rho_c$ at selected temperature. To collapse resistivity data into one single curve, we plot $\rho^*(P, T)$ versus $t\delta P(T)$ as indicated in

figure 5.3.11. t(T) is a scaling parameter obtained from the least square fitting ranged from ΔP = -0.5 GPa to ΔP = 0.5 GPa for each T and zv value can be obtained from $t(T) = aT^{1/zv}$ as described in previous research [8]. In figure 5.3.10, two kind of zv factors were measured in the different T range. In the dynamical mean-field theory (DMFT) calculation, the scaling hypothesis is satisfied in the temperature range of $2T_c < T < 0.12t$, where T_c is the critical temperature and t is the nearest-neighbor transfer integral in the Hubbard model. Therefore, we adopt the temperature ranged from 46 K to 70 K to obtain the single zv value. In this study, $\rho^*(P_c, T)$ at selected temperatures collapsed onto the bifurcation scaling curves with zv = 1 indicated in figure 5.3.12 and it implies the existence of the quantum criticality in the quasi-1D organic conductor. The obtained zv value surprisingly corresponds to the theoretical and experimental value studied on the 1D system [15, 16].

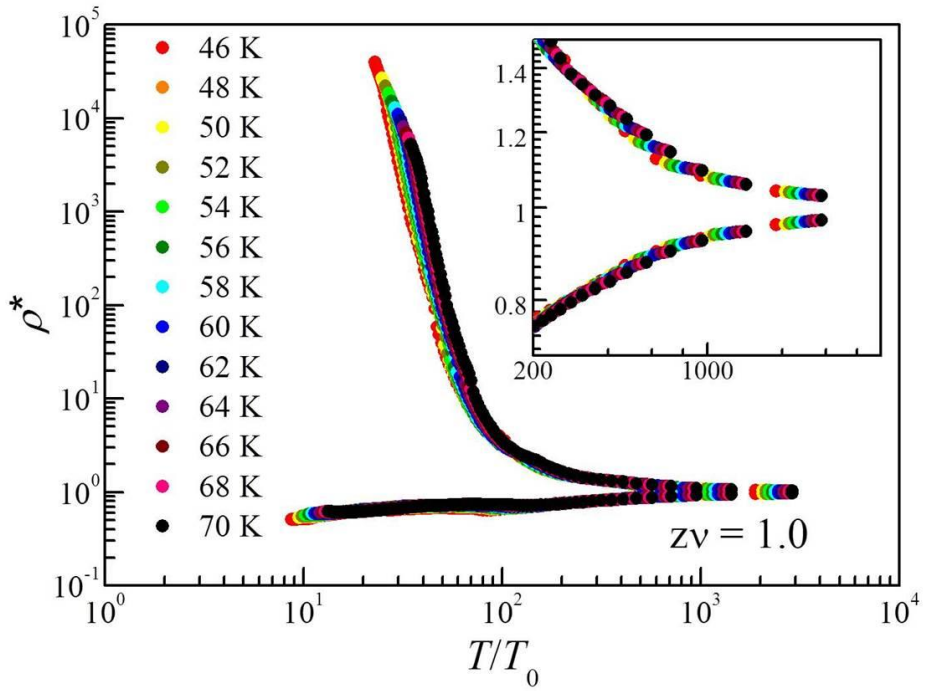

Figure 5.3.12.Bifurcation of the resistivities. Metallic branch (up) and insulating branch (down) are observed. Mirror symmetry between metallic and insulating branches was observed near crossover pressure.

On the other hand, $z\nu = 6.4$ was obtained when we follow the crossover line measured from the inflection point of $\log[\rho(P, T)]$ (not order parameter) vs P indicated in Figure 5.2.13(a) and (b). Furthermore, the bifurcation curve is insensitive to the critical exponent $z\nu$ lager than 6.4 indicated in figure 5.3.14. In two-dimensional materials of organic conductor and Si-MOSFET, difference of $z\nu$ value was shown [8, 10, 11]. The discrepancy of each circumstance may come from two possible scenarios; 1) different crossover lines were chosen, 2) different tuning parameters such as the carrier density or hydrostatic pressure were chosen. Further theoretical and experimental results are required to clarify the relation between this quantum criticality and $z\nu$ value.

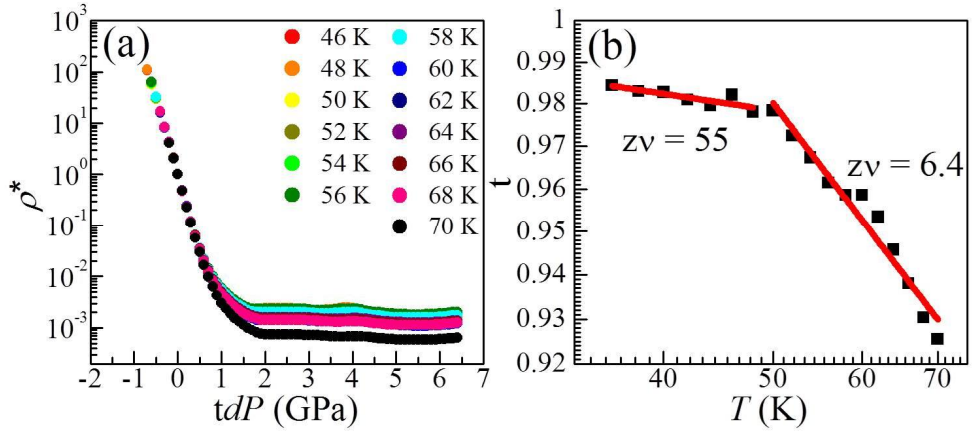

Figure 5.3.13. $z\nu = 6.4$ was obtained when we follow the crossover line measured from the inflection point of $\log[\rho(P, T)]$ vs P.

Although obtained critical exponents with different crossover lines are different, the critical exponent of the quasi-1D organic conductor shows the different value of the quasi-2D organic conductors [8]. It is important to note that our obtained critical exponent $z\nu = 1$ is the same value of the 1D Bose gas realized by optical lattices [15]. Previously reported result strengthens our result that the 1D system has universal $z\nu$ value of 1. Different critical exponent sets categorize the universality classes and it depends only on dimensionality or the symmetry.

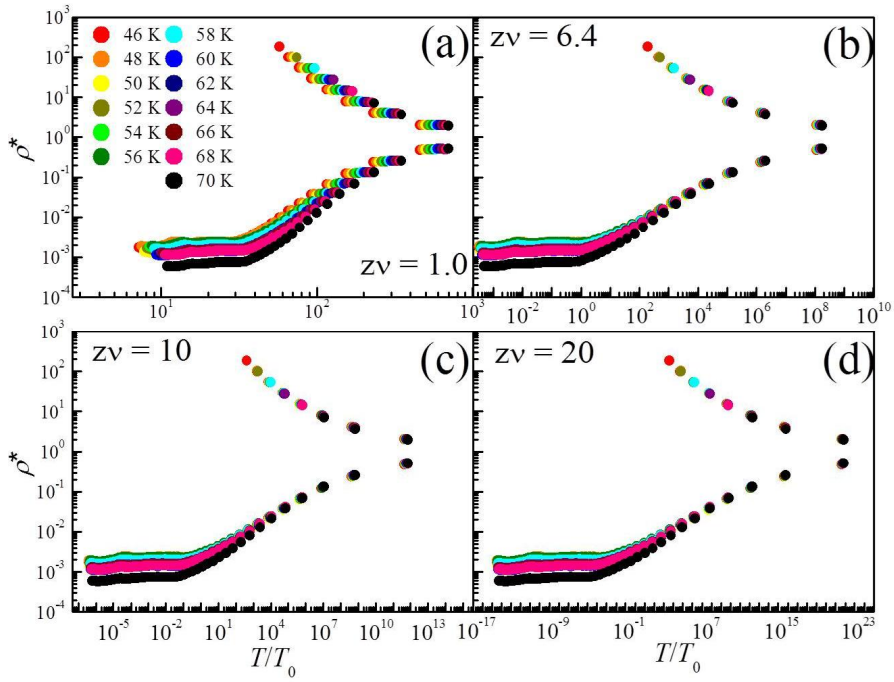

Figure 5.3.14. The bifurcation curves with different critical exponent of zν. Bifurcation is insensitive to zν value larger than 6.4.

Conclusion

We have measured critical exponents of δ, β, and γ. We introdeced new temperature T^* defined by the maximum point of $d\sigma/dP$ because no first-order transition was observed in this material. Obtained critical exponents are $\delta = 1$, $\beta = 1$ and $\gamma = 0$ near T^*, which are unconventional value compare to other universality classes. Critical exponents far away from T^* show $\delta = 2$, $\beta = 1$ and $\gamma = 1$. These values are the same as critical exponents of 2D organic conductor. This might be related to dimensionality crossover from 1D to 2D.

Moreover, Finite temperature quantum criticality in the quasi-1D organic conductor was investigated. The critical exponent $z\nu = 1$ was measured by the

crossover transition from metal to insulating state. This value is surprisingly corresponds to theoretical value of the 1D system with $z = 2$, $\nu = 1/2$ for quantum critical regime and $z = 1$, $\nu = 1$ for Luttinger liquid phase and it was confirmed by experiment in 1D Bose gas. Our finding of $z\nu$ value in the strongly correlated electron system with a quasi-1D material suggests that the critical exponents is universal regardless of their microscopic origin and governed by global factor such as a dimensionality or the symmetry.

5.4 $Nb_2Pd_xSe_5$

New superconductor $Nb_2Pd_xSe_5$ with T_C = 5.5 K has been discovered by Seunghyun Khim *et al* in 2013. It has quasi-1D Nb-Se chains along *b* directions and each conducting chain is hybridized to form the conducting *b* - *c** planes [22]. Neutron diffraction data revealed that $Nb_2Pd_xSe_5$ has the space group *C*12/m monoclinic structure with lattice parameters of *a* = 12.788 Å, *b* = 3.406 Å, *c* = 15.567 Å [22]. Previous reported research shows that this superconductor has bulk superconductivity and BCS-type pairing mechanism [22]. The upturn of the resistivity was observed near 50 K and it may come from Fermi surface character, charge density wave, or defects of crystals.

5.5 High-pressure effect of $Nb_2Pd_xSe_5$

This newly discovered superconductor $Nb_2Pd_xSe_5$ has the maximum T_C as high as 5.9 K and the resistivity anomaly was observed near 50 K [22]. Applying high pressure changes material properties, since superconductivity and density wave are sensitive to pressure. If we can fully suppress resistivity upturn and find superconducting dome, we can argue that the possibility of the quantum critical point or competing orders between superconductivity and unknown orders.

Experimental

Polycrystalline samples were grown by the conventional solid state reaction method. The mixture of Nb (99.999 %), Pd (99.99 %), and Se (99.99 %) were weighted in stoichiometric ratio and kept at 800 ºC for 2 – 3 days inside of sealed quartz ampules in vacuum. Single crystals of $Nb_2Pd_xSe_5$ were grown by

chemical vapor transport method with transport agent of $SeCl_4$ [22]. Typical sizes of single crystals are 50 μm × 50 μm × 500 μm with a needle shape. Gold wires are used as electrodes and attached to sample using silver paste (Dupont 4929N) and silver epoxy. The direction of applied current is *b*-axis which is a needle direction in the single crystal.

Results and discussion

Previous reported data shows the resistivity and the magnetization measurements as a function of temperature of polycrystalline $Nb_2Pd_{1.2}Se_5$ samples. Zero resistivity T_C was observed at 5.5 K. The magnetization of the zero field cool measurement indicates that the volume fraction of the polycrystalline same is almost 100 % [22].

High-pressure transport effects were measured using hybrid piston cylinder cell up to 2.2 GPa. Daphne 7373 oil was used as pressure transmitting medium to keep hydrostaticity of the sample space.

Near 50 K, the resistivity upturn defined as a T^* was observed and it continuously suppressed as pressure increases as indicated in figure 5.5.1. Whereas, T_C increases with pressure up to 2.2 GPa. We did not observe the maximum T_C due to the limitation of applying pressure.

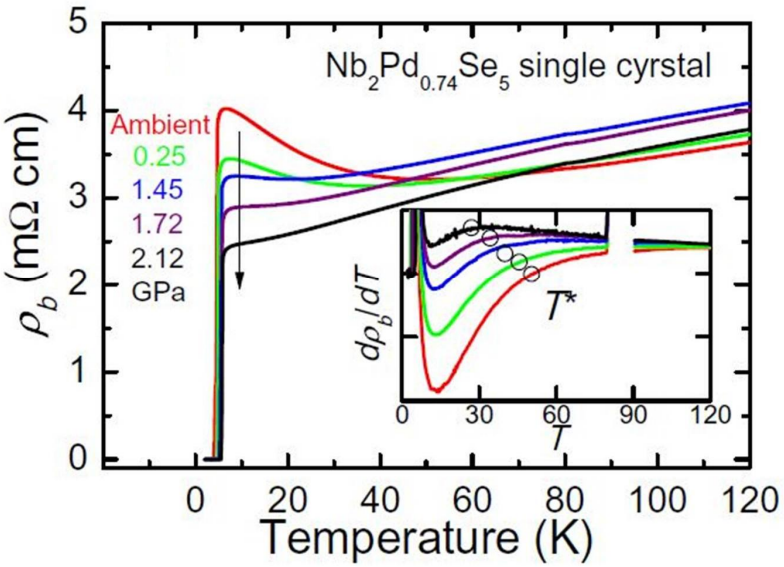

Figure 5.5.1. High pressure effect of $Nb_2Pd_{0.74}Se_5$ single crystal. T_C increases with pressure, while T^* was suppressed by pressure [22].

Overall phase diagram is depicted in figure 5.5.2. In low pressure regime, T_C increase linearly with rate of 1.8 K/GPa which is larger compared to other chalcogenide superconductors.

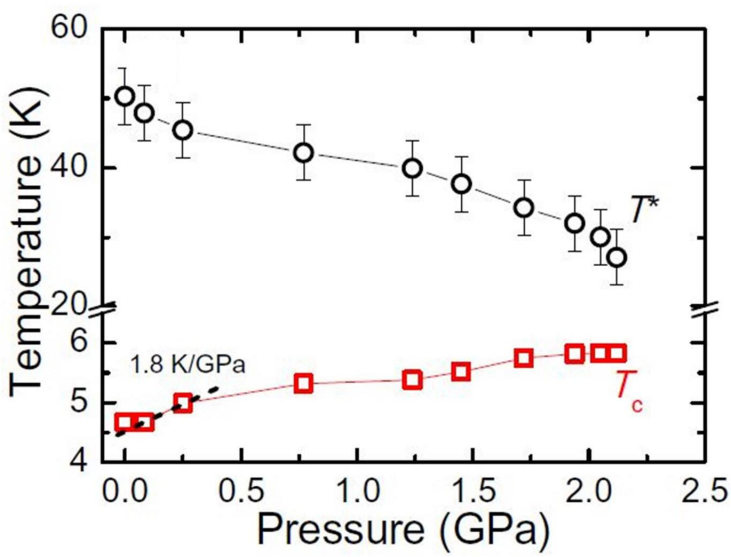

Figure 5.5.2. *p-T* phase diagram of $Nb_2Pd_{0.74}Se_5$ single crystal. T_C increase continuously with initial slope of 1.8 K/GPa [22].

Conclusion

New quasi-1D superconductor $Nb_2Pd_xSe_5$ with T_C = 5.5 K was grown by the chemical vapor transport growth technique. Low dimensional materials usually show density wave character such as charge density wave or spin density wave due to its Fermi surface character. In $Nb_2Pd_xSe_5$ superconductor, the resistivity upturn, which may be related to spin density wave appears near T^* = 50 K. High-pressure suppresses T^*, while the superconductivity is enhanced. Thus, T^* might be competing with the superconductivity. Higher pressure is required to find the maximum T_C and fully suppression of T^*.

Bibliography

[1] Georges, A *et al*. AIP conf. Proc. **715** 3-74 (2004)

[2] Kotiliar *et al*. Phys. Rev. Lett. **84** 5180 (2000)

[3] Kotilar *et al*. Phys. Today **57** 53 (2004)

[4] Onoda *et al*. arXiv:cond-mat/0408207v1 (2004)

[5] P. Limelette *et al*. Science **302** 3 (2003)

[6] F. Kagawa *et al*. Nature **436** 534 (2005)

[7] Terletska *et al*. Phys. Rev. Lett. **107** 026401 (2011)

[8] T.Furukawa *et al*. Nat. phys. **11** 221 (2015)

[9] Misawa *et al*. Phys. Rev. B. **75** 115121 (2007)

[10] Kravchenko *et al*. Phys. Rev. B. **51** 7038 (1995)

[11] Dragana Popovic. Phys. Rev. Lett. **79** 1543 (1997)

[12] D.B. McWhan. Phys. Rev. B. **2** 3734 (1970)

[13] A. Jayaraman. Phys. Rev. B. **2** 3751 (1970)

[14] Misawa, T. & Imada. Phys. Rev. B **75,** 115121 (2007)

[15] Bing Yang *et al*. arXiv:1611.00426v1 (2016).

[16] Giamarch, T. Quantum physics in one dimension (Oxford university press, 2004)

[17] Zhang,X. Science **335** 1070 (2012)

[18] Kaden R. A. Hazzard *et al*. Phys. Rev. A. **84** 013604 (2011)

[19] J.Vuucicevic *et al*. Phys. Rev. B. **88** 075143 (2013)

[20] F.F Tafti *et al*. Phys. Rev. B. **85** 205104 (2012)

[21] N.Hanasaki *et al*. Phys. Rev. Lett. **96** 116403 (2006)

[22] Seunghyun Khim *et al*. New journal of physics **15,** 123031 (2013)

[23] Komatsu *et al*. J. Phys. Soc. Jpn. **65,** 1340 (1996).

[24] Nishikawa *et al*. unpublished

Appendix

A1. Helium liquefier system

Helium is valuable materials in the scientific point of view. It has been using as an inert gas or pressure transmitting medium. However, the most important purpose of the helium in the scientific field is a coolant of the sample space. We can reach temperature down to 4.2 K by soaking the sample into liquid helium since the boiling point of liquid helium is 4.2 K. When pressure is decreased by pumping the sample space, the boiling point of liquid helium is decreased down to 1.23 K at 100 Pa. To make lower temperature, helium isotope ^{3}He is used to reach temperature down to 0.3 K. A mixture of ^{4}He/^{3}He cools the samples down to 2 mK using the dilution refrigerator.

Although liquid helium is very important coolant in the science field, low-temperature experiments are limited due to low supply and high price of liquid helium. The biggest problem is light atomic mass of helium gas because gravity of Earth cannot keep helium gas inside of atmosphere. Thus, helium gas keeps decrease continuously. To solve this problem, many research groups have installed helium liquefier with closed circuit system to prevent helium gas from evaporation to outer space. The advantage of helium liquefier is stable supply and decrease of price.

We used many cryostats such as a Physical property measurement system (PPMS^{TM}), Magnetic property measurement system (MPMS^{TM}), Pulsed magnet, 14 T Janis magnet, and cubic anvil cell. Thus, stable helium supply is very important to keep continuous operation.

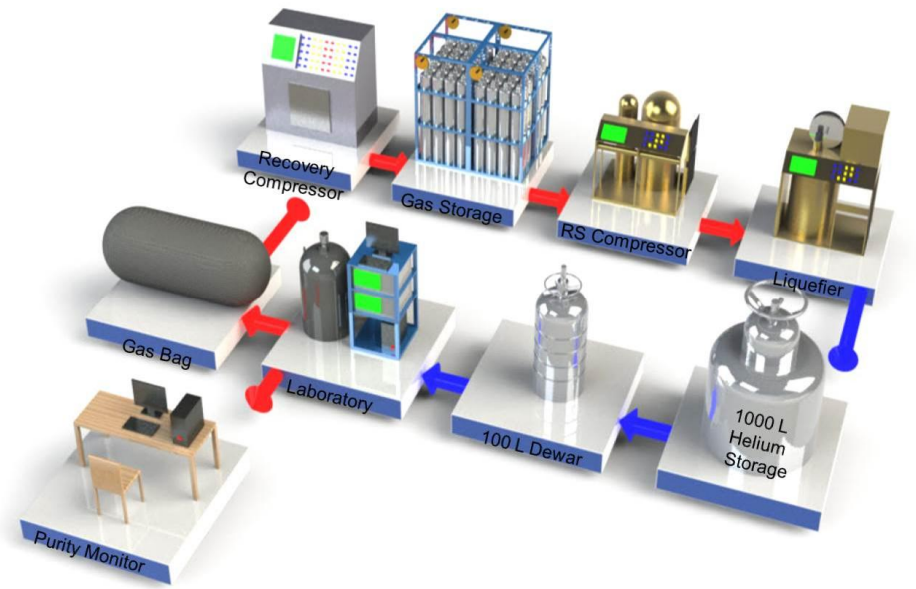

Figure A1.1. Schematics of helium liquefying system. Closed circuit of helium is crucial part to sustainable operation.

In figure A1.1, overall helium liquefier system was indicated. After using liquid helium in each laboratory, impure gas helium is gathered in the gas bag. This gathered impure helium gas is compressed by recovery compressor and send it to gas bombe with 1800 psi. This compressed helium gas is cooled by isentropic expansion and Joule-Thomson expansion using RS compressor and helium liquefier. Cold and high pressure helium gas is liquefied inside of 1000 L helium storage by decreasing the pressure of gas helium. This closed liquid/gas helium circulation system results in small loss of gas helium, if we can keep helium gas with very high purity. To keep the high purity of helium gas, we are monitoring helium purity of each laboratory using helium purity monitors which is connected to internet and gather information of each laboratory's helium purity in the single computer indicated in figure A1.2.

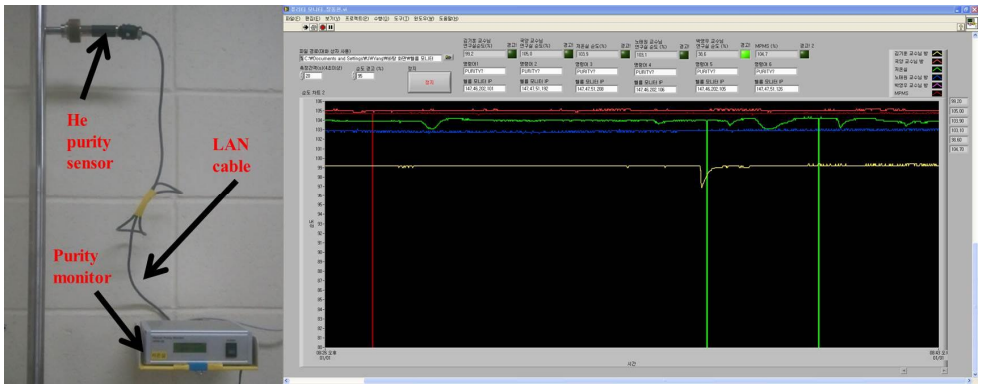

Figure A1.2. Helium purity monitor connected to internet. The purity of helium gas of each laboratory is collected by LabVIEW software.

Helium liquefier and 1000 L liquid helium storage are indicated in figure A1.3 (left) and RS compressor is indicated in figure A1.3 (right).

Figure A1.3. Helium liquefier and the 1000 L liquid helium storage (left). RS compressor can pressurize 5 psi helium gas to 240 psi of pressure.

When we liquefy helium gas, many conditions can change liquefaction rate. The performance of liquefier is determined by liquefaction rate of liquid helium. The important conditions are listed below.

1) Gas helium inlet pressure: Inlet gas pressure controlled by RS compressor

determines the liquefaction rate, since pressure difference between inlet and outlet pressure determines cooling power in the liquefier.

2) Flow of the gas: Although inlet gas pressure is enough, low flow rate can decrease liquefying rate. If helium flow is lowered, pressure difference between inlet and outlet becomes bigger.

3) Temperature of pre-cooled helium gas: In the helium liquefier, gas helium goes through long line with continuous cooling. At each stage, specific temperature is very important because these temperatures are harmonized for fast and continuous liquefaction. Thus, adequate temperature at each stage should be monitored and be kept those values constant.

The helium purifier is installed inside of our liquefying system and it can liquefy impure helium gas (< 80 % purity) to pure helium gas. Moreover, we have one big size of helium purifier which can purify impure helium gas with high purity up to 99.999 %. This big helium purifier enables us to provide pure helium gas (figure A1.4).

Figure A1.4. Helium purifier. Impure helium gas can be purified up to 99.999 % of purity.

A2. Floating zone method

Figure A2.1. Picture of the floating zone system. It has two halogen lamps and quartz tube.

Growth of the single crystals is important in research area, since directional measurement is possible using single crystals. Traditionally, single crystals have been grown by the flux method. However, flux or materials is possible to react with the crucible and damage the crucible. In addition, flux material can be doped into the single crystals. To overcome this limitation, single crystal growth method called floating zone method without crucible was invented (figure A2.1).

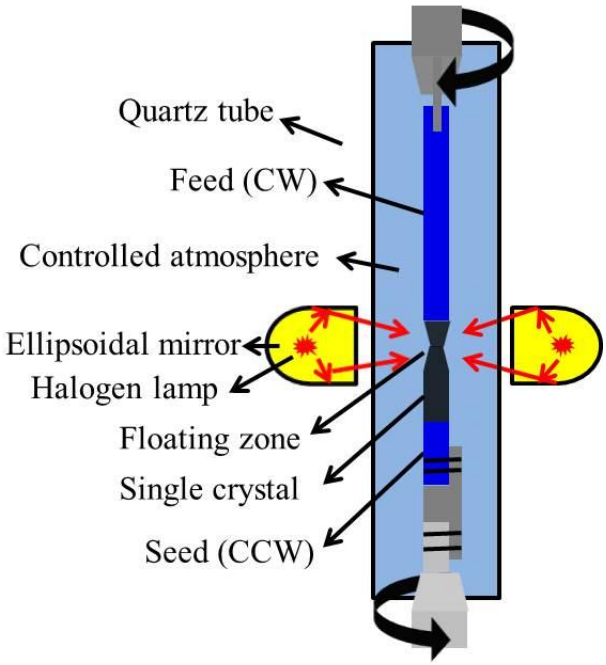

Figure A2.2. Schematic of floating zone method. Two halogen lamps melt poly-crystalline rods and grow single crystal.

The word of “floating zone” is related to melting zone which moves to upward aligning atomic position and form single crystal. In figure A2.2, two ellipsoidal mirrors reflect and focus light at a single point. This focused light heat a center of the poly-crystalline rod and eventually melts the poly-crystalline sample. Only focused region is melted and other parts remains solid poly crystal. This focused light can cause high temperature gradient and result in high thermal stress. This molten zone goes upward with adequate moving rate and makes single crystals.

Poly-crystalline seed and rod should be prepared before starting floating zone method. Poly-crystalline sample which is usually grown by the conventional solid state reaction was crushed into fine power form. Ground powder is pushed into long balloon to make cylindrical seed and rod. After filling the poly-crystalline

powder into balloon, pumping out process is necessary to remove air bubble inside of this balloon. We used 1 inch diameter cylinder to pressurize balloon up to 300 MPa. In this process, waiting time is important factor. If waiting time is too short, rod is easily broken or causes the density inhomogeneity. The density inhomogeneity is crucial part for growing single crystal in the traveling solvent floating zone method, which will be explained later. We usually wait longer than 1 hour to remove such a problem. After that, we cut balloon and obtain poly-crystalline seed and rod with 7 cm length and 6 ~ 7 mm size of diameter. Grown seed and rod are mounted in the floating zone machine with perfect orientation. After aligning seed and rod with a perfect orientation, we rotate seed and feed rod with opposite direction to mix the liquid homogeneous. Rotation rate is not sensitive to make single crystal but sensitive to the quality of the crystal, which can be characterized by Rocking curve in XRD pattern. The most important growth condition is growth rate. Our floating zone machine has 0.1 – 20 mm/h of growth rate. Usually, slow growth rate is applicable to layered material or incongruent melting case. However, faster growth rate can be applicable to single crystal which has high evaporation rate in liquid form. Grown crystals are characterized using powder XRD or LAUE.

Congruent and incongruent melting

Single crystal growth needs melting process, since reorientation of atoms must happen. When we melt crystals, we should consider whether molten crystals are congruent melting or incongruent melting. Congruent melting crystals are relatively easier to grow single crystals compare to incongruent melting case. Congruent melting is that the target compound AB is energetically more stable than

A or *B* compound. Thus, the melted mixture *A* + *B* solidifies and forms *AB* compound. In incongruent melting case, however, *A* + *B* goes to *A* + *B*, *A* + *C*, or *AB* + *C*, which never makes *AB* compound. Thus, congruent melting case is easier to grow single crystal than incongruent melting case. In congruent melting case, conventional floating zone method is possible to grow single crystals. However, in incongruent melting sample, conventional floating zone method is impossible due to separation of crystal phases. In above case, traveling solvent floating zone method is applicable to grow single crystals which have incongruent melting character. The traveling solvent floating zone method is different crystal growth method compare to conventional floating zone method. In conventional floating zone method, liquid poly-crystalline sample turns into single crystal during solidification process to reduce internal energy. In the traveling solvent floating zone method, liquid flux which is liquid poly-crystal or other liquid compound aligns atoms and form single crystal.

$LaInO_3$ single crystals

We have grown many single crystals using floating zone method and some of them were published. Here, we introduce the single crystal growth of $LaInO_3$.

Growth of $LaInO_3$ single crystal is important, since it can be used as substrate which covers 4.1 Å lattice constant indicated in figure A2.3 (a). Color of grown single crystal has brown (figure A2.3 (b)) and it becomes transparent in the visible light region when thickness of the crystal is getting thinner, stated in figure A2.3 (c).

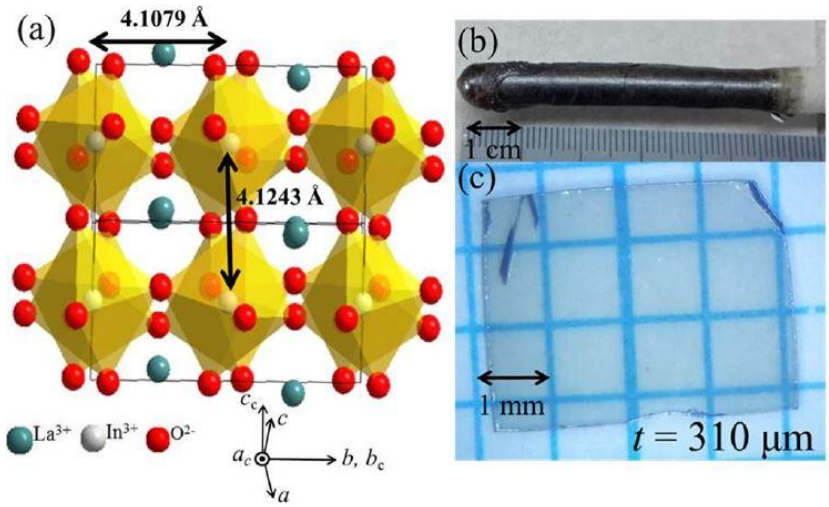

Figure A2.3. (a) Crystal structure of $LaInO_3$. (b) Grown single crystal using floating zone method. Color of the grown crystal is brown. (c) After polishing, $LaInO_3$ single crystal is transparent in the visible light region [1].

The absorption coefficient of grown crystals depends on the growth conditions. We tried to three different conditions. During the crystal growth, we applied 1.0 MPa of oxygen gas pressure to prevent evaporation of In_2O_3 powder. Thus, we only can change the growth rate as a dominant growth condition as indicated in figure A2.4. The growth rate affects to the absorption coefficient. Slower growth rate increases evaporation of In_2O_3 powder and color of the single crystal is darker. While faster than 15 mm/h growth rate, grown crystal shows more transparent in the visible light region. Three samples are grown under 10 bar of O_2 gas pressures. As a result, we used 15 mm/h growth rate as an optimal condition, since slower growth rate forms bigger single crystal and higher crystallinity.

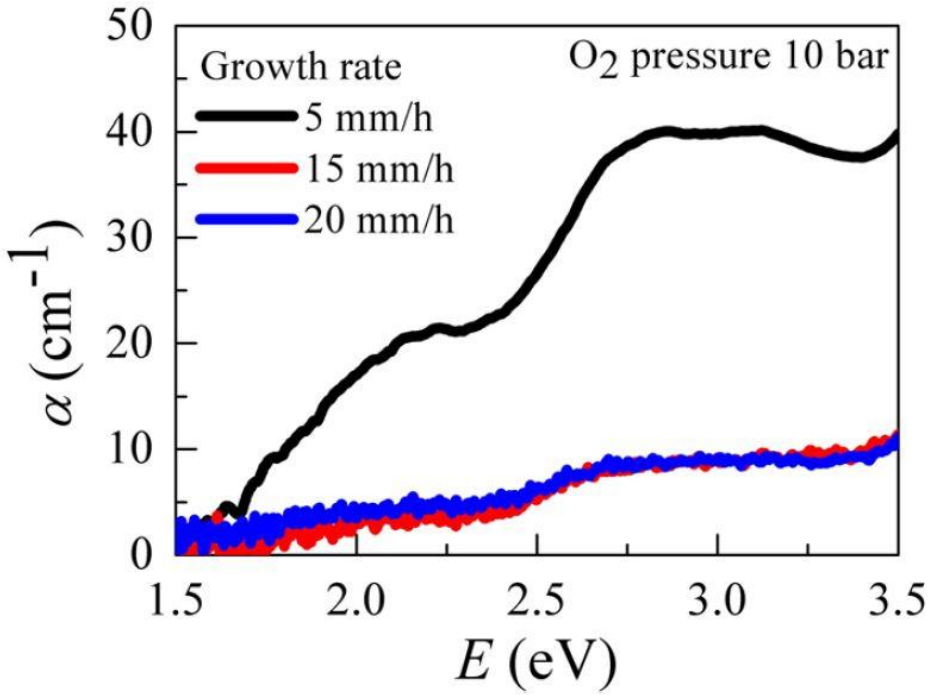

Figure A2.4. Absorption coefficients of various single crystals grown in different growth rate [1]. 15 mm/h of growth rate was chosen as an optimal growth rate.

To confirm single phase and crystallinity of grown crystal, we measured x-ray diffraction of $LaInO_3$ single crystal. Grown crystals are single phase and single crystal. Rocking curve of 0.0345º shows that the grown crystal has good crystallinity.

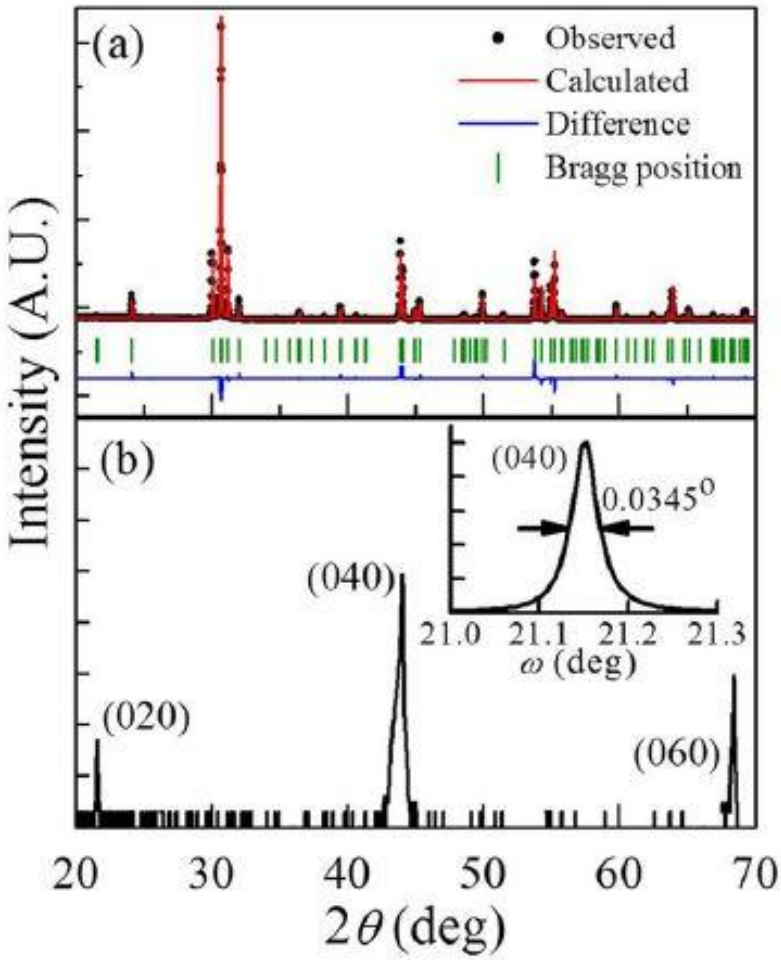

Figure A2.5. (a) Powder XRD data. (b) Rocking curve of $LaInO_3$ single crystal [1]. X-ray powder diffraction and single crystal diffraction show that growth crystal is good quality.

We measured electrical properties of $LaInO_3$ single crystal to measure activation energy and dielectric constant. The calculated activation energy of 0.7 eV indicated that electrical band gap is 1.4 eV, although $LaInO_3$ single crystals are transparent in the visible light region. The dielectric constant measurement shows that the kinks are observed near 25 K and 35 K, which may be related to structure transition.

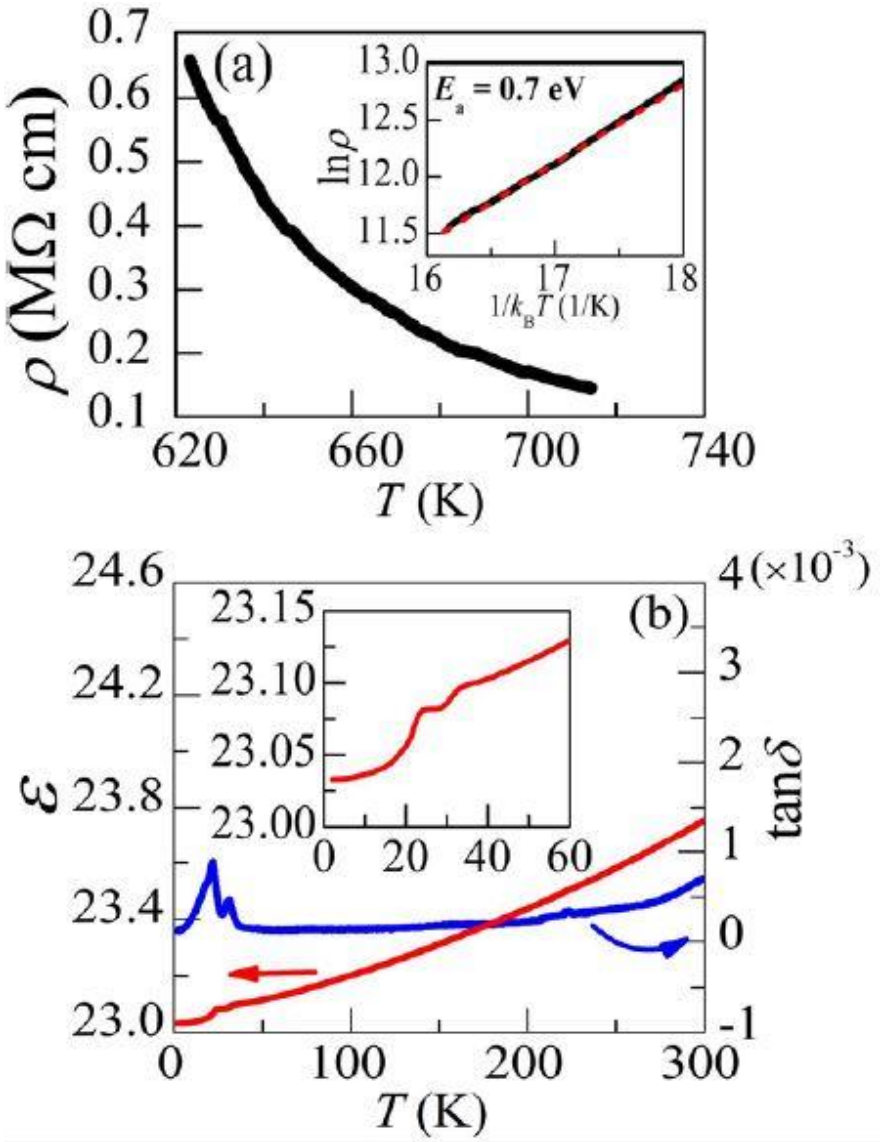

Figure A2.6. Electrical properties of $LaInO_3$ single crystals. (a) Electrical transport measurement shows that the activation energy of $LaInO_3$ single crystal is 1.4 eV. (b) Dielectric constant and tangent loss show the anomalies at 25 K and 35 K [1].

In figure A2.7, the transmittance and the absorption coefficient shows that three kinds of transition were observed. Energy scale of transition A is the similar

to intrinsic energy band gap of 1.4 eV obtained by the electrical transport measurements. The absorption coefficient diverges when the photon energy is higher than 4.13 eV, which corresponds to optical band gap. The optical band gap higher than 3.3 eV indicates that this single crystal is transparent in the visible light region.

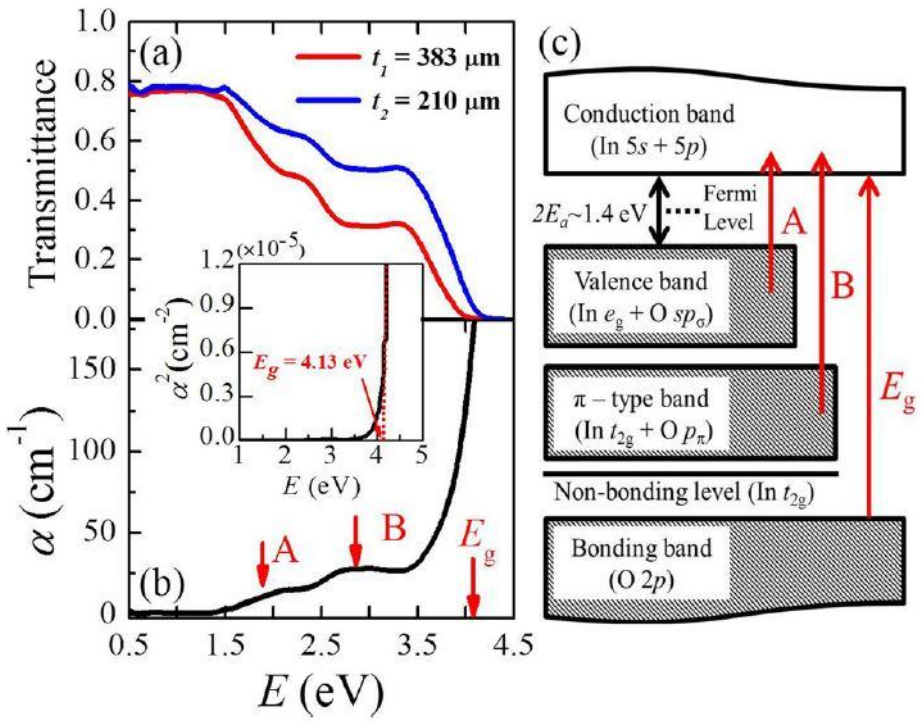

Figure A2.7. Optical properties of $LaInO_3$ single crystals. (a) Three kinds of transmittance steps are observed. (b) The absorption coefficient of $LaInO_3$ single crystal shows three kinds of transition at 1.4 eV, 2.7 eV, and 4.1 eV, which are indicated as A, B, E_g, respectively.

We have grown $LaInO_3$ single crystals for the first time. Lattice constant of 4.1 Å is applicable as a substrate to make film of $BaSnO_3$, which has high electrical mobility in room temperature.

A3. List of grown single crystals using floating zone method

1. $(Co_{1-x}Zn_x)Nb_2O_6$ (x = 0.00, 0.04, 0.05, 0.06, 0.07)

O_2 gas flow40 rpm, 1 mm/h

2. $LaInO_3$

10 bar O_2 gas pressure, 15 rpm, 15 mm/h

3. $La_{0.9}Ca_{0.1}InO_3$

10 bar O_2 gas pressure, 30 rpm, 15 mm/h

4. $PrInO_3$

10 bar O_2 gas pressure, 15 rpm, 5 mm/h

5. $La_{1-x}Pr_xInO_3$ (x = 0.2, 0.4, 0.8)

10 bar O_2 gas pressure, 20 rpm, 15 mm/h

6. $Pr_{0.97}Sr_{0.03}InO_3$

10 bar O_2 gas pressure, 15 rpm, 5 mm/h

7. Mn_3O_4

O_2 and Ar flow, 15/25 rpm, 5/20 mm/h

8. $Mn_{2.9}Cu_{0.1}O_4$

O_2 and Ar flow, 25 rpm, 5 mm/h

9. $BiCu_2PO_6$

6.5 bar O_2 gas pressure, 20 rpm, 1 mm/h

10. $MnGa_2O_4$

Ar flow, 20 rpm, 5 mm/h

11. $BaBiO_3$

10 bar O_2 gas pressure, 20 rpm, 10 mm/h

12. $CaBaCo_4O_7$

6 bar O_2 gas pressure, 40 rpm, 20 mm/h

Bibliography

[1] Dong Hyun Jang *et al*. Journal of Applied Physics **121**, 125109 (2017)

List of publications

1. Seunghyun Khim, Bumsung Lee, Ki-Young Choi, Byung-Gu Jeon, **Dong Hyun Jang**, Rokyeon Kim, Eun Sang Choi, Seongsu Lee, Jaejun Yu and Kee Hoon Kim. "Enhanced Upper Critical Fields in a New Quasi-one-dimensional Superconductor $Nb_2Pd_xSe_5$", New Journal of Physics **15** 123031 (2013)
2. L. H. Yin, **D. H. Jang**, C. B. Park, K. W. Shin, and Kee Hoon Kim. "Pressure-induced ferroelectricity and enhancement of Mn-Mn exchange striction in $GdMn_2O_5$". Journal of Applied Physics **119** 104101 (2016)
3. Rana Saha, Somnath Ghara, Emmanuelle Suard, **Dong Hyun Jang**, Kee Hoon Kim, N. V. Ter-Oganessian, and A. Sundaresan. "Magnetoelectric effect in simple collinear antiferromagnetic spinels". Physical Review B **94** 014428 (2016)
4. **Dong Hyun Jang**, Woong-Jhae Lee, Egon Sohn, Hyung Joon Kim, Dongmin Seo, Ju-Young Park, E. J. Choi, and Kee Hoon Kim. "Single crystal growth and optical properties of a transparent perovskite oxide $LaInO_3$". Journal of Applied Physics **121** 125109 (2017)
5. Woong-Jhae Lee, Hyung Joon Kim, Jeonghun Kang, **Dong Hyun Jang**, Tai Hoon Kim, Jeong Hyuk Lee, and Kee Hoon Kim. "Transparent perovskite barium stannate with high electron mobility and thermal stability". Annual Review of Materials Research **47** 391 (2017)
6. **Dong Hyun Jang**, Dilip Bhoi, Yeahan Sur, Chanhee Kim, Keizo Murata and Kee Hoon Kim. "Pressure and chemical tuning of charge density

wave and superconductivity in 2*H*-Pd_xTaSe_2". submitted to Physica C

7. **Dong Hyun Jang**, Yeahan Sur, Sho Miyamoto, Hiroyuki Nishikawa, Keizo Murata1 and Kee Hoon Kim. "Quantum criticality in a quasi-one-dimensional organic conductor". in preparation
8. Dilip Kumar Bhoi, Byeong Hyun Min, **Dong Hyun Jang**, Shim Jee Hoon, Duck Young Kim, Keizo Murata and Kee Hoon Kim. "Pressure enhanced superconductivity and quantum criticality in $Ca_{1-x}La_xFeAs_2$ iron based superconductors". in preparation

국문초록

물질에 고압을 인가 함으로써 물질의 특성을 변화시켜 초전도, 양자임계현상, 부도체-도체 전이 등 많은 흥미로운 현상들이 발견되고 있다. 특히, 최근 200 K이 넘는 고온 초전도체가 고압 하에서 발견됨으로써, 고압 하에서 상온 초전도체의 발견을 기대하고 있다.

위와 같은 물질의 고압 효과를 측정하기 위해서, 많은 압력 장비들이 사용 되고 있다. 대표적인 고압 인가 장비로는 Hybrid piston cylinder cell, Diamond anvil cell, Bridgman cell, Cubic anvil cell 등이 있다.

본 연구에서는 위에 언급한 고압 장비들에 대한 자세한 설명과, 저 차원구조를 가진 초전도체와 유기전도체에 압력을 인가함으로써 물질의 초전도 온도 및 밀도파 온도의 변화에 대해 연구 하였다.

준 2차원 구조를 가진 Pd_xTaSe_2, $CaFeAs_2$, 그리고 $BaFe_2As_2$ 물질 및 준 1차원 구조를 가진 $Nb_2Pd_xSe_5$ 초전도체의 전기 전도도를 압력하에서 측정을 하였다. 측정한 세 종류의 초전도 단결정에서는 압력하에서 초전도 온도가 증가하고, 밀도파 특징이 줄어드는 효과를 발견할 수 있었다. 이는 압력 하에서 밴드구조가 변하는 것을 의미하며, 이론적인 계산결과의 필요성을 제안하고 있다.

준 1차원 구조를 가진 $[(S,S)\text{-DM-MeDH-TTP}]_2AsF_6$ 유기전도체의 압력 효과 측정에서는 부도체-도체 전이에서 1차 상전이를 발견하지 못하였지만, 새로 T^* 를 정의하여 그 근처에서

임계지수 δ, β, γ 를 구하였다. 또한, 이 물질에서 양자임계현상을 발견하였고, 임계지수 $z\nu = 1$ 이라는 것을 발견하였다. 이는 물질의 보편성 부류가 차원이나 대칭성등 온곳 인자에 의해서만 결정되고, 미세적 세부 구조에 대해서는 결정되지 않는 다는 것을 의미한다.